

新制

理

1158

學位申請論文

王 功輝

**AN EXPERIMENTAL STUDY ON THE MECHANISM OF
FLUIDIZED LANDSLIDE**

**—WITH PARTICULAR REFERENCE TO THE EFFECT OF GRAIN SIZE AND
FINE-PARTICLE CONTENT ON THE FLUIDIZATION BEHAVIOR OF SANDS**

By

Gonghui WANG

A thesis submitted to the Graduate School of Science
Kyoto University
in partial fulfillment of the requirements
for the Doctor Degree of Science
in the Division of Earth and Planetary Science

December 1999

ABSTRACT

Fluidized landslides moving with high velocities and long run-out distances are often catastrophic, and prediction of the initiation and motion of fluidized landslides is an extremely important topic. Nevertheless, the mechanism of fluidized landslides has been poorly understood. Therefore, in this research, fundamental tests were performed on sands to study the fluidization and its maintaining mechanism by using a ring-shear apparatus, model flume and double cylinder rotating apparatus. Sands with different grain size and fine-particle content were used in these tests to investigate the effects of grain size and fine-particle content. As a case study, a fluidized landslide triggered by the August 1998 heavy rainfall, Fukushima Prefecture, Japan, was investigated and compared to the results of these laboratory experiments.

From the undrained ring-shear test results, it was observed that the brittleness index (the ratio of the difference between the peak shear and steady state strengths to the peak shear strength), which is an important factor affecting the acceleration of fluidized landslides, depended greatly on the initial stress state. Also, both peak and steady state shear strengths decreased when sands became finer in grain size or greater in fine-content.

According to flume tests on sands with the same thickness but different initial densities, it was found that there was an optimal density for high pore pressure generation for a given sand, at which both the corresponding run-out distance and peak velocity were the greatest. Examining the motion in flume tests and pore pressure maintaining tests with the double cylinder apparatus revealed that fine-particles played an important role for maintaining excess pore pressure during motion, i.e., fine-particles floated more easily during motion and increased the excess pore pressure.

According to the observations of a pit dug in the deposition area of the Fukushima fluidized landslide, a shear zone of approximately 20 cm wide was formed on the

bottom of this landslide and fine-particles existed in this shear zone. From the results of ring-shear tests on the volcanic deposits sampled from the source area of this landslide, it was inferred that grain crushing in the shear zone caused the generation of high excess pore pressure, which initiated the fluidization; meanwhile, the high content of fine particles in the original soil and the newly formed fines by crushing reduced the permeability further and made the dissipation of excess pore pressure from the shear zone more difficult. The combination of these factors resulted in the fluidized landslide with high-speed and long run-out distance.

These studies from ring-shear tests, model flume tests and field investigations have disclosed the mechanisms of fluidization of soil mass and its maintenance during motion, especially the important roles of fine-particle in the initiation and motion of fluidized landslides have been clarified.

TABLE OF CONTENTS

Chapter	Page
ABSTRACT	
1. INTRODUCTION	1
1.1 Background of This Study	2
1.2 Purpose of This Research	5
1.3 Outline of This Thesis	6
2. CONCEPTS AND KEY WORDS FOR FLUIDIZED LANDSLIDES	9
2.1 Liquefaction	9
2.1.1 Liquefaction History	9
2.1.2 Definition of Liquefaction	12
2.1.2.1 Mass liquefaction	12
2.1.2.2 Sliding surface liquefaction	14
2.2 Steady State Line and Collapse Surface	15
2.2.1 Steady State Line	15
2.2.2 Collapse Surface	17
2.3 Static Liquefaction Resistance and Brittleness Index	17
2.3.1 Static Liquefaction Resistance	18
2.3.2 Brittleness Index	18
2.4 Fluidized Landslide	19
2.4.1 Definition of Fluidized Landslide	21
2.4.2 Motion of Fluidized Landslide	21
2.4.2.1 Flowslides	21
2.4.2.2 Rapid slide motion	22
2.5 Apparent Friction Angle for Landslide	22

2.6 Other Concepts Used in This Thesis	24
3. SAMPLE, APPARATUS AND TEST PROCEDURE	27
3.1 Samples Employed in the Tests	27
3.2 Ring Shear Apparatus and Test Procedures	28
3.2.1 Ring Shear Apparatus	28
3.2.2 Test Procedures	31
3.3 Flume Test Apparatus and Test Procedures	34
3.3.1 Flume Test Apparatus	34
3.3.2 Test Procedures	35
3.4 Double Cylinder Apparatus and Test Procedures	36
3.4.1 Double Cylinder Apparatus	36
3.4.2 Test Procedures	37
4. THE FLUIDIZATION BEHAVIOUR OF THE SHEAR ZONE BASED ON RING SHEAR TESTS	38
4.1 Introduction	38
4.2 Experimental Results	40
4.2.1 Effects of Initial Relative Density on The Undrained Shear Behaviors	41
4.2.1.1 Ring shear test on loose sand	41
4.2.1.2 Ring shear tests on medium to dense sand	42
4.2.2 Effects of Initial Stress State	44
4.2.2.1 Effects of Initial Normal Stress	45
4.2.2.2 Effects of Initial Shear Stress	45
4.2.3 Effects of Grain Size	47
4.2.3.1 In loose state	47
4.2.3.2 In dense state	48
4.2.4 Effects of Fine-Particle (Loess) Content	50

4.2.4.1 In loose state	50
4.2.4.2 In dense state	51
4.3 Mechanism of Fluidization in the Shear Zone	52
4.3.1 Formation of Localized Fluidization in the Shear Zone	52
4.3.2 Grain Crushing Within the Fluidized Shear Zone	54
4.3.3 Collapse Behaviour of Loose Sand Within the Shear Zone	56
4.3.4 Brittleness Index for Sand at Different Stress States.....	58
4.3.5 Characterization of Fluidization Behavior of Sand with Different Grain Size and Fine-Particle (loess) Contents	59
4.3.5.1 Pore pressure generation at different stages	60
4.3.5.2 Undrained peak shear strength	61
4.3.5.3 Steady state strength	62
4.3.6 Maintaining of Generated Pore Pressure in Shear Zone	63
4.4 Summary	65
5. THE FLUIDIZATION BEHAVIOUR OF LANDSLIDE MASS IN THE FLUME TESTS	66
5.1 Introduction	66
5.2 Test Conditions	68
5.3 Observed Phenomena and Discussion	68
5.3.1 Excess Pore Pressure Generation	68
5.3.2 Motion of Failed Landslide Mass	69
5.3.2.1 Retrogressive sliding	70
5.3.2.2 Flowslides	71
5.4 Effects of Initial Void Ratio	73
5.4.1 On Excess Pore Pressure	73
5.4.2 On the Motion of Landslide Mass	74
5.4.2.1 On the failure mode of retrogressive sliding	74
5.4.2.2 On the flowslide motion	74

5.5 Effects of grain size and fine-particle (loess) contents	75
5.5.1 Differences in Excess Pore Pressure Generation	76
5.5.2 Differences in Resulting Motion of Landslide Mass	76
5.6 Pore Pressure Maintaining Mechanism During Motion Through Double Cylinder Mixing Test	77
5.6.1 Test Phenomena	78
5.6.2 Effects of Sample	80
5.7 Initiation Process and Motion of Fluidized Landslides	82
5.7.1 Initiation Process of Fluidized Landslides	82
5.7.2 Motion of Fluidized Landslides	84
5.8 Comparison of Ring Shear Test and Flume Test	85
5.9 Summary	86
6. CASE STUDY ON THE MECHANISM OF A FLUIDIZED LANDSLIDE TRIGGERED BY THE AUGUST 1998 HEAVY RAINFALL, FUKUSHIMA PREFECTURE, JAPAN	88
6.1 Introduction	88
6.2 Landslide Property	89
6.3 Ring Shear Tests	92
6.3.1 Ring shear test on the sample from source area	92
6.3.1.1 Saturated undrained speed-control ring shear test	92
6.3.1.2 Saturated drained torque-control ring shear test	94
6.3.2 Examining the Motion of Failed Landslide Mass on the Rice Plants Based on Ring Shear Test	97
6.4 Summary	100
7. CONCLUSIONS	101
PAPER FOR THE BASIS OF THIS THESIS	103

ACKNOWLEDGEMENTS	104
BIBLIOGRAPHY	105
CAPTIONS AND LIST OF SYMBOLS	118
APPENDIX	129

Chapter 1

INTRODUCTION

Landslide hazard is a world wide big problem confronting the developing of economics and constructions in mountainous areas. It results in tremendous lost of lives and properties almost every year. Among those hazardous landslides, fluidized landslides are of the most destructive, for its high disaster potential and high frequency of occurrences.

Fluidized landslides are usually characterized by high mobility and long run-out distance, and then necessarily followed by tremendous lost of lives and properties. They are always the result of liquefaction, a process during which high pore water pressure is generated and soil mass losses a great part of its strength and shows the behaviour of liquid. It can be triggered by dynamic effects, such as earthquakes (Seed 1968; Inokuchi 1985; Ishihara et al. 1990; Sassa 1996; Sassa et al. 1996), or by static effects, such as rainfall (Eckersley 1985; Sassa 1998a), melted snow (Marui 1996; Sassa 1998b; Sassa et al. 1997a), or other factors, such as engineering activities. Both man-made structures, such as colliery spoil tips (Bishop 1973) and mine tailings dams (Lucia 1981), and natural slopes, particularly those in the sub-aqueous environment, are susceptible to failure and subsequent fluidized motion.

Although there were so many fluidized landslides had been reported and studied, and there were some knowledge had been built up, the mechanism of this kind of failure is kept less understood. And even more, this kind of failure is still in a growing tendency, accompanying the urbanization, further development toward mountainous areas, and the changing of globe environment. For example, just in Japan, many disastrous fluidized landslides happened in recent years, such as the December 1996 Gamahara torrent debris flow, Niigata Prefecture, the July 1997 Harihara *landslide–debris flow* (here it worth to note that the description of several noun combinations to identify the multiple types of material and movement involved in a complex or composite landslide is following that described in detail by Turner and Schuster, 1996), Kagoshima Prefecture, the August 1998 Taiyo-no-kuni long run-out landslide, Fukushima Prefecture, and the June 1999 *landslide–debris flows*, Hiroshima Prefecture, etc. All of them were triggered by snow melting or heavy rainfall, and of tremendous hazards with great loss of lives.

To prevent the further occurrence of these kinds of failures, or at least to mitigate these kinds of hazards, it is urgent to make the triggering mechanism clear and make the prediction of motion of failed mass with high reliability.

1.1 BACKGROUND OF THIS STUDY

As reported in many literatures, fine sands are easier to suffer from liquefaction failure (Kramer 1988; Thevanayagam 1998). Meanwhile, it has been pointed out that silt and silt-clay mixture are more prone to suffer form liquefaction failure with large resulting run-out distance, basing on many field observations (Bishop 1973; Eckersley 1990; Ishihara 1990; Kokusho 1999; Seed 1968; Turner & Schuster 1996). However, the undrained shear behaviour of this kind of soil is not very clear. For evaluating the liquefaction potential of this kind of soil, there is no guideline available based on their density, void ratio, plasticity index, standard penetration values, or any other simple soil property. And even more, there is confusion on the influence of clay content, plasticity

index, and void ratio, as pointed out by Guo & Prakash (1999). For example, by performing series tests on loose samples prepared with varying percentages of both plastic and nonplastic fines ($<74 \mu\text{m}$) and nonplastic fine sand ($>74 \mu\text{m}$), Pitman *et al.* (1994) found that undrained brittleness decreased as the fines content, for both plastic and nonplastic type, increased; at a fines content of 40% the stress path indicated only strain hardening towards steady state. Another research carried out by Ovando-Shelley and Perez (1997) had pointed out that within limited range of clay content, the presence of clay increases the potential for generating excess pore pressure during undrained loading, and also reduces strength and stiffness. From these researches, it could be concluded that the undrained shear behavior of silt and silt-clay mixtures is not very clear and needs further extensive scrutiny. Therefore, the fluidization behavior of sands with different grain sizes and fine-particle content would be the main focus of this research.

As mentioned above, fluidized landslide is always the result of liquefaction. Therefore, many researches on the mechanism of this kind of failure were mainly concentrated on the liquefaction behaviour of soil.

Liquefaction of sands due to cyclic loading has received a great deal of attention since the Niigata earthquake, 1964, Japan (Yoshimi *et al.* 1977; Seed 1979; Finn 1981). In addition, static liquefaction due to monotonic increase of static loading has been studied in recent years (Castro 1969; Casagrande 1976; Poulos 1981; Poulos *et al.* 1985). And it was found that loosely compacted sands could exhibit a strain-softening response during undrained loading, which would result in the quick failure of liquefaction. Based on the tremendous experimental results of mostly triaxial tests, there were many sounds good conclusive remarks on the undrained shear behaviour of soils had been made. And among them, the most appealing one idea for studying the ultimate state of sands subjected to shearing might be the concept of critical void ratio line (Casagrande 1936). This hypothesis is that sand, which plot above the critical void ratio line in their situ

state, would be susceptible to liquefaction under undrained conditions, while those below, i.e. in medium or dense state, would be safe against liquefaction failure.

However, an investigation of the Fort Peck Dam slide hold by Casagrande himself showed sand, which according to the hypothesis of critical void ratio line should be safe against liquefaction, had actually liquefied with a very large loss in strength (Casagrande, 1971). Meanwhile, recent undrained ring shear tests showed that liquefaction could be triggered even in very dense sand due to grain crushing accompanying increasing shear displacement. Based on the undrained ring shear tests results, a concept of sliding-surface liquefaction was newly proposed by Sassa (1996), with which many fluidized landslide failure could be interpreted. And therefore, a new insight should be provided into the analyzing approach of fluidized failure. Meanwhile, because there is no limitation of shear displacement in ring shear apparatus, it enables the grain crushing to be complete and then makes it possible to study the ultimate steady state of sand at vast range of densities, which is important for analyzing the ultimate steady of a real fluidized landslide on the field.

Nevertheless, as has been pointed out by Eckersley (1990), the understandings on liquefaction of sand had relied almost entirely on laboratory tests on small specimens under idealized conditions; and meanwhile, although most of the laboratory work has involved undrained loading, this is not in itself a prerequisite for liquefaction (Sladen *et al.* 1985). Hence, it is highly desirable to confirm the observations obtained from undrained tests by measuring processes in real fluidized landslides. This stimulated the author to perform flume tests on rainfall-induced fluidized landslides that will be elaborated in detail in Chapter 5 of this thesis.

In the analysis of potential hazards of a fluidized landslide, the prediction of run-out distance is a most important aspect. Among the factors affecting the possible moving speed and run-out distance, the generation and maintaining of pore pressure within the

failed mass are the most important controlling factors. Using a simple apparatus to rotate samples (sand with different grain sizes and contents of loess) and water inside a double cylinder, the variation of pore pressure in relation to rotating velocity was observed by Sassa. (1988a). And it was pointed out that pore pressure increases with increasing rotating velocity, and the change of pore pressure in sample with finer grain size is greater while the rotating velocities are the same. This conclusion is used to interpret the rapid motion of liquefied mass in flume tests:

It is highly desirable to examine these understandings obtained from laboratory tests through a real fluidized landslide. Therefore, case study is performed on a fluidized landslide triggered by August 1998 heavy rainfall, Fukushima Prefecture, Japan, and basing on the ring shear tests results, the initiation and motion mechanism are analyzed in Chapter 6.

1.2 PURPOSE OF THIS RESEARCH

The purpose of this thesis is to study the fluidization behavior of sand with different fine-particle contents. Liquefaction (including mass liquefaction and sliding surface liquefaction) is used to interpret the rapid motion of fluidized landslides. By changing test conditions, factors affecting the generation of pore pressure and the resulting deformation/motion were examined in three different series tests, and the fluidization mechanisms were analyzed. These three series experimental studies are as follows:

- (1) To examine the fluidization behavior of shear zone and provide a new insight into the analysis of liquefaction susceptibility, using a newly developed ring shear apparatus, a series of undrained ring shear tests was conducted on sand. Based on the tests results, the effects of relative density, initial stress state, and samples (with different grain sizes and fine-particle contents) on the undrained shear behaviour were examined. Basing on the tests results, the fluidization mechanism in the shear zone was discussed.

- (2) To examine the fluidization behavior of landslide mass, the second phase of laboratory investigation involved in documenting the behaviour of rainfall-induced landslides in a small flume. By using different samples and changing sample's initial density, the effects of these factors on the generation of pore pressure and resulting motion were examined; and then the initiation process and motion of fluidized landslides were analyzed
- (3) The third phase of the experimentation is to examine the pore pressure generation in fluidized landslide mass during motion. It is a complementary test study for flume tests. Using a simple apparatus to rotate samples (sands with different content of loess) and water inside a double cylinder, the variation of pore pressure in relation to rotating velocity for samples with different loess content was observed, and the maintaining of pore pressure during motion was discussed.
- (4) The fourth is case study on a fluidized landslide triggered by August 1998 heavy rainfall, Fukushima Prefecture, Japan. On the basis of laboratory ring shear test results, the initiation and motion mechanism of this fluidized landslide were examined. It was found that high grain crushing susceptibility and high content of fine particles made the accumulation and maintaining of high pore pressure possible, and then enabled the failed soil mass to slip out from the source area with high mobility and travel a large distance on the horizontal paddy field.

1.3 OUTLINE OF THIS THESIS

Following this introductory chapter, Chapter 2 summarizes the developing history of liquefaction, and some fundamental concepts on liquefaction, such as *mass liquefaction*, *sliding surface liquefaction*, *steady state line*, *collapse surface*, *static liquefaction resistance*, *brittleness index*, and *apparent friction angle*, etc., are introduced. Meanwhile, some concepts concerning on the resulting deformation/motion of fluidized mass, such as *flowslide*, *rapid slide motion* etc. are introduced also.

Chapter 3 mainly introduces the characteristics of samples and the test apparatuses employed in this research. In the present stage, to make a basic understanding on the fluidized failure behaviour, fine silica sands (no. 7 and no. 8) are used in all the tests. To investigate the effects of fine-particle content on the fluidized failure behaviour, finer silica sand (no. 8) and loess were used, and their characteristics are presented in Section 3.1. Section 3.2 gives a detailed description of an almighty undrained ring shear apparatus (DPRI-Ver.6) newly developed and improved by Sassa (1997) and its operation method; meanwhile, the undrained shear test procedures are elaborated in detail. Section 3.3 shows the arrangement of flume test apparatus and the corresponding test procedures. Finally, in Section 3.4, a double cylinder mixing apparatus that was designed by Sassa (1988a) is presented and the test procedures are provided also.

Chapter 4 presents fluidization behavior of the shear zone, basing on the ring shear tests. Section 4.2 summarizes the experimental results, including the effects of initial relative density, initial stress state, grain size, and fine-particle (loess) content on the undrained shear behavior. On the basis of the results and observed shear deformation, the mechanism of fluidization in the shear zone is discussed in Section 4.3. These discussions include the formation of localized fluidization in the shear zone, grain crushing existing in mass liquefaction and sliding surface liquefaction, the collapse behavior of loose sand within the shear zone, brittleness index at different stress states, and effects of grain size and fine-particle (loess) content on the fluidization behavior of shear zone; meanwhile, to examine the maintaining of generated pore pressure within the shear zone, drained shear tests results on different samples are presented.

Chapter 5 summarizes the phenomena of rainfall-induced landslide failure in flume tests and the pore pressure maintaining mechanism during motion. Section 5.3 provides a general introduction of the observed phenomena. On the basis of monitoring the sliding distance and pore pressures, the process of excess pore pressure generation in relation to soil displacement is discussed. And then in the followed section, Section 5.4, the effects

of initial void ratio on the generation of pore pressure and resulting motion of landslide mass are examined. In section 5.5, effects of grain size and fine-particle (loess) contents on the excess pore pressure generation and resulting motion of landslide mass are presented. To examine the maintaining of pore pressure during motion, Section 5.6 presents the pore pressure maintaining mechanism during motion. Using a simple but valid apparatus to rotate samples (sands with different content of loess) and water inside a double cylinder, the variation of pore pressure in relation to rotating velocity is observed. And then the analysis on the initiation process and motion of fluidized landslides is carried out in Section 5.7.

Chapter 6 presents the results of case study on a fluidized landslide triggered by August 1998 heavy rainfall, Fukushima Prefecture, Japan. Section 6.2 gives a general introduction of this landslide. Three sets of ring shear tests are performed to examine the initiation and motion mechanism of this fluidized landslide. The tests results and analyses are illustrated in Section 6.3.

In the following chapters, Chapter 7, the analyses on the test results are performed, and the corresponding conclusions are presented.

Chapter 2

CONCEPTS AND KEY WORDS FOR FLUIDIZED LANDSLIDES

2.1 LIQUEFACTION

2.1.1 Liquefaction History

As stated by Castro (1969), perhaps the first explanation of the phenomenon of liquefaction was published by K. Terzaghi (1925) in his book, and transcribed in one of his late papers (Terzaghi 1956) as:

“Liquefaction can occur only on the condition that the structure of a large portion of the sedimentary deposit is metastable.....if the soil is saturated, at the instant of collapse the weight of the solid particles is temporarily transferred from the points of contact with their neighbors onto the water. As a consequence, the hydrostatic pressure at any depth z increases from its normal value $z\gamma_w$ by an amount u_w which is close to the submerged weight $z\gamma_s$ of the sediment located between the surface and depth z .”

The resulting slope failures Terzaghi called “**subsidence flow**” Terzaghi (1925) used the term “**mobility**” to describe the condition of sand during liquefaction failures.

In the history of liquefaction, one important discovery may be traced back to the study of Reynolds (1885). During tests, Reynolds discovered that shear deformation of sand is

accompanied by volume changes, i.e., loose granular materials decrease in volume when sheared, while dense granular materials increase in volume. Reynolds termed this property of granular materials “dilatancy”

Nevertheless, the most important and creative study was carried out by Casagrande (1936), 50 years later. And then, the significance of the volume changes during shearing in relation to the shear strength of sand, and in particular to liquefaction, was more clearly recognized. Through a series of drained strain-controlled triaxial tests, Casagrande found that initially loose and dense sand at the same confining pressure approached the same density when sheared to large strains. The void ratio corresponding to this density was called the “critical void ratio” Corresponding to this tendency, if a sand is saturated and kept in undrained condition, pore water pressure would be resulted in, and then the shear resistance will be reduced subsequently, which, if of substantial magnitude, may result in a flow slide. Performing tests at various effective confining pressures, Casagrande found that the critical void ratio varied with effective confining pressure. Plotting these on a graph produced a curve, which is referred to as the critical void ratio (CVR) line (Figure 2.1). The CVR line constituted the boundary between dilative and contractive behaviour drained triaxial compression. A soil in a state that plots above the CVR line exhibits contractive behaviour and vice versa.

Although there were some results on liquefaction had been obtained in the earlier stage, it was after the 1964 earthquake of Niigata, Japan, broader attention was attracted to the phenomenon of liquefaction, and then the importance of earthquake-induced liquefaction was underlined. In that earthquake disaster, extensive damage to structures was triggered due to liquefaction of the sandy deposits on which they were seated. The significance of the loss of life and properties resulted from liquefaction failure during the earthquake generated a large amount of research to evaluate the phenomenon, and there were some appealing approaches had been proposed to provide mitigative

measures against liquefaction.

Among the several methods of analyzing liquefaction susceptibility, the steady state approach may be the most appealing one and widely used in practice. On the basis of critical void ratio, Castro performed an important series of undrained, stress-controlled triaxial tests. In these tests, three different types of stress-strain behavior depending on the soil state were found (see Figure 2.2). Dense specimens dilated with increasing effective confining pressure and shear stress. Very loose samples collapsed at a small shear strain level and failed rapidly with large strains. Castro called this behaviour of very loose sample "liquefaction"-it is also commonly referred to as "**flow liquefaction**". Medium dense soils initially exhibiting contractive behaviour, the same behaviour as the loose samples but, after initially exhibiting contractive behaviour, the soil transformed and began exhibiting dilative behavior. Castro referred to this type of behaviour as "**limited liquefaction**". Castro plotted the relationship between effective confining pressure and void ratio at large strains for these undrained, stress-controlled tests. Castro referred to the curve, produced by this plot, which is similar to the CVR line for the drained strain controlled tests performed by Casagrande, as the "**Steady State Line**" (SSL). The important assumptions in the steady state approach are that the sand has a unique steady-state line in void ratio-effective stress space, and that this line can be determined from the results of undrained tests on loose specimens of sand (Castro 1969, Castro and Poulos 1977, Poulos 1981). And the essential criterion of this approach is that saturated soil with void ratio and effective confining stress located below the steady state line has no susceptibility to suffer liquefaction failure.

Nevertheless, recent undrained ring shear tests showed some inconsistent tendency with these conclusions obtained from triaxial tests, medium and dense sand being able to suffer from liquefaction failure due to grain crushing along sliding surface. In the studies of landslides triggered by the Hyogoken-Nambu earthquake through undrained ring shear tests, a new concept of sliding surface liquefaction was proposed by Sassa

(1996). Sliding surface liquefaction is a special kind of liquefaction; it differs from the pronounced liquefaction (mass liquefaction) (Sassa, 1996).

For his doctoral thesis, F. W. Wang (1998) performed a series of ring shear tests under Professor Sassa's guidance, to determine the relationship between the grain crushing possibility of sand in dry state and the sliding surface liquefaction potential when subjected to undrained shearing. He found that grain crushing is a key factor for rapid landslide motion, no matter the failure was triggered by cyclic loading or by static loading.

2.1.2 Definition of Liquefaction

In order to prevent confusion it is necessary to differentiate between the different uses of the term liquefaction by the different investigators mentioned in the preceding section.

As aforementioned, corresponding to the undrained shear behaviour in triaxial tests, there are three kind of response, and these processes were termed as liquefaction, limited liquefaction and dilation, respectively (Castro 1969). However, in ring shear tests, the undrained shear behaviors are more tending to behave in two different kinds of way: with or without strain softening (collapse behavior) that would result in the quick liquefaction failure, i.e., mass liquefaction and sliding surface liquefaction. And here in the thesis, they are defined as follows.

2.1.2.1 Mass liquefaction

To make a distinguish between the normally understood liquefaction and newly proposed sliding surface liquefaction, and meanwhile, considering that the normally understood liquefaction was necessarily entailed flow motion of soil mass in the tremendous literatures (Terzaghi 1956; Bishop 1973; Kramer 1988; Eckersley 1990; Ishihara *et al.* 1990), Sassa (1995) utilized this term "mass liquefaction" to refer to the

normally defined liquefaction.

With respect to mass liquefaction, as appeared in the literatures, there are two different definitions. One is the “zero effective stress definition”, and the other is “strain softening and collapse definition”

Zero effective stress definition

This definition was used by Seed (1966) to refer to this kind of condition at which zero effective stress was reached as a result of accumulation of excess pore pressure during cyclic loading. As a result of this kind of liquefaction, the liquefied soil loses its shear strength and will not be able to carry any shear stress. This definition has some limitation once it came into being. It is obvious that this definition was not suitable for the anisotropically consolidated dense soils under undrained cyclic loading, because the condition of zero effective stress will not occur if no further shear stress develops. Meanwhile, as stated by Casagrande (1971), the zero effective stress is impossible to be reached when the liquefaction failure happened on the soil mass on a slope.

Strain softening and collapse definition

This definition is based on the concept of “critical void ratio” proposed by Casagrande (1936). Casagrande (1938) elaborated on the fact that the critical void ratio decreases with increasing confining pressure, and he concluded that during a flow condition, the effective stresses are reduced to the effective confining pressure for which the critical void ratio is equal to the in-situ void ratio of the sand. The shear strength of the sand would thus be reduced to a value, which is only a function of its void ratio. If a slope or embankment were high enough so that the shear stresses are much greater than the reduced shear strength of the sand, a flow failure would result. Thus, for the first time, it was proposed that the occurrence of liquefaction is not necessarily related to a zero or almost zero effective stress condition, but rather to a reduction of the effective stresses which is large enough so that the shear strength would drop substantially below the

existing shear stresses in the soil mass. If these shear stresses are large, as under a high dam or natural slope, catastrophic liquefaction may develop while the effective stresses in the flowing mass remain relatively large.

Based on the thought of Casagrande and the results of undrained monotonic loading triaxial tests on saturated sand, Castro (1969, 1975) referred to **liquefaction** as a process during which a soil mass suddenly loses a large proportion of its shear resistance when subjected to monotonic or cyclic loading at constant volume (i.e., undrained loading conditions) so that the mass undergoes very large unidirectional shear strains, and flows in a manner resembling a liquid. The flows will be continued until the shear stresses are as low as or lower than the reduced shear resistance. Thus, the prerequisite condition for liquefaction failure is the presence of driving static shear stresses that exceed the reduced shear resistance of the soil.

As stated by Soroush (1996), *“there are at least two advantages of the definition of liquefaction proposed by Castro; one is that it enables one to unify descriptively liquefaction cases induced by both cyclic and monotonic loading. The second is that it enables one to introduce some strength, namely residual or steady state strength, for liquefiable materials in any stability analysis.”*

The definition of liquefaction proposed by Castro is used in this thesis as the definition of mass liquefaction. It is evident that this kind of liquefaction is mainly due to the destruction of metastable soil structure. And the essential features of this definition are that liquefaction involves loss of strength and sudden loss of limiting equilibrium. **Figure 2.3a** presents a schematic illustration of mass liquefaction defined as above.

2.1.2.2 Sliding surface liquefaction

The concept of sliding surface liquefaction was newly proposed by Sassa (1996) in the studies of landslides triggered by the Hyogoken-Nambu earthquake through undrained

ring shear tests.

Sliding surface liquefaction is a special kind of liquefaction; it differs from the pronounced mass liquefaction. Sliding surface liquefaction is a phenomenon that liquefaction only takes place along the sliding surface. With increasing shear displacement, accompanying the grain crushing, pore water pressure builds up gradually, and shear resistance decreases slowly, finally pore pressure reaches to a high value, and shear resistance tends to a substantial constant correspondingly. Therefore, sliding surface liquefaction can take place even in medium or dense soil structure; it is a localized liquefaction limited in the shear zone both in laboratory and on the field.

Figure 2.3b illustrates the definition of sliding surface liquefaction. And then the difference between mass liquefaction and sliding surface liquefaction could be recognized through the destruction of soil structure and the corresponding effective stress paths.

Considering both of these two kinds of liquefaction could at least result in rapid motion after the liquefaction failure is initiated, in this thesis, liquefaction would be used to refer to both mass liquefaction and sliding surface liquefaction, when have no specific declaration.

2.2 STEADY STATE LINE AND COLLAPSE SURFACE

2.2.1 Steady State Line

As aforementioned, based on the concept of critical void ratio defined by Casagrande (1936), and on the supportive results obtained from undrained monotonic loading tests on saturated sand, Castro (1969, 1975) introduced a steady state line. Thereafter, the steady state approach of analyzing liquefaction susceptibility was postulated and widely used in practice. The important assumptions in these analyses are that the sand has a unique steady-state line in void ratio-effective stress space, and that this line can be

determined from the results of undrained tests on loose specimens of sand (Castro, 1969; Castro and Poulos, 1977; Poulos, 1981). As a key characteristic of the steady state, the concept of the steady state of deformation proposed by Poulos (1981) is necessary to quote here:

“The steady state of deformation for any mass of particles is that state in which the mass is continuously deforming at constant volume, constant normal effective stress and constant velocity. It is achieved only after all particle orientation has reached a steady state condition and after all particle breakage, if any, is complete so that the shear stress needed to continue deformation and the velocity of deformation remain constant.”

Figure 2.4 presents an illustration of the steady state of a sand as a line in p' - q - e space, where p' , q , and e are the mean normal effective stress, the deviator stress and the void ratio, respectively. **Figure 2.4a** shows the actual stress paths in a spatial manner in three-dimensional space. It could be seen that the projections of this steady state line on (e - p') plane (**Figure 2.4b**) and (e - q) plane (**Figure 2.4c**) are curves, while that on (p' - q) (**Figure 2.4d**) is a straight line.

With respect to the uniqueness of steady state line, there are some disputations. Some laboratory tests results have shown that for uniform sand, the steady state line is just a function of void ratio, and independent of the effective stress path and the initial effective stress value (Been and Jefferies 1985; Been et al., 1991, 1992; Castro, 1969; Castro and Poulos, 1977; Ishihara, 1993; Poulos, 1981). For example, Been et al (1991, 1992) examined the undrained shear behaviour of fine sand, and concluded that steady state of the sand is unique, irrespective of stress path, sample preparation and initial stress state. By conducting compression and extension triaxial tests on water deposited sand, Vaid et al (1990) concluded that at a given void ratio, the steady state strength is

smaller in extension than in the compression, and the difference increases as the sand gets looser. However, Been et al (1991) explained that the difference in the steady state strength of the sand in compression and extension is due to the difference in mapping of steady state line in the p' - q plane.

2.2.2 Collapse Surface

Based on the laboratory tests and back analysis on a large-scale slide, which was resulted from the liquefaction of the berm sand during the hydraulic placement of an artificial island berm in the Beaufort Sea, Sladen et al (1985) proposed a collapse surface concept. It was found that a necessary condition for liquefaction is that the soil state lies on this surface. This collapse surface concept is fundamentally an extension of the steady state concepts proposed by Casagrande, Poulos, and Castro, and follows in many respects the principles of critical state soil mechanics.

Test results obtained by Sladen et al (1985) suggested that the collapse surface may be observed by plotting the results of undrained triaxial compression tests in a normalized p' - q plane. The envelope of the peak strengths on this normalized plane forms the collapse surface. Figure 2.5 shows the collapse surface suggested by Sladen et al. (1985).

Tests results showed that peak shear strength depends on the effective stress path and also on the initial stress, and the post peak strain softening behavior depends on both void ratio and initial effective stress. For a soil with constant void ratio, the higher the in situ stress, the more brittle the soil and, hence, the higher the softening of the soil.

2.3 STATIC LIQUEFACTION RESISTANCE AND BRITTLINESS INDEX

It had been pointed out by Seed and Hon (1987) that in general, there are two main problems confronting the soil engineer dealing with a situation where soil liquefaction may occur: (1) Determining the stress conditions required to trigger liquefaction; and

(2) determining the consequences of liquefaction in terms of potential sliding and potential deformation. With these aspects, two parameters, **Static liquefaction resistance** and **Brittleness index**, could be effective.

2.3.1 Static Liquefaction Resistance

Considering that both in the field and in the laboratory, liquefaction can only occur when shear stresses under undrained conditions are greater than or equal to those required to initiate liquefaction, Kramer and Seed (1988) proposed a new concept of “**static liquefaction resistance**” to evaluate the liquefaction potential or factor of safety against liquefaction at a given site. The **static liquefaction resistance** was defined as the increase in shear stress under undrained conditions required to initiate liquefaction, and formulated as:

$$R_L = \tau_f - \tau_i \dots\dots\dots(2.1)$$

where τ_f = peak undrained shear strength (subscript *f* means failure), τ_i = initial shear stress existed in soil element before undrained shear load was applied (subscript *i* means initial). A schematic illustration of this concept in triaxial tests is given in **Figure 2.6**, where the abscissa presents the axial strain at triaxial tests, and ordinate is the deviator stress. Considering that in ring shear tests, only the shear displacement could be obtained accompanying the increasing shear stress, here in the thesis the shear displacement will be used as the abscissa to substitute the axial strain in triaxial tests. The static liquefaction resistance in ring shear test could be interpreted by **Figure 2.7**, a schematic illustration of shear stress-shear displacement curve in ring shear test.

2.3.2 Brittleness Index

The reduction in soil shear strength resulted from the initiation of liquefaction may be large or small, and it may depend on the initial void ratio, stress state and shear history. The magnitude of the strength loss after initiation of liquefaction does not directly affect

the safety against initiation of liquefaction, but it has a large effect on the consequences of liquefaction. After liquefaction has been initiated in an element of soil, that element deforms until it reaches the steady state of deformation. In this process, the shear resistance drops from the peak undrained shear strength to the residual (steady state in most situation) shear strength. To analyze the post-rupture behaviour, Bishop (1967) proposed a parameter “**Brittleness index**” to express the reduction in undrained strength of a strain-softening material, which was defined as:

$$I_b = (\tau_p - \tau_r) / \tau_p \dots\dots\dots(2.2)$$

Where τ_r is the residual undrained shear strength, namely the steady-state shear strength in many undrained shear tests. A greater brittleness index indicates a greater reduction in shear strength that means progressive development of large deformation could be resulted in after the initiation of liquefaction.

In this paper, these indexes will be used to analyze the liquefaction susceptibility and post failure behaviour in some places of examination on the undrained shear behaviors.

2.4 FLUIDIZED LANDSLIDE

Even though slope failures may threaten lives and property, not all of them present the same degree of danger. It is well known that the resulting hazards are mainly dependent on the velocity of failed slopes and the possible run-out distance.

Landslide velocity could be in a large range, from extremely slow to extremely rapid, and therefore, their resulting hazard may be essentially different. Based on huge number of case histories and observations, Cruden and Varnes (1985) introduced a detailed definition of landslide velocity classification, based on the proposition given by Varnes (1978). **Figure 2.8** presents the detailed definition, where the landslide velocity is divided into seven classes, and the boundary between each class is enumerated. An important limit appears to lie between very rapid and extremely rapid movement, which

approximates the speed of a person running (5 m/sec). Table 2.1 illustrates the probable destructive significance of the seven velocity classes on the new landslide velocity scale.

Table 2.1

Definition of Probable Destructive Significance of Landslides of Different Velocity Classes (after Cruden and Varnes, 1985)

Landslide Velocity Class	Probable Destructive Significance
7	Catastrophe of major violence; buildings destroyed by impact of displaced material; many deaths; escape unlikely
6	Some lives lost; velocity too great to permit all persons to escape
5	Escape evacuation possible; structures, possessions, and equipment destroyed
4	Some temporary and insensitive structures can be temporarily maintained
3	Remedial construction can be maintained with frequent maintenance work if total movement is not large during a particular acceleration phase
2	Some permanent structures undamaged by movement
1	Imperceptible without instruments; construction possible with precautions

From Figure 2.8 and Table 2.1, it could be concluded that extremely rapid landslides are of most disaster. Among those most hazardous landslides, fluidized landslide is typical and representative, not only for its characterization of extremely rapid moving velocity and larger run-out distance, but also for its occurrence with high frequency. And therefore, to mitigate this kind of disaster, the study presented in this thesis is focusing on the fluidized landslide.

2.4.1 Definition of Fluidized Landslide

As well known, fluidized landslide is a result of liquefaction failure. Therefore, **Fluidized landslide** used in this thesis refers to those slope failures, where high pore pressure is generated and the shear strength of soil mass reduced greatly; and as the consequence, the failed soil mass shows high mobility with large run-out distance.

2.4.2 Motion of Fluidized Landslide

Fluidized landslides are usually characterized by high mobility and large run-out distance; therefore, it seemed not enough to evaluate this kind of failure just according to the velocity. Different characterization of movements will have differing resulting disaster. According to the distinguished features of fluidized landslides, the movement could be classified into two series: flowslide and rapid slide (as a whole block) motion. And their detailed characteristics will be described in the followings.

2.4.2.1 Flowslides

Flows, when used to describe the mass movements as well as mass transport, are referring to this kind of move that solid grains shear over one another and over a stationary bed, and move like a “viscous mass” Therefore, “flowslides” is used to refer to those slope failures that are characterized by general disintegration of the sliding mass with a rise in pore-water pressure and by development of fluid-like motion (Bishop, 1973; Eckersley, 1985, 1990; Spence & Guymer, 1997). They can be distinguished from “slides,” which have a relatively intact soil mass above the sliding surface (Bishop, 1973). Usually, this kind of failure occupies only a few minutes.

The requirements for this kind of failure are:

- Post peak behavior of the soil in undrained/drained loading conditions should be strain softening; the loading can be either monotonic or cyclic
- Initial shear stress must be higher than the steady state strength of the soil

- Free boundaries for flowing

2.4.2.2 Rapid slide motion

The term slide usually refers to those movements of materials along recognizable shear surfaces. Due to the differences in shear strength and/or stress state between the basal or bottom layer and the upper material, when the failure is resulted in, a sliding surface would be formed, and then the upper material would slide along this surface as a whole, just like a rigid block, riding over the bottom layer. The difference between flowslide and slide (plug slide) could be illustrated by Figure 2.9, a schematic explanation of these two kinds of movements.

The character of this category of movements is that liquefaction is located on a limited zone; and there are two possibilities for this kind of failure to happen:

- (1) There exists a sand seam or thin sand layer underlying an otherwise stable mass of soil; or
- (2) The soil particle is crushable. When shear stress is greater enough such that shear failure could be initiated, thereafter, accompanying the grain crushing along with shear displacement, excess pore pressure within the shear zone is built-up gradually, and shear resistance is reduced consequently, finally, high speed slide would be necessarily resulted in, i.e. sliding surface liquefaction failure.

2.5 APPARENT FRICTION ANGLE FOR LANDSLIDE

Apparent friction angle (ϕ_a) for landslide was proposed by Sassa (1984) to present the mobilized coefficient of friction for soil mass in motion, in substitution of the internal friction angle used in the field of soil mechanics. It is defined as an inverse tangent function of the ratio of landslide height to landslide total length (see Figure 2.10a), and formulated as follows:

$$\tan \phi_a = h / x \dots\dots\dots(2.3)$$

Where, h : presents the height of landslide; x : expresses the horizontal travel distance of landslide. As stated by Sassa (1985), this apparent friction angle is chiefly the results of combination of the real internal friction angle during motion and the pore pressure during motion, and then it is proved by Sassa and formulated as (1985):

$$\tan \phi_a = \frac{\sigma - u}{\sigma} \tan \phi_m \dots\dots\dots(2.4)$$

where, ϕ_m : Internal friction angle during motion; σ : Normal stress; u : Pore pressure. For a landslide where pore pressure is generated in the shear zone, this apparent friction angle could be predicted through the undrained ring shear test results effectively (Sassa 1984), and Figure 2.10b illustrates the determination method. As shown, it is computed by the ratio of undrained residual shear strength (usually undrained steady state shear strength) to initial normal stress in ring shear tests, and therefore, it is dependent on the initial normal stress, greater initial normal stress resulting in smaller apparent friction angle. Usually, smaller friction angle shows higher mobility.

As the result of liquefaction, fluidized landslides usually have smaller apparent friction angles. With respect to this aspect, some typical fluidized landslides could be listed out.

- (1) Saleshan fluidized landslide (Zhang and Sassa 1992): this landslide occurred at the Saleshan mountain, Gansu Province, China on 7th March 1983, and the landslide mass slid down from a steep slope at a high speed (13-14 m/sec at average), rode on the quaternary alluvium and moved over about 800 m until a river. According to field survey result, the apparent friction angle was 10.8 degrees, while that from the undrained ring shear test results was 10.2 degrees.
- (2) Harihara fluidized landslide: this landslide, occurred at the Harihara torrent, Izumi City, Kagoshima Prefecture, was triggered by the heavy rainfall on July 1997. The failed soil mass of $2 \times 10^5 \text{ m}^3$ in volume run out a large distance of approximately 830

m, and brought great losses of lives and properties. According to field survey, this fluidized landslide showed an apparent friction angle of 10.9 degrees.

- (3) Nikawa landslide: This fluidized landslide was triggered by the January 17, 1995 Hyogoken-Nambu earthquake in Japan, and had destroyed 11 houses and killed 34 persons. According to Sassa et al. (1995, 1996), this landslide was 110,000~120,000 m³ in volume and 175 m in run-out distance, and the apparent friction angle was approximately 10.0 degrees.
- (4) Hiegaesi fluidized landslide: This landslide, that will be studied late in this thesis, was located in Nishigo Village, southern Fukushima Prefecture, Japan, and triggered by the heavy rainfall on August 1998. Irrespective of its small scale (approximate 1200 m³ in volume), the failed soil mass traveled a large distance of 97 m, and deposited on a paddy field, with the apparent friction angle being 11.2 degrees.

From these typical fluidized landslides, it could be seen that they were similar in their apparent friction angle: approximate 10 degrees. Therefore, here in this thesis, to judge whether fluidization of soil mass in undrained ring shear tests has happened or not, a criterion of apparent friction angle obtained from undrained ring shear test being less than 10 degrees will be used, that is:

$$\tan \phi_m = \frac{\tau_s}{\sigma_i} \leq \tan 10 \dots\dots\dots(2.5)$$

where, τ_s : undrained shear strength at steady state; σ_i : initial normal stress

2.6 OTHER CONCEPTS USED IN THIS THESIS

The followings are the definitions of some concepts to be used in this thesis.

Grain crushing: a process during which soil grains are crushed into smaller size, when the acting stresses acting on soil grains are greater than their strengths. It is also referred

to as particle breakage in some literatures (Lade et al. 1996).

Pore pressure coefficient in direct-shear state, B_D : a parameter that was proposed by Sassa (1985a) to illustrate the saturation degree of sample in direct shear condition, on the conceptual basis of pore pressure coefficient, B , proposed by Skempton (1954). It is a ratio of pore pressure response to the normal stress increment under undrained condition, and formulated as:

$$B_D = \frac{\Delta u}{\Delta \sigma} \dots\dots\dots (2.6)$$

where Δu and $\Delta \sigma$ are the increment of pore pressure and normal stress, respectively. If $B_D \geq 0.95$, it could be considered that a full saturation has been reached.

Relative density (D_r): defined by Terzaghi (1921), and formulated as

$$D_r = \frac{e_{max} - e}{e_{max} - e_{min}} \times 100\% \dots\dots\dots (2.7)$$

Where e_{max} presents the maximum void ratio of dry sand corresponding to the loosest state; e_{min} presents the minimum void ratio of dry sand corresponding to the densest condition; e is the void ratio of sample. e_{max} and e_{min} are measured following "JSF T 161-1990" (JSF: Japanese Society of Soil Mechanics and Foundation Engineering).

Density index (I_d): Relative density D_r is for expressing the situation that e is smaller than e_{max} (e_{max} was obtained from dry sand in loosest state). There are some cases that sand are extremely loose and their void ratio e could be greater than e_{max} . To presents the relative density of these cases, density index was used, and formulated as:

$$I_d = \frac{e_{max} - e}{e_{max} - e_{min}} \dots\dots\dots (2.8)$$

Therefore, I_d could be smaller than 0, when sand is in extremely loose state.

Contractive: A specimen is said to be contractive if it tend to decrease in volume when subjected to an increase in shear stress. Depending on whether its volume is allowed to change or is kept constant while the shear stress is increased, the volume will either decrease or the pore pressure will increase.

Dilative: A specimen is said to be dilative if it tends to increase in volume when subjected to an increase in shear stress (deviator stress). Depending on whether its volume is allowed to change or is kept constant while the deviator stress in increased, the volume will either increase or the pore pressure will decrease.

Excess pore pressure: referring to the pore water pressure generated in soils under drained and/or undrained conditions. The variation of pore water pressure corresponding to the varying of normal stress under undrained condition is not included in the excess pore pressure in this thesis.

Excess pore pressure ratio (r_u): presents the ratio of excess pore pressure to the initial effective normal stress. It is an index to evaluate the degree of liquefaction, and formulated as:

$$r_u = \frac{u - u_i}{\sigma_i - u_i} \dots\dots\dots(2.9)$$

Where, u_i : initial pore pressure; u : pore pressure; σ_i : initial normal stress. When $r_u = 1.0$, it means a complete (full) liquefaction.

Chapter 3

SAMPLE, APPARATUS AND TEST PROCEDURE

3.1 SAMPLES EMPLOYED IN THE TESTS

It was found that fine sands are easier to suffer from liquefaction failure (Kramer 1988, Thevanayagam 1998). To make the trigger of liquefaction in laboratory relatively easy, in this study, fine silica sand no. 7 (S7) and no. 8 (S8) are selected as the sample. These silica sands are kinds of sand materials for building use made from silica sandstone by mechanical grinding, comprised of 92-98 percent of subangular to angular quartz, and a little amount of feldspar. The particles ranged from fine sand to silt sizes.

To study the influence of material characteristics upon liquefaction behaviour, loess was used in this research, too. This loess, which was composed mainly of fine sand and silt, was collected from a potential landslide at Lishan, Xi'an, China. In the present work, a series of tests was conducted on the mixture of S8 and loess with loess content of 10, 20, and 30 percent, which were termed as M10, M20 and M30, respectively.

The grain-size distributions of S7, S8 and loess are shown in **Figure 3.1**. As shown in this figure, there is some amount of grains whose sizes are smaller than 0.005 mm

existing in each sample. It should be noted that those grains smaller than 0.005 mm existing in loess could be regarded as clay, while those in S7 and S8 could be just treated as fine silt or rock flour, because the grains are formed by mechanical grinding without any weathering.

Table 3.1 lists some characteristics of the employed samples. It should be noted that all these property measurements of S7, S8 and loess are followed the JSF. And the properties of M10, M20, and M30 were obtained by those of S8 and loess, using the weight average method.

Table 3.1 Properties of employed samples, S7, S8, M10, M20, M30, and loess.

Sample	S7	S8	Loess	M10	M20	M30
Mean grain size, D_{50} (mm)	0.13	0.050	0.0185	0.047	0.043	0.040
Effective grain size, D_{10} (mm)	0.074	0.018	0.0012	0.0118	0.0084	0.0057
Uniformity coefficient, U_c	2.1	3.7	19.0	4.6	6.0	8.3
Maximum void ratio, e_{max}	1.23	1.66		1.51	1.52	1.56
Minimum void ratio, e_{min}	0.70	0.85		0.73	0.73	0.73
Specific gravity, G_s	2.63	2.63	2.72	2.64	2.65	2.66

3.2 RING SHEAR APPARATUS AND TEST PROCEDURES

3.2.1 Ring Shear Apparatus

Ring shear apparatus has been widely used in the analysis of slope stability due to its advantage in shear displacement recently (Bishop et al. 1971; Bromhead 1979; Gibo 1994; Sassa 1988a, b, 1996, 1998a, b; Sassa and Fukuoka 1995; Sassa et al. 1997a, b; Tika and Hutchinson 1999). Two new sets of almighty intelligent ring shear apparatus (DPRI-Ver.5, DPRI-Ver.6) were developed and improved by Sassa and colleagues to simulate the earthquake-triggered-landslides after the Hyogoken-Nambu earthquake,

17th January 1995. In the present research, DPRI-Ver.6 was employed.

Table 3.2 The main features of the employed ring shear apparatus (DPRI-Ver.6)

Shear box	
-Inner diameter (mm)	250
-Outer diameter (mm)	350
Maximal normal stress (MPa)	2.0
Maximal shear speed (cm/sec)	214
Resolution of gap control system (mm)	0.001
Maximum data acquisition rate (readings/sec)	200
Maximum frequency of cyclic-loading (Hz)	5
Possibility of undrained test	Yes
Possibility of simulation of monitored seismic wave records by normal stress and shear stress	Yes
Automatic safeguard and alarm system for mishandling	Yes

Figure 3.2a shows a front photographic view of the DPRI-Ver.6 ring shear apparatus before its installation in the laboratory, including the operation system (controlling system and data acquisition system), and mechanical system. The main features of this apparatus are listed in Table 3.2. As illustrated in this table, the applicable maximum normal stress is 2.0 MPa (20 kgf/cm²), and the mechanical system is made relatively high and big consequently. To operate it conveniently, the blow half of the mechanical system is located under the ground of laboratory.

Figure 3.2b presents the electronic control system. As illustrated, this system consists of normal stress control, shear stress control, and gap control. Figure 3.2c shows a schematic diagram of this apparatus. In this figure, the sample is loaded by a loading

plate through an oil piston (OP_1). The loaded normal stress is measured by the load cell (N_1). The sum of the friction between the sample and the upper shear box and the contact pressure (was kept as 250 kgf in the present series tests) of rubber edge in the gap is measured by a load cell (N_2). The real normal force acting on the shear surface is obtained from the difference between the values measured by the two load cells (N_1 and N_2). This value is sent to a servo-amplifier as a feed back signal. Then, the normal stress on the shear surface is automatically controlled so as to be the same with the control signal given by the computer. The contact pressure of rubber edge is automatically controlled by a servomotor (OP_2) using the feed back signal obtained from a gap sensor (GS) with precision of 1/1000 mm. Shear stress is supplied by torque-control-servo-motors (in the right and left hand). The loaded torque is measured by torque transducers (T_1 and T_2). Using the sum of monitored values of T_1 and T_2 as the feed back signal, the loaded shear stress is automatically controlled by the servo amplifier and servomotor so as to be the same with the pre-decided value given by computer. The shear resistance acting on the shear surface is monitored by the load cell (S_1 and S_2), through which the upper half part of the shear box is restrained from rotation.

Figure 3.2d shows the shear mode of sample in ring shear apparatus briefly. The sample is laterally confined between pairs of upper and lower confining rings, and loaded normally through an annular loading platen connected to the oil piston (OP_1 in **Figure 3.2c**) through load lever, as mentioned above. The low half of the shear box is rotary in both directions, driven by a servomotor through transmission system, while the upper part is kept steady with help of two reacting torque arms, with which the shear resistance is measured. When shear failure happened, the annular ring-shaped sample will be sheared on a plane of relative rotary motion, with the lower part rotating along with rotating table.

It is worth to point out that the most essential design for undrained ring shear apparatus is the construction of undrained shear box. Its design is illustrated as **Figure 3.2e**, an enlarged diagram of the undrained edges and its surroundings, including water-pressure measurement system. Water-leakage proof is made by rolling two slices of “O” rings on the upper loading platen, and pasting rubber edges on the two confining rings of the low rotary pair. Before setting the shear box, the rubber edges are covered with friction coat of Teflon, and daubed with vacuum silicon grease. During test, a certain amount of pressing force (determined by the possible generation of pore pressure) is applied between the upper pair and rubber edges, and kept constant automatically through the gap control oil piston (OP₂ in **Figure 3.2c**). For DPRI-Ver.6, the shear box is 250 mm in inner diameter, 350 mm in outer diameter, and 150 mm in height. Pore pressures are measured by pore pressure transducers, which are connected to the gutter (4×4 mm) along the whole circumference on the inner wall of the outer ring in the upper pair. The gutter is located at 2 mm above the shear surface and covered with two metal filters, with a filter cloth between them.

Two personal computers are set for test controlling and data recording. Testing process is controlled by an operating computer. The test could be either shear torque controlled, shear speed controlled or shear displacement controlled. In the present research, to observe the shear behaviour of soil accompanying the increasing shear stress before failure, torque controlled method is selected. All the recordings of transducer are recorded automatically, while the graph of effective stress path is being drawn simultaneously by the data-recording computer.

3.2.2 Test Procedures

In this research, all the tests were carried out following the procedures listed below.

● Sample Setting

The samples were made by means of moist placement or dry deposition (Ishihara, 1993), according to different test purposes. For moist placement method, de-aired water was first added to the oven-dried samples to make the initial water content rise up to 5 percent, and then the sand was stirred evenly. After that, the sample was placed into the shear box. To make the sample uniform, while packing, the sample was placed in a series of layers of 3-cm thickness, and then each layer was tamped. For dry deposition method, the oven-dried sample was fallen into the shear box freely by layers, and each layer was and was not tamped differently to make the initial density different.

● Sample Saturation

Sample was saturated with help of carbon dioxide and de-aired water. After the sample was packed, CO₂ was then percolated through the sample to expel the air in the sample pores out, by flowing in through the lower drainage line very slowly, and discharging from the upper drainage line. Usually, this process took 4 to 12 hours, depending on the samples (for S7, S8, 4 hours are enough; for M10, M20, and M30, this duration was kept normally 12 hours). After hours of percolation of CO₂, de-aired water was infiltrated into the sample through the lower drainage line to expel the CO₂ in the sample pores from the upper drainage line. This infiltration was kept very slow with help of a very small water head. To expel the CO₂ as completely as possible, this water saturation process was usually kept 12-24 hours, depending on the samples (as mentioned above, for the mixtures of S8 and loess, this saturation process was longer also). Considering the possible effects of backpressure on tests results, during saturation, back pressure was not applied.

● Saturation Checking

To check the saturation degree of samples, B_D parameter was used in this series tests.

During checking, the sample was firstly consolidated under normal stress of 49 kPa (0.5 kgf/cm²) in drained condition. And thereafter, a normal stress increment, $\Delta \sigma = 49$ kPa, was applied in the undrained condition, and the resulting increment of excess pore pressure (Δu) was measured. Therefore, the saturation degree could be checked by the ratio (B_D) of excess pore pressure increment and normal stress increment ($\Delta u / \Delta \sigma$). As aforementioned, If $B_D \geq 0.95$, it could be considered that a full saturation has been reached. In this study, all the tests were carried out with $B_D \geq 0.95$.

● Sample Consolidation

All the samples were normally consolidated in this series tests under the pre-decided normal stress and shear stress. In the present research, most of the tests were carried out under the same initial stress state, with normal stresses being 196 kPa and shear stress being 0, except for those tests for examining the effects of stress state.

● Undrained Shearing

The studies by both Castro et al. (1982) and Sladen et al. (1985) have determined that there is no difference between the results of either load-controlled (stress) or strain-controlled tests. To allow more data to be gathered between the start point of shearing and the point where peak shear strength was mobilized, and then yield a well-defined effective stress path, torque-controlled method was selected. Corresponding to the torque control, there are three kinds of rotating gear with final speed of Low (10 mm/sec), Medium (32.3 cm/sec) and High (2.25 m/sec). To avoid the phenomenon of runaway strains in contractive sand once the peak shear stress has been reached, which usually appears in stress-controlled triaxial compression tests, in this study, the Low gear was selected in nearly almost all of the tests, except for some tests for special purposes (those tests will be illustrated separately in details in the following sections where they appear), providing that shear speed has no effects on the key results

(Hungr and Morgenstern 1984b). After consolidation, undrained shear stresses were subsequently applied at a loading rate of 0.098 kPa/sec (0.001 kgf/cm²/sec). Transducers were scanned at an interval of 1 second before the peak shear strength; after that, the sampling rate was increased to 20 samples/sec.

3.3 FLUME TEST APPARATUS AND TEST PROCEDURES

3.3.1 Flume Test Apparatus

The experimental apparatus is illustrated in Figure 3.3. The flume, with transparent sides, was 180 cm long, 24 cm wide, and 15 cm high. The flume angle is made changeable for different test requirements. To assure the same friction between the sand particles and the base of the flume as of that of sands inside the flume, silica-sand grains were glued to the surface of the flume base. At longitudinal distances $x_1 = 45$ cm, $x_2 = 90$ cm, and $x_3 = 140$ cm from the upstream end of the flume, three identical holes with diameters of 1.5 cm were drilled along the central line, as seen in Figure 3.3 (in the left part of this figure shows the placing of transducers on the flume bottom). Vinyl tubes were inserted into these holes with one end of each tube being flush with the flume bed (end A for x_3 in Figure 3.3) and the other end (end B) being connected to the pressure transducers, so that the pore-water pressure could be measured. On the side of the hole at position x_1 , a normal-stress transducer and a shear-stress transducer were installed to measure the stresses in the soils. In the place immediately close to and being in the downstream of place of x_1 , a styrene foam ball 2 cm in diameter was laid so that it connected with a linear displacement transducer through a wire. During the test, the ball buried in the sample moves together with the sample; in this manner, the time series of sliding distance can be monitored. Because of the resolution of this linear displacement transducer with rated capacity (100 cm), displacements smaller than 1.0 mm cannot be measured correctly. Therefore, to get precise measurement, a laser displacement sensor

with resolution of 0.015 mm and rated capacity of 15 mm was also used by fixing a target on the wire and shining a laser beam upon the target. A 160-g weight was attached to the other end of the wire to balance the pulling resistance of the linear-displacement transducer. At a position 3 cm above the base at the location of x_1 , a plate (3 cm \times 3 cm) with many holes was laid parallel to the base. The plate was connected to another target outside of the soils by means of a fine metal bar. Thus, by using another laser displacement sensor it was possible to monitor the normal displacement of the soils within the zone near the base. Above the flume two spray-nozzles were placed. By keeping the supplied water pressure constant with help of a pump, and adjusting the distance to the nozzles, a uniform artificial rainfall was assured. A video camera was used to monitor the entire test process from one side of the flume.

3.3.2 Test Procedures

The tests were conducted as follows.

- **Installation of the transducers:** The normal-stress and shear-stress transducers were positioned flush with the surface of the flume base. The pore-pressure transducers (P1, P2, P3) were installed with end B (for P3 in Figure 3.3) being 1 cm lower than end A (for P3). End B was ensured to be de-aired.
- **Preparation and placement of sample:** To obtain loose samples with different void ratios, de-aired water was first added to the oven-dried samples to make the initial water content rise up to 5 percent, and then the sand was stirred evenly. After that, the sample was packed into the flume. To make the sample uniform, while packing, the sample was placed in a series of layers of 2 cm thickness parallel to the flume base, and then each layer was tamped. Finally, the superfluous parts of placed

sample were removed and the shape was made to be as shown in **Figure 3.3**. Initial dry density was determined from the oven-dried weight of the used mass and the volume of the sample.

- **Sprinkling water and recording:** When the sprinkling began, the data-logging system and video camera started to record. To successfully obtain the rapid change of pore pressure during quick failure, each of the instruments was logged at 0.05-second intervals.

3.4 DOUBLE CYLINDER APPARATUS AND TEST PROCEDURES

3.4.1 Double Cylinder Apparatus

The employed double cylinder rotating apparatus (designed by Sassa, 1988) is illustrated in **Figure 3.4**. It is composed of a rotating system, a double cylinder and a data recording system. To observe the variation of pore pressure along with moving velocity, the rotating system is made changeable in rotating velocity within a large range with help of a velocity control motor and a gearbox. The double cylinder, made from aluminum alloy with high hardness, is 14 cm in inside diameter, 30 cm in outside diameter, and 28 cm in depth. To observe the pore water pressure within the moving mass, pore pressure transducer is installed by drawing a vinyl hose from the bottom of cylinder, and to prevent the sample from sinking into the hose, porous stones are placed on the bottom, as shown in **Figure 3.4**. During tests, the mixture of sample and water inside the cylinder is rotated by four mixing rods that are connecting to the rotating axis, and the rotating velocity is measured with help of a potential meter. All the data from pore pressure transducer and potential meter are recorded by a personal computer automatically. Considering that in practice situation, the debris height (h_d) and the water height (h_w) are almost same in the head of debris flows (Sassa 1988a), all the tests

presented here were performed under the condition of $h_d = h_w$.

3.4.2 Test Procedures

All the tests were performed following the procedures as follows:

- To make sure that pore pressure be measured correctly, de-aired water is poured into the cylinder until the water level is flush with the upper surface of porous stone, so that the space below the porous stone is full of de-aired water without any air left.
- Weigh the oven-dried sample and setting it into the cylinder until the sample height reaches 15 cm;
- Sprinkle de-aired water from the upper opening mouth of cylinder until the water level reaches the same height as the sample. And then keep the water the same height as the sample for more than 12 hours without any disturbance to make the sample with high saturation degree.
- Rotate the mixing rods and then record the data of pore pressure and potential meter through computer. To observe the variation of pore pressure along with rotating velocity, the velocity is increased gradually by steps; and at each step, the rotating is kept 10 minutes and thereafter the data are recorded.
- After increasing the rotating velocity to a certain value at which the pore pressure does not change further more, decrease the rotating velocity gradually by steps to zero. At each step of deceleration, the rotating duration is kept 10 minutes also before recording the data.

Chapter 4

THE FLUIDIZATION BEHAVIOR OF THE SHEAR ZONE BASED ON RING SHEAR TESTS

4.1 INTRODUCTION

The undrained shear behaviour of sand is a knotty problem to civil engineers in dealing with a situation where soil liquefaction may occur. It is closely related to the determining of stress conditions required to trigger liquefaction, and the analyzing of the consequences of liquefied mass in terms of potential deformation. As aforementioned, based on the tremendous results of mostly triaxial tests, a very appealing concept of ultimate steady state was proposed and widely used in the procedure of analyzing liquefaction susceptibility of a soil in anti-liquefaction design (Castro 1969; Vaid and Chern 1983; Poulos et al. 1985; Alarcon-Guzman et al. 1988; Kramer and Seed 1988). And it was well accepted that saturated soil with void ratio and effective stress located below the steady state line in the “*e-logp*” diagram is impossible to suffer liquefaction failure. So it is generally believed, erroneously, that medium and dense sands have no susceptibility to suffer from liquefaction failure.

Nevertheless, recent undrained ring shear tests showed some inconsistent tendency, liquefaction being able to be triggered even in very dense sand due to grain crushing

accompanying increasing shear displacement. In the studies of earthquake-triggered-landslides based on ring shear tests, a concept of sliding surface liquefaction was proposed by Sassa to interpret the high mobility of failed landslide mass. As mentioned in Chapter 2, sliding surface liquefaction can take place even in medium or dense soil structure, and it is a localized liquefaction limited in the shear zone both in laboratory test and on the field.

Recently, Sassa and colleagues had carried out tremendous ring shear tests on different samples under different loading conditions (static load and cyclic load) to study the mechanism of sliding surface liquefaction, with emphasis on the relationship between grain crushing susceptibility and pore pressure generation, etc. (Sassa 1996; Sassa *et al.* 1997a, b; Vankov and Sassa 1998; Wang 1998). However, most of these studies were concentrated on the sliding surface liquefaction behavior, i.e., focusing on the undrained behavior of dense and medium dense specimens that exhibit dilative behavior. In this sense, the loose specimen was less studied in ring shear tests. Further more, as has been pointed out, in many cases of liquefaction-induced slope failure, the liquefaction was just limited in the sliding zone (Casagrande 1971; Castro 1992; Sassa *et al.* 1999; Seed 1968); and some laboratory researches have found that shear bonding could even be formed in very loose sand when subjected to shearing. Nevertheless, compared with the huge number of undrained triaxial tests, the undrained shear behavior of sand in the shear zone is still poorly understood and needs further scrutiny.

On the other hand, investigations into the shear behaviour of granular soils have generally concentrated on clean sands, which contains only relatively small quantities of silt and no clay. But as reported, natural sands often contain significant proportions of both silt and clay (Ishihara, 1985), and silt and silt-clay mixture are more prone to suffer from liquefaction failure with large resulting run-out distance, on the basis of many field observations (Bishop 1973; Eckersley 1990; Georgiannou *et al.* 1990; Ishihara 1990; Keith Turner & Schuster 1996). However, the undrained shear behaviour of silt and

silt-clay mixtures is not very clear. For evaluating the liquefaction potential of this kind of soil, there is no guideline available based on their density, void ratio, plasticity index, standard penetration values, or any other simple soil property. And even more, there is confusion on the influence of clay content, plasticity index, and void ratio, as pointed out by Guo & Prakash (1999). For example, by performing series tests on loose samples prepared with varying percentages of both plastic and nonplastic fines ($<74 \mu\text{m}$) and nonplastic fine sand ($>74 \mu\text{m}$), Pitman *et al* found that undrained brittleness decreased as the fines content, for both plastic and nonplastic type, increased; at a fines content of 40% the stress path indicated only strain hardening towards steady state, i.e., no brittleness. Another research carried out by Ovando-Shelley and Perez (1997) had pointed out that within limited range of clay content, the presence of clay increases the potential for generating excess pore pressure during undrained loading, and also reduces strength and stiffness. From these researches, it could be concluded that the undrained shear behavior of silt and silt-clay mixtures is not very clear and needs further extensive scrutiny.

Therefore, in this research, using a newly made ring shear apparatus (a detailed introduction of this apparatus, its operation, and test procedures are presented in **Chapter 3**), series tests were conducted on sand with different grain sizes and fine-particle (loess) contents (characteristics of these samples are listed in **Chapter 3** in detail). By performing tests at large range of relative densities and at different initial normal stresses, the different undrained shear behaviors are examined. Basing on the tests results, the mechanism of fluidization in the shear zone is analyzed.

4.2 EXPERIMENTAL RESULTS

Since it is impossible to present the results of all the tests that were carried out, here some typical results were selected to present the undrained shear behavior in different test conditions, with emphasis on examining the effects of initial relative density, initial

stress state, grain size, and fine-particles on the undrained shear behavior. The test condition and results for those selected tests are listed in **Table 4.1**.

4.2.1 Effects of Initial Relative Density on The Undrained Shear Behaviors

It has been pointed out that the initial relative density plays an important role on the undrained shear behavior (Castro 1969, Ishihara 1993). To make a good understanding of the undrained shear behavior of sand in ring shear tests, tests results were divided into two series according to their effective stress paths, to interpret their typical characteristics. One series is the tests on loose sand showing a typical effective stress path of mass liquefaction, with quick strain softening process that resulted in collapse failure; the other series is the tests on medium to dense sand showing the effective stress path of sliding surface liquefaction, with a process from strain softening to strain rehardening, and finally followed by liquefaction caused by grain crushing. Here, test results were presented to show their unique characteristics.

4.2.1.1 Ring shear tests on loose sand

The results of one test on loose sand S8 showing mass liquefaction behaviour during undrained shearing are illustrated in **Figure 4.1**. The sample for this test was made by means of moist placement and consolidated under the normal stress of 196 kPa and shear stress of 0. After consolidation, the relative density reached 63.3% (1.15 in void ratio).

Figure 4.1a shows the variation of shear resistance and pore pressure in relation to shear displacement. To make a clear view on the generation of pore pressure accompanying the shear displacement in the initial period, a logarithmic abscissa of shear displacement within the range of 10 cm was taken, and thereafter linear abscissa was used to show that the test had been sheared to steady state (the point of SSP in **Figure 4.1a**, for simplification, the steady state point will be termed as SSP in the

followings), where the shear resistance did not reduce further more. As shown in this figure, immediately after the undrained shear stress was applied, shear displacement took place. Accompanying the increasing shear displacement, pore pressure built up quickly within limited shear displacement range (about 1 cm), and shear resistance decreased remarkably. This period is usually known as the collapse period, mainly due to the failure of metastable structure. After 3-cm shearing, accompanying the further increase of shear displacement, pore pressure built up gradually and then shear resistance decreased slowly as the subsequence. This process might be due to the grain crushing accompanying the shearing.

Figure 4.1b shows the effective stress path and failure line. The failure line was measured after the undrained shear test was stopped by means of unloading the normal stress at a very small rate while the low parts of ring shear apparatus was kept rotating at a constant speed under drained condition. From this figure, it could be seen that after undrained shear stress was added from 0.0, with increasing shear stress, stress path extended towards but did not reach the failure line until the final point, i.e., the steady state. This effective stress path showed the same changing tendency as that in undrained triaxial tests on loose sand. Therefore, it was treated as mass liquefaction in ring shear tests.

Mass liquefaction appeared only in loose sand. Because all the tests were carried out under normally consolidated state, there were just limited tests showing mass liquefaction, while most of them showed another kind of fluidized failure of sliding surface liquefaction.

4.2.1.2 Ring shear tests on medium to dense sand

Figure 4.2 shows the results of a test on dense sand of S8, in which appeared typical sliding surface liquefaction phenomenon. This sample was made by means of dry deposition with heavy tamping. After saturated and normally consolidated, the sample

was sheared in undrained condition to a large displacement, 210 mm. To shorten the rotating time after failure, in this test, torque control method with Medium gear (32.3 cm/sec) was selected. Figure 4.2a illustrates the variation of pore pressure and shear resistance in relation to shear displacement; Figure 4.2b shows the corresponding effective stress path. As shown in Figure 4.2a, in the initial period after undrained shear stress was applied, with increasing shear displacement, pore pressure built up gradually. However, after point "PT", pore pressure decreased due to the dilatancy of dense sand. After the peak shear strength was reached (Point F in Figures 4.2a, b), sample failed, and thereafter, pore pressure built up gradually with shear displacement, finally reached 145 kPa approximately. The shear resistance decreased slowly consequently, and finally fell to approximately 34 kPa. The excess pore pressure ratio, which is determined as the ratio of excess pore pressure and initial effective normal stress, was approximately 0.74. As shown in Figure 4.2b, upon increase of shear stress, the effective stress path extended left-upward due to the pore pressure generation. After point "PT", the path went right-upward accompanying further shearing, showed a shape of "elbow" with a turn point. After failure point "F", the path fell downward along the failure line until a small shear stress. This is a typical stress path of sliding surface liquefaction.

According to Wang (1998), the pore pressure generation process along with the shear displacement could be divided into three stages as shown in Figure 4.2a; Stage 1: from the beginning to point "PT" (where the phase transformation was started, according to Ishihara, 1993), defined as the initial negative dilatancy area, it is mainly caused by the orientation of sand grains and the failure of metastable soil structure accompanying the increasing shear stress; Stage 2: from point "PT" to point "M" (where the pore pressure is the minimum), defined as initial positive dilatancy. With further increasing shear stress, sand grains adjust their positions, and/or move to each other. This would affect the adjacent particles significantly and lead to potential volume dilatancy, and then result in the reduction of generated pore pressure. Stage 3: from point "M" to final

point "E" (means end of the shearing), defined as negative dilatancy due to grain crushing, which results in the potential volume shrinkage. Absolutely, the pore pressure generation in each stage depends on the initial state (including the initial relative density, normal stress, shear stress, shear history, and even the ageing of sample, etc.), and the characteristics of samples (including the grain size, fine-particle content, possibility of grain crushing, etc.).

The undrained shear behaviour in triaxial apparatus as that before the point "F" in **Figure 4.2b** was described as limited liquefaction (Castro, 1969). Due to the limitation of triaxial apparatus in shear displacement, the behaviour after "F" was not obtained and not made clear until undrained ring shear apparatus was built and improved by Sassa and colleagues. Obviously, the prerequisite for this kind of liquefaction is that enough shear displacement could be offered for the effective happening of grain crushing.

In the liquefaction potential analysis based on triaxial test results, it has been pointed out that, for soil at a certain stress state, when the relative densities greater than those corresponding to the steady state line (obtained from undrained triaxial tests), the soil will exhibit dilative behaviour, and there will be no potential for liquefaction. However, the test results presented here shows that, provided that shear stress is great enough to initiate the failure of soil, liquefaction could be triggered, no matter the soil are in dense or loose state.

4.2.2 Effects of Initial Stress State

Fluidization landslides could be induced in different slopes, where the slope angle and soil depth may be different, i.e., the failure could be initiated at different initial stress state, and then the resulting failure could be different. To examine the effects of initial stress state on the fluidization landslides, in this test series, two sets of tests were conducted on S8 under different initial normal stresses and shear stresses respectively, and then the undrained shear behavior were examined.

4.2.2.1 Effects of initial normal stress

At first, a set of tests was conducted on samples consolidated to different normal stresses to study the influence of initial normal stress on the undrained shear behavior. Theoretically all the tests should be performed under the same relative density, but due to the difficulties in making samples and the effect of the applied initial stresses, there were still little differences between their initial relative densities among the tests presented here. Considering that the differences were very small (usually smaller than 0.05%), the influences caused by those differences in relative densities were neglected during analyzing.

Effects of initial normal stress on the undrained shear behaviour could be interpreted by **Figure 4.3**, the effective stress paths for 4 tests on S8. The samples for these four tests were all made by means of moist placement. They were normally consolidated at initial normal stresses of approximate 147.0, 196.0, 245.0, and 294.0 kPa, respectively (corresponding to 1.5, 2.0, 2.5 and 3.0 kgf/cm², respectively), and then were all sheared to steady state by increasing the shear stresses from 0.0 at a loading rate of 0.098 kPa/sec (0.001 kgf/cm²) under undrained condition. As exhibited in **Figure 4.3**, with increasing initial normal stress, the peak strength becomes greater (peak shear strengths were 41.2, 54.1, 61.2, and 70.6 kPa, for the tests with normal stress being 147.0, 196.0, 245.0, and 294.0 kPa, respectively), showing a tendency that static liquefaction resistance increases with increasing initial normal stress. Nevertheless, the final point of each effective stress path tending to the same point shows that these four tests have the same steady state strength (approximate 15.0 kPa), irrespective of initial normal stresses. In this aspect, ring shear tests results showed a good consistency with those obtained from undrained triaxial tests, hollow-cylinder torsional shear tests, etc.

4.2.2.2 Effects of Initial Shear Stress

Four test results were plotted in **Figure 4.4** to interpret the effects of initial shear stress

on the undrained shear behaviour of sand. The initial shear stresses for these four tests were 0.0, 34.5, 72.0, and 108.5 kPa, respectively, while the normal stresses were kept the same, 196.0 kPa. These four samples were all made by means of dry deposition without tamping, and were all normally consolidated. It is worth to note here that as stated above, in this series tests, the void ratio (relative density) should be made the same, but due to the difficulties in making samples and the possible effects of different initial consolidation stress state, although efforts were made by performing numbers of tests and then selecting those results of tests with the void ratios being approximately the same, there are still little differences between the tests presented here in their initial relative densities. Considering the differences being very small, their effects are ignored in the following discussion.

Figure 4.4 shows the results of tests on different initial shear stresses. Figure 4.4a presents the effective stress paths for these tests; and Figure 4.4b is the variation of shear resistance in relation to shear displacement. As shown in Figure 4.4a, for each test, with increasing shear stress, the effective stress path tended leftward and finally reached the failure line, thereafter fell down along the failure line towards zero point. It is worth to pay attention to the fact that with increasing initial shear stress, the effective stress path reached to the failure line more quickly, and thereafter followed the failure line dropping towards zero point, as illustrated by the effective stress path of test at initial shear stress of 108.5 kPa, which showed a typical sliding surface liquefaction behaviour. From Figure 4.4b, it could be seen that with increasing initial shear stress, the reduction rate of shear resistance against shear displacement becomes greater. Meanwhile, Figures 4.4a, b show clearly that with increasing initial shear stress, the peak shear strength become greater.

Although the tests on sand with different initial shear stresses showed different peak shear strength, it can be seen easily (Figures 4.4a, b) that the final liquefaction resistance were approximately the same. The little differences between their values may

be due to the little differences between their initial relative densities. As described above, denser sand will have greater steady state strength. Therefore, it could be concluded that initial shear stress has no influence on the steady state strength.

4.2.3 Effects of Grain Size

To examine the effects of grain size on the pore pressure generation, and then on the undrained shear behavior, a series of tests was conducted on S7 and S8 at large range of initial relative densities. Because S7 and S8 are made from the same material (silica sandstone) through grinding method, it could be inferred that the differences between their undrained shear behaviors, if exist, are resulted from the different grain sizes. Considering that there are two obviously different kinds of undrained shear behaviors in ring shear tests as described above, the effects of grain size are examined both in loose state and in medium to dense state, correspondingly. During comparison, relative density (D_r) was used to present their density.

4.2.3.1 In loose state

The effects of grain size on the undrained shear behavior in loose state could be illustrated by **Figure 4.5**, where the results of one test on loose S8 (63.3% in relative density) and two tests on S7 with different initial relative densities (47.2% and 56.6% respectively) are presented in the form of variation of shear resistance in relation to shear displacement (**Figure 4.5a**), pore pressure generation against shear displacement (**Figure 4.5b**), and effective stress paths (**Figure 4.5c**). It should be noted that theoretically, the initial relative densities for each sample should be made the same in this kind of comparison, but due to their different characteristics, although the same methods (by means of moist placement with the same tamping) were used in making the loose sample, after normally consolidated in the same stress state (normal stress being 196 kPa and shear stress being 0), the samples were still quite different in the initial relative densities. Therefore, to illustrate the influence of grain size, a complementary

test was performed on S7 that was made by means of dry deposition without tamping with relative density being 56.2% after consolidation. Although the relative densities of S7 and S8 were not the same yet, the effects of grain size on the undrained shear behavior could be seen evidently.

From **Figure 4.5c**, it could be seen that in the tests on loose S7 (47.2% in relative density) and S8 (63.3% in relative density), typical effective stress path of mass liquefaction appeared in both of them. Meanwhile, it could be found that both the peak shear strength and steady state shear strength for S8 were greater than those for S7 (as shown in **Figures 4.5a, c**). This difference could be interpreted by the different relative densities, S8 was 16.1% greater than S7 in relative density. Usually, this order of increase in relative density could result in great change in the undrained shear behavior, just as presented by the results of test on S7 of 57.9% in relative density. As shown in **Figures 4.5a, c**, there just showed a typical sliding surface liquefaction behavior without any (at least obvious) collapse behavior. Therefore, it could be inferred that, if make the relative density of S7 being 63.3%, the sand would behave sliding surface liquefaction with stronger rehardening process after the point of phase transformation (point "PT" in **Figure 4.5b**).

4.2.3.2 In dense state

Figure 4.6 presents the tests results of S7 and S8, illustrating the undrained shear behaviour of dense sands. The shear resistance-shear displacement curves (**Figure 4.6a**) and excess pore pressure-shear displacement curves (**Figure 4.6b**) are typical and obtained from a series of tests, their corresponding effective stress paths are shown in **Figure 4.6c**. Theoretically, their relative densities should be made the same during comparison, but due to the difficulties in preparing the samples, the relative densities of the tests presented here are 88.3% for S7, and 95.2% for S8. Nevertheless, the influence of grain size on the undrained shear behaviour could be seen evidently.

From **Figure 4.6a**, it could be seen that before the peak shear strength was mobilized, the shear displacement at a certain shear stress is greater for S8, showed higher deformation potential than S7. And then the corresponding pore pressure builds up rapidly for S8. But after failure, S7 had a quicker increase in pore pressure accompanying the increasing shear displacement in the final period, as reflected evidently by the change in curvature of the pore pressure versus shear displacement plotted in **Figure 4.6b**. And then the shear resistance decreases rapidly in the final period for S7 correspondingly. Usually, for the same sand, when relative density becomes greater, the generation of pore pressure along with shear displacement would become slower before the peak shear strength, and rapider after failure. Therefore, it could be concluded that the results illustrated in **Figure 4.6** were resulted from the influence of grain size. The difference could be interpreted by the main controlling factors in different shearing stages. For S7, its grain sizes are coarser; this makes the sand have less contacting points with greater average contacting forces acting on each of them. Therefore, it would be difficult for sand grains to orientate, and for the failure of metastable structure to happen in **Stage 1**. In **Stage 2**, the adjusting of position and motion of grains would result in higher dilatancy potential for coarser sand S7. During **Stage 3**, grain crushing happened in these coarser sands would result in higher potential of volume shrinkage, and then would result in quicker generation of pore pressure.

When we focus on their effective stress paths, **Figure 4.6c**, we can find easily that the locations of phase transformation, peak shear strength and steady state are differing for S7 and S8. The corresponding effective normal stresses for S7 at phase transformation point, peak shear stress and steady state are approximately 95, 266, and 67 kPa, respectively; while those for S8 are 79, 211, and 39 kPa, respectively, showing to be easier to suffer from liquefaction than S7.

4.2.4 Effects of Fine-Particle (Loess) Content

As mentioned in the introduction of this chapter, although there are some inconsistencies between the research results of different researches, it was made clear that fine-particle (including its characteristics and its content) could affect the undrained shear behavior greatly. Therefore, in this test program, by changing the initial void ratio, series tests were conducted on each sample of M10, M20, and M30. In each test series, when the initial relative density was different, the undrained shear behavior was differing, varying from mass liquefaction to sliding surface liquefaction. Here the effects of fine-particle (loess) content on the undrained shear behavior will be illustrated both from the phenomena of tests on loose samples and those of the tests on medium to dense samples. Because these samples with different loess contents were treated as different samples, here relative density was used when the comparison was made in this section, similar to the series tests described above.

4.2.4.1 In loose state

Because of the difficulties in making loose samples, the tests presented here to illustrate the effects of fine-particle content on the undrained shear behavior were different in relative density. Nevertheless, the effects could be seen clearly through the tests results. Here the selected three tests on M10, M20, and M30 were 52.6%, 63.3%, and 67.5% in relative densities, respectively (1.10, 1.02, and 1.00 in void ratios, correspondingly). The tests results are shown in Figure 4.7, where, Figure 4.7a presents the variation of shear stress in relation to shear displacement, Figure 4.7b plots the pore pressure against shear displacement, and Figure 4.7c draws the effective stress paths. As illustrated in Figure 4.7c, the tests on M30 and M20 showed quick collapse failure after the peak shear strengths were mobilized, while M10 behaved more like a sliding surface liquefaction failure: after the peak shear strength was mobilized, the shear resistance fell downward along the failure line with increasing shear displacement. Meanwhile, it could be found that when the fine-particle (loess) content became greater, the

corresponding peak shear strength and steady state shear strength became smaller. The test on M30 showed a very small peak shear strength and steady state shear strength (almost tended to 0), showed highest liquefaction potential among these three tests, although the relative density was the greatest.

4.2.4.2 In dense state

Figure 4.8 presents the tests results of dense M10, M20, and M30 with initial relative densities being 70.4%, 79.4%, and 80.5%, respectively (0.96, 0.89, and 0.89 in initial void ratio, respectively). Figure 4.8a, b show the variation of shear resistance and pore pressure in relation to shear displacement respectively, and Figure 4.8c illustrates the undrained shear behavior in the form of effective stress paths. As shown evidently, with increasing fine-particle content, the undrained shear behavior in the form of effective stress path changed remarkably. The test on dense M10 and M20 showed strong strain rehardening processes after the phase transformation point, during which shear strengths increased greatly due to suction of dense samples, and after failure, shear strengths reduced accompanying the generation of pore pressures (as presented in Figures 4.8a, c) due to grain crushing. With increasing fine-particle (loess) content, this strain rehardening process becomes weaker, showing a reduction tendency in peak shear strength. For the test on dense M30, there was almost no rehardening process due to dilatancy. This tendency could be seen evidently from Figure 4.8b, where the pore pressure generation along with shear displacement showed a continuous increase throughout the whole shearing process without any temporary reduction. Meanwhile, the steady state shear strength becomes smaller evidently with increasing fine-particle (loess) content. Therefore, It could be concluded that, with increasing fine-particle (loess) content (within the tested range of loess content, 30%), both the peak shear strength and steady state shear strength become smaller, i.e., become easier to suffer from liquefaction failure, while their initial relative densities are the same.

4.3 MECHANISM OF FLUIDIZATION IN THE SHEAR ZONE

There are many investigations on the case studies showing that liquefaction was initiated within the sliding zone, and this zone might be a newly developed one due to shear failure, or the existed sand seam (or sand lenses) sandwiched in the soil layers (Castro et al. 1992; Seed 1968). It was widely known that the possibility that the shear zone might liquefy is determined by the initial condition of the sand, by the magnitude of the stresses induced by earthquake or some other triggers, by the initial stresses in the sand before the loading, and by the possibilities for dissipation of pore pressure in the shear zone as they build up during the loading. Although these understandings are very appealing and widely accepted, they were based on the experimental results of mostly triaxial tests. As has been pointed out, soil failure is often accompanied by the occurrence of localized deformation in thin zones of intense shearing. Therefore, using the global stress-strain measurements in triaxial apparatus would not be representative of the localized shear behaviour while localization formed within the specimen (Finno et al. 1996). Recently, there were some researches had been carried out to study the centralized liquefaction failure by means of shaking table (for example, Kokusho 1999), geo-centrifuge (Zeng and Arulanandan 1994), plane strain apparatus (Finno et al. 1996, 1997), etc.. However, due to the limitation of these apparatus in shear displacement, the grain crushing could not be complete, i.e., the ultimate steady state could not be reached. In this aspect, ring shear apparatus offered an available method.

4.3.1 Formation of Localized Fluidization in the Shear Zone

As mentioned above, there are two kinds of different response in the undrained shear behaviors: mass liquefaction in loose state and sliding surface liquefaction in medium to dense state. To observe the shear behavior of sands in ring shear box, the shear deformation within the shear zone was observed after the two tests introduced in **Figures 4.1** and **4.2** were finished. Meanwhile, to observe the deformation of the sand within the whole ring shear box, two complementary tests were conducted on S8, while

keeping their relative densities being the same as those introduced in **Figures 4.1 and 4.2**. In each of these complementary tests, two vertical 1-cm wide slices made from Toyoura standard sands, whose color differs obviously from that of S8, were made inside the samples. The samples were saturated and normally consolidated following the methods used in their host tests. After sheared to 3 cm in undrained condition, the tests were stopped. Thereafter, the upper parts of ring shear apparatus were removed and the deformation of the inserted slices were observed.

The undrained shear results of the complementary test on loose S8 (having the same relative density as that of the host test shown in **Figure 4.1**) are presented in **Figure 4.9**. To make a convenient comparison, results of the host test are presented also. As shown, **Figure 4.9a** shows the variation of pore pressure and shear resistance in relation to shear displacement for the host test; and **Figure 4.9b** for complementary test, where logarithmic abscissa of shear displacement was taken for making a clear view on the generation of pore pressure accompanying the shear displacement in the initial period. **Figure 4.9c** shows the effective stress paths and failure line. As shown in these figures, within the shear displacement range of 3 cm, the complementary test and the host test behaved almost the same. Meanwhile, the pore pressure ratio reached approximately 0.75, indicating that liquefaction has been resulted in at the place of shear displacement being 3 cm.

Figure 4.10 presents the shear deformation of one slice inside the shear box for the complementary test. The difference in color assisted in the identification of shear deformation. As shown in this photo, the upper part of the slice inclined slightly leftward to the shear direction due to the shear deformation within the upper part of sample. Nevertheless, there is no obvious disturbance within the slice, but a shear zone (approximately 0.5-cm thick) formed between the upper and low parts. Therefore, it could be concluded that the liquefaction is just localized in the shear zone. This shows a consistency with the result of test on sand by plane shear apparatus, with which, it is

observed that shear banding could happen even in very loose sand (Finno *et al.* 1997).

The results of the complementary test for dense S8 shown in **Figure 4.2** are presented in **Figure 4.11**, in the form of variation of shear resistance and pore pressure in relation to shear displacement (**Figures 4.11a, b**), and in the form of effective stress path (**Figure 4.11c**). To examine the undrained shear behavior of the complementary test, the results of the host test are presented also in **Figure 4.11a** and **Figure 4.11c**. As shown in **Figure 4.11c**, except of a little difference that could be seen in the place of phase transformation, they behaved almost the same. This little difference might be resulted from the effects of vertically inserted slices of Toyoura sand, because even though the initial relative densities were made approximately the same, the characteristics of Toyoura sand are differing from those of S8. Anyway, this little difference could be regarded as having no influence on the observation of shear deformation.

Figure 4.12 illustrates the shear deformation of one slice. As shown, the slice stood nearly vertically even after sheared to 3 cm. There was a very thin zone (even can not see the zone but a line in **Figure 4.12**) formed between the upper and low parts, showing a highly centralized shearing along the shear zone.

4.3.2 Grain Crushing Within the Fluidized Shear Zone

As stated by Sassa (1996), grain crushing plays the most important role in sliding surface liquefaction. Based on the tests results, Wang (1998) had performed a analysis on the relationship between grain crushing possibility of sand in dry state and the pore pressure generation in saturated condition when subjected to undrained shearing. However, the grain crushing in the undrained condition was less examined. Meanwhile, in the definition of steady state deformation proposed by Poulos, it has been pointed out that steady state deformation could be reached only after the grain crushing, if existing, have finished. Therefore, the grain crushing was examined in the localized liquefaction phenomena of undrained ring shear tests.

First, the grain crushing analysis was performed on the test showing mass liquefaction (shown in Figure 4.1). After the test was finished, pore water was drained out from the shear box, by flowing Carbon dioxide from the upper drainage hose and draining water from the lower drainage valve. By doing this, the sample could be kept relatively undisturbed, while moving the upper mechanical parts of the shear box away. Thereafter, samples were taken out from the shear zone. It should be noted that an annular shear zone showing allspice-shaped cross section was formed, which was differing from the upper and lower part in color evidently with extinguished interface between its upper and lower boundary, due to the grain crushing within the shear zone (As shown in Figure 4.13). The grain size distributions of the original sample and that from the shear zone are illustrated in Figure 4.14. Because the shear was carried out under undrained condition, and at the same time silica sand no. 8 is kind of fine sand with hard particles, the degree of grain crushing is not heavy. To make a clear view of the differences between each other, logarithmic ordinate was used in Figure 4.14. As shown, the grain size distribution curve for the sample from shear zone is locating above that for the original sample, showing that grain crushing was initiated in the shear zone.

From Figure 4.9, it could be seen clearly that after sheared to 3 cm, the sand showed a quick and great loss in shear strength, and thereafter, the shear strength decreased slowly with increasing shear displacement. From the grain crushing analysis presented in Figure 4.14, it could be considered that this slow reduction in shear strength was resulted from the grain crushing within the shear zone.

Following the same method, the grain crushing analysis was performed on the test of dense sample (presented in Figure 4.2). The results are presented in Figure 4.15, and it could be seen clearly that Figure 4.15 shows the same tendency as that in Figure 4.14: the sample from the shear zone is the finer than the original sample. It is needed to say that, after the test was finished and the upper parts of the shear box were moved, the shear zone was very clear, showing the same shape of cross section as, but thicker than,

that in **Figure 4.13** (as shown in **Figure 4.16**), due to more severe grain crushing.

From the cross section of the shear zone appeared in both the loose state and dense state, it could be inferred that the shear was localized in the shear zone, now matter the sand was in loose state or in dense state. Therefore, it could be concluded that liquefaction was limited in the shear zone in ring shear tests.

4.3.3 Collapse Behaviour of Loose Sand Within the Shear Zone

To analyze the undrained shear behavior of loose sand, the collapse behaviors in ring shear tests at different initial normal stresses were examined. As reflected by **Figure 4.3**, the point of peak shear strength at each effective stress path lies on the same line, which was referred to as “collapse line” by Sladen (1985). According to Sladen’s proposition, this line binding the points of peak shear strengths for the tests at different normal stresses passes through the steady state point, and is dependent on initial void ratio. Similar to this concept of collapse line, Vaid and Chern (1983) proposed a concept of “critical stress ratio line” (CSR), and they found that the points of peak shear strengths lie in the same line, and this line projects back through the origin and is independent on initial void ratio. This CSR line is called the flow liquefaction surface (FLS), presenting the onset of flow liquefaction. It could be seen that these two concepts of collapse line and critical stress ratio line share the same meaning: marking the onset of quick strain softening that would result in flow liquefaction. Nevertheless, they showed controversies evidently, although they were all based on triaxial compression tests results. Some commenced research works support Sladen’s collapse line (Ishihara 1993; Sasitharan et al. 1994). Meanwhile, “Critical stress ratio line” was supported also by some studies (Vaid *et al.* 1989; Alarcon-Guzman *et al.* 1988; Negusse *et al.* 1988; Konrad 1993). In this undrained ring shear tests, from the tendency of collapse line drawn in **Figure 4.3**, it could be seen evidently that collapse line projects back through origin, supporting Vaid’s critical stress ratio line (collapse line).

As aforementioned, the grain size could affect the undrained shear behavior. To examine the effect of grain size on the collapse behavior, here a series of tests was conducted on S7 at different initial normal stresses. The results of tests on loose S7 were presented in Figures 4.17a. From this figure, it could be found easily that collapse behaviour happened in each test: after the peak shear strength was mobilized, the sand failed rapidly accompanying the quick generation of pore pressure and reduction in shear resistance; connecting the peak strength points formed a collapse line and this collapse line projected back through the origin. A comparison of the inclination of collapse line shown in Figure 4.3 and that shown in Figure 4.17a could result in a finding that the collapse line for loose S8 in Figure 4.3 is steeper than that for S7 in Figure 4.17a. This could be interpreted by the different relative densities. As shown above, in these series tests, although the void ratios in series tests on S8 were approximately 1.15, while those in the series tests on S7 were approximately 0.98, seemed denser than S8, the relative densities for the series tests on S8 were approximately 63.3%, while those for the series tests on S7 were approximately 47.2%, evidently smaller than that of the tests on S8.

To compare the effects of grain size on collapse behavior, it is desirable to conduct the tests on S7 and S8 at the same relative densities. However, as proved by the results of a trial test on S7, when the initial relative density reached at 57.9%, the undrained shear behavior showed a typical sliding surface liquefaction phenomenon with a strong rehardening process (as shown in Figure 4.5), namely without any collapse behaviour that could result in the quick liquefaction failure. Hence, it could be inferred that when the relative density of S7 reaches 63.3%, at which S8 showed quick collapse failure, there would be no collapse failure behavior for S7. Nevertheless, a series of trial tests on S7 with collapse behavior in the undrained shear process showed that collapse behaviour is dependent on the grain size as well as on the relative density. The samples of this series tests were made by means of dry deposition without tamping and consolidated at different normal stresses with void ratios being approximately the same,

0.93 (56.6% in relative density). The tests results were presented in **Figure 4.17b** in the form of effective stress path. As shown, in each test, after the peak strength (before the re-hardening process) was mobilized, the sample failed, showing an evident collapse process during which excess pore pressure generated quickly and shear resistance reduced consequently. However, after a certain period of quick strain-softening, the sand re-hardened, and showed a limited increase (very small) in shear resistance before the failure; after failure, with increasing shear displacement, pore pressure built up and then shear resistance was reduced consequently, this led to the effective stress path dropped down along the failure line. It could be seen that the final point of each test tended to approximately the same value, and binding the peak strength (before the re-hardening process) of each test formed a direct line that projects back the origin, showing consistency with the tests results of those two series described above. Comparing this collapse line with that of S8 shown in **Figure 4.3** could lead to a finding that the collapse line for S7 at relative density of 56.6% is steeper than that for S8 at the relative density of 63.3%. Meanwhile, as shown, the inclination of the collapse line in **Figure 4.17a** is approximately 19.0 degrees, while that in **Figure 4.17b** is approximately 22.1 degrees. Although the difference in inclination is just two degrees, considering the difference between their void ratios is very small (just 0.05 in e value), it could be seen that the increase tendency of inclination of collapse line with initial void ratio is evident. Therefore, it could be concluded that the collapse behavior was affected not only by the grain size, but also by the initial relative density.

4.3.4 Brittleness Index for Sand at Different Stress States

From field observations, it is normally understood that slope failure behavior is controlled by the slope angle and soil thickness, namely well connected with the initial stress state. To predict the fluidized slope failure behaviour through the tests results, here the brittleness index for sand at different stress state were examined. Because the brittleness index is strongly dependent on the initial density (Bishop, 1969), to

minimized the effects of initial density, here the effects of stress state on the brittleness index will be examined basing on those tests presented in Section 4.2.2.

The effect of initial normal stress on the brittleness index could be seen evidently from an observation of Figure 4.3, where the undrained peak shear strength increases with increasing initial normal stress, while the steady state shear strengths for all the tests are approximately the same. Therefore, it could be concluded that the brittleness indexes are differing from each other ($I_B = 0.64, 0.72, 0.75,$ and 0.79 , for the test with normal stress being $147.0, 196.0, 245.0,$ and 294.0 kPa, respectively); the test on sand consolidated to greater normal stress has a greater brittleness index, just as shown in Figure 4.18a. As mentioned previously, a greater brittleness index indicates a greater reduction in shear strength that may be associated with larger and faster deformation after the initiation of liquefaction. Hence, it could be inferred that for a fluidized landslide in practice situation, the thicker the failed soil mass is, the faster and longer the soil mass would move.

The effect of initial shear stress on brittleness index could be drawn also from Figure 4.4, through which it could be seen that the peak shear strength becomes greater with increase of initial shear stress while the steady state shear strength is the same. Therefore, the brittleness index (I_B) becomes greater consequently. This tendency is illustrated evidently in Figure 4.18b, where the brittleness indexes are plotted against initial shear stresses. Therefore, it could be concluded that the fluidized landslide initiated at a steeper slope will suffer from faster and larger progressive motion.

4.3.5 Characterization of Fluidization Behavior of Sand with Different Grain Size and Fine-Particle (Loess) Contents

In dealing with the possible fluidization behavior of a soil mass in the field, the pore pressure generation process, peak shear strength and steady state strength may be the key parameters. Therefore, the different characterization of fluidization behavior of

sands due to the change in grain size and fine-particle (loess) content will be examined in these three aspects.

4.3.5.1 Pore pressure generation at different stages

As mentioned before, mass liquefaction only appeared in loose sand, while most of them showed sliding surface liquefaction, where a process of negative dilatancy-positive dilatancy-negative dilatancy appeared with the increasing shear displacement (described as Stage 1 to Stage 3 in Section 4.2.1.2), therefore, to examine the effects of grain size on the compressibility, dilatability and crushing characteristic of samples respectively, the effects of grain size on pore pressure generation during these different stages (for sliding surface liquefaction) were examined. In the present stage of this research, tests were conducted on S7, S8, M10, M20, and M30, respectively, namely on samples with grain size becoming finer. Because there was no rehardening process for the tests on M30, here the results of tests on S7 and S8 are used to illustrate the effects of grain size on the pore pressure generation.

The pore pressures generated in different stages (as introduced in Section 4.2.1.2) were examined separately for the tests on S7 and S8, and plotted in Figure 4.19 against relative density. Figure 4.19a reflects the generated pore pressure due to shear deformation before the phase transformation point, corresponding to stage 1. As showing, S8 has a greater pore pressure than S7 at this stage, while their relative densities are the same. This substantiates the explanation given in section 4.2.1.2, finer sand S8 having higher deformation potential than S7. Figure 4.19b presents the reduction of pore pressure due to dilatancy of dense sands, corresponding to Stage 2. It could be seen that the generated pore pressures were all negative during this period. From the fact that the reduction of pore pressure for S7 is greater than that for S8, while their relative densities being the same, it could be concluded that dense coarser sand has greater dilatancy potential when subjected to undrained shearing. But when we focus on

Figure 4.19c, we could find that the initiated pore pressure for S7 in Stage 3 is greater than that for S8, showing that coarser sand has higher volume shrinkage potential due to grain crushing during shearing.

4.3.5.2 Undrained peak shear strength

For the tests carried out under the same initial stress state, the peak shear strength could reflect whether it is difficult for a given sample to suffer fluidization failure or not. Therefore, emphasis was directed to the peak shear strength during the analysis of fluidization behaviors of sands with different grain size and fine-particle (loess) contents.

Because the peak shear strength is dependent on the initial shear stress, here the peak shear strengths are all those tests carried out under the same initial stress state (initial normal stress = 196 kPa, and initial shear stress = 0). The peak shear strengths versus relative density for S7 and S8 are plotted in Figure 4.20a. An observation of this figure could immediately lead to an understanding that S7 has a greater peak shear strength than S8, while their relative density are provided the same.

The peak shear strength for M10, M20, and M30 were plotted in Figure 4.20b against relative density. As reflected in this figure, peak shear strength increases with increasing relative density for each sample. From the changing trend of each sample, it could be seen that given the initial relative density being the same, the peak shear strength becomes smaller with increasing fine-particle (loess) content (within the tested range of loess content of 30%).

From the tests results presented above, it could be concluded that when the grain size becomes finer or with increasing fine-particle (loess) content (within tested loess content limitation of 30%), the sample becomes easier to suffer fluidization failure.

4.3.5.3 Steady state strength

Steady state strength plays an important role on the motion of fluidized soil mass. It is directly related to the final slope angle when the fluidized mass stopped. As an important component in analyzing the fluidization behavior of sands with different grain size and fine-particle (loess) contents, here the steady state strengths are examined.

Although the steady state strength is just a function of initial relative density, irrespective of initial stress state, the apparent friction angle (see Chapter 2) is dependent on the initial normal stress. To analyze the fluidization behavior of sample, here those strengths at steady state for all the samples are from all the tests conducted at different initial void ratios and the same initial normal stress (196 kPa).

Figure 4.21 show the steady state points for S7 and S8, plotted on a D_r versus $\log(\tau_s)$ and D_r versus $\log(\sigma_s')$ plane, where σ_s' and τ_s are the effective normal stress and shear strength at steady state in ring shear test, respectively. From the tendency, it could be seen that the steady state line of S8 is located above that of S7 both in Figure 4.21a and 4.21b. It shows that finer sand S8 has smaller effective normal stress, and then smaller shear strength consequently than S7, while their relative densities being the same.

The steady state strengths for M10, M20, and M30 were presented in Figure 4.22, where initial relative densities are plotted as ordinates, and shear strengths and effective normal stresses at steady state as abscissas in logarithm form (Figures 4.22a, b). As shown, with increasing fine-particle (loess) content, the steady state line shifts the position from that of the M10; when the relative density for each of them are the same, the shear strength at steady state becomes smaller with increasing fine-particle (loess) content, at least within the range of loess content being 30%.

According to the suggested criterion for judging fluidization behavior of soil in undrained ring shear tests, the apparent friction angle should be less than 10 degrees,

namely the undrained shear strength at steady state should be less than 34.6 kPa, given the initial normal stress being 196 kPa. Here we use τ_c to term this value of 34.6 kPa. The corresponding line is drawn in **Figure 4.21a** and **Figure 4.22a** in the form of dotted line, and then the area on the left of this line presents that fluidization is initiated, while the area on the right presents no fluidization. Therefore, the relative density (D_{rc}) corresponding to that at the intersection point of the steady state line and this dotted line for each sample is critical; when the initial relative density is smaller than this value, fluidization could be initiated, while greater, no fluidization. From **Figure 4.21a**, it could be seen that this value of D_{rc} for S8 is much greater than that for S7. Meanwhile, **Figure 4.21b** shows the same tendency: with increasing fine-particle (loess) content, this value of D_{rc} is becoming greater, and the when the fine-particle (loess) content increases to some extent (30% of loess content), fluidization could be initiated in almost all the tests, even in the most dense state.

4.3.6 Maintaining of Generated Pore Pressure in Shear Zone

In practice situation, there were many cases where liquefaction had been initiated but the liquefaction-induced movements were of only limited extent (McCulloch and Bonilla 1967; Seed 1968). Although there are many reasons why a slide caused by soil liquefaction may not result in large deformations, the maintaining of generated pore pressure may be the most important factor. Liquefaction can only persist as long as high pore pressures persist in a soil; if drainage can occur rapidly then liquefaction may persist for such a short period of time that large displacements are unable to develop. In practice, the liquefied soil mass could be regarded as in undrained conditions during the very short period of failure triggered by earthquake, rainfall or some other factors, but could not be treated as in undrained condition throughout the whole moving process. Therefore, the persisting of generated pore pressure will be an important factor affecting the run-out distance of a fluidized landslide in the field, just as stated by Seed (1968). Considering that in this ring shear test series and in many historic liquefaction failures,

liquefaction was limited in the shear/slide zone, it is highly desirable to have an insight into the maintaining of pore pressure in the shear zone. Therefore, a series ring shear tests was carried out to examine the dissipation of generated pore pressure in the shear zone. During tests, the saturated samples were shear in undrained condition to a large displacement where the liquefaction was ensured to have been initiated, and thereafter turned the shear box into drained condition to observe the dissipation of generated pore pressure and recovering of the shear strength.

Figure 4.23 presents the results of tests on S7, S8, M10, M20, and M30, where the shear resistances are plotted against the elapsed time. In all these tests, the moment when the shear box was turned into drained condition was treated as the zero point of elapsed time. Because the recorded value in pore pressure transducers just present the pore pressure outside the shear zone (as illustrated in Chapter 3), when the shear box turned into drained condition, the pore pressure within the shear zone could not be observed correctly. Nevertheless, the recovering of shear strengths could reflect the dissipation of generated pore pressure. As shown in Figure 4.23, when the shear box was turned into drained condition, the shear strengths of S7, S8, M10, M20 were recovering with the elapsed time, i.e., with the dissipation of generated pore pressure. However, an observation on the inclination of each curve (recovering rate of shear strength) could direct to the finding that the when the sample became fine and the fine-particle (loess) content became greater, this recovering rate of shear strength was becoming smaller, especially for the test on M30, there was almost no recovering tendency could be seen. Therefore, it could be inferred that once the liquefaction was initiated in the soil mass containing greater fine-particle, the pore pressure could be kept for a long time that would result in large deformation. This result showed a consistency with many laboratory researches and field cases (Seed 1968; Zeng and Arulanandan 1995).

4.4 SUMMARY

Several sets of undrained ring shear tests were conducted on S7, S8 and the mixtures of S8 with different loess content by weight to study the fluidization behavior of sand within the shear zone. By inserting slices of Toyoura sand with different color into the shear box during the undrained shear tests on S8, the formation of sand within the shear box was observed. By taking sample from the shear zone after the undrained shear tests, grain crushing behavior was examined also. Based on the tests results, the effects of initial relative density, initial stress state, and samples on the undrained shear behavior were examined by analyzing the undrained peak shear strengths and steady state shear strengths, and then the fluidization behavior was examined. By turning the shear box into drained condition after the sample was sheared to a high pore pressure under undrained condition, the dissipation of generated pore pressure from the shear zone for different samples was examined also.

Chapter 5

THE FLUIDIZATION BEHAVIOR OF LANDSLIDE MASS IN THE FLUME TESTS

5.1 INTRODUCTION

Rainfall-induced landslides pose significant hazards in many parts of the world especially in the mountainous areas in a sub-aqueous environment, because they occurred frequently and some of them were characterized by rapid movement and large run-out distance. It is generally recognized that rainfall-induced landslides are caused by increased pore pressures and seepage forces during period of intense rainfall (Anderson and Sitar 1995; Sitar et al. 1992). It is indicated that it is the increased pore pressure that decreases the effective stress in the soil, and then reduces the soil shear strength, and eventually results in the slope failure (Brand 1981, Brenner et al. 1985). Further study points out that slide along the sliding surface leads to the grain crushing, then leads to the sliding surface liquefaction, and finally results in rapid movement (Sassa 1996, Sassa 1998a, b).

As mentioned in **Chapter 2**, if the slope failure is a kind of fluidized landslide, there are two kinds of after-failure behaviour for the landslide mass correspondingly; one is flowslide, and the other is rapid slide. Flowslides triggered by dynamic effects, such as

earthquakes, or by static effects, such as rainfall (Eckersley, 1985; Sassa, 1998a, b), snowmelt, etc., had received much attention and had been studied extensively (Bishop 1967, 1973; Casagrande 1971; Ishihara et al. 1990; Marui 1996; Sassa 1984a, 1996, 1998a, 1998b; Seed 1966; Terzaghi 1956), and the majority of these studies have been concerned primarily with evaluation of liquefaction susceptibility and steady state strength of liquefied materials. It was found that the liquefaction resistance of a sand is influenced by a number of factors, including relative density, confining pressure, initial shear-stress conditions, as well as grain angularity, over-consolidation ratio, previous strain history, length of time under sustained pressure, grain structure or fabric, and loading rate (Castro 1969; Casagrande 1971; Castro & Poulos 1977; Hird and Hassona 1990). However, the understanding of all of these failures has relied almost entirely on laboratory testing of small specimens under idealized conditions. It is highly necessary to confirm these observations by measuring processes in real flowslides (Eckersley 1990; Hungr and Morgenstern 1984a). Along this line of thought, Eckersley (1990) triggered liquefaction and flowslides in coking-coal stockpiles by raising the water table, and showed that excess pore pressures were generated during, rather than before, movement. However, in this work, the sliding displacement was recorded only by video cameras; observations of deformation within the stockpiles were not carried out. By using a flume, Kubota (1997) performed a series of tests on silica sand and loess to study the mechanism of flowslides under conditions of rainfall. Kubota concluded that the generation of pore pressure was a result of sudden initiation of subsidence. Another laboratory flowslide study was conducted on loose saturated fine quartz sands in which the motion of liquefied sands and pore pressures during motion were analyzed (Spence & Guymer 1997). However, how the excess pore pressure generates, and how the liquefaction and slide motion are affected by grain size, void ratio, fine-particle content, and other basic factors, are still poorly understood. Therefore, in the present study, by changing the initial void ratio and samples, a series of laboratory experiments was performed in a flume under conditions of artificial rainfall. Meanwhile, to examine the

pore pressure maintaining mechanism of the fluidized landslide mass during motion, the double cylinder mixing tests were conducted also on different samples. Based on the results, the initiation and maintaining of pore pressure were examined, and then the resulting movement of failed landslide mass were analyzed. Finally, the initiation and motion of fluidized landslide in flume tests was scrutinized.

5.2 TEST CONDITIONS

Test conditions and some test data are summarized in Table 5.1. In this research, the flume angle was kept at 30 degrees, and the thickness of soil layer was 10 cm. Density was expressed by density index I_d . In all these tests the given rainfall intensity was 1.7 mm/min. The tests were carried out in three series, i.e.,

- Test series I : tests on S7;
- Test series II : tests on S8;
- Test series III : tests on M10, M20, and M30.

5.3 OBSERVED PHENOMENA AND DISCUSSION

Although the observed phenomena were differing from each other, they shared some similarities. In general, the entire process required 25 to 30 minutes for slope wetting, and a few seconds for failure (reviewed by video recordings).

5.3.1 Generation of Excess Pore Pressure

To study the effects of pore pressures on the motion of failed masses, pore pressures were monitored at three places. The pressure transducers installed at the places of x_2 and x_3 were planned to monitor the pore pressure during motion. However, pore pressures monitored at x_2 and x_3 were not correct (in many cases, they were not obtained), due to the effect of possible existing of air in the tube before the failed mass passed by, and meanwhile, due to the rapidly changing depth of flowing-over mass, as well as the pore-pressure dissipation during motion. Then, the pore pressure monitored at the

location of x_1 was used to analyze the behaviour of pore pressure generation in the source area. Here, the results of one test are used to interpret the generation of pore pressure.

Figure 5.1 shows the results of test S8_{1,3}, where **Figure 5.1a** illustrates the time series of pore pressure and sliding distance immediately before and after the failure. **Figure 5.1b** is the enlargement of **Figure 5.1a** for the very short period of failure. The precise monitoring of transient pore pressures in relation to slope movement demonstrated that excess pore pressures in the shear zone did not exist prior to the initiation of failure (**Figure 5.1b**). As shown, there was gradual increase of pore pressure, u_i , probably due to the rise of water surface in the sample before the failure. After failure, the pore pressure rose rapidly; this must have been due to the influence of excess pore-pressure generation due to shearing because rainfall intensity was kept constant. Thereafter, the pore pressure fell (**Figure 5.1a**), probably because the soil mass moved downward and the resulting decrease of mass height resulted in dissipation of pore pressure. It should be noted that the maximum value of pore pressure (u_m) measured was much greater than u_i . **Figure 5.1b** illustrates the concept that excess pore pressure was generated during shearing rather than before the failure of slope, as had earlier been pointed out in the research by Eckersley (1990).

5.3.2 Motion of Failed Landslide Mass

The resulting motion of landslide mass is differing for the tests on different samples at different initial densities. In the series tests on S7, although the test phenomena were differing from each other when the initial densities were different, just retrogressive sliding happened. However, in the series tests on S8 (Series II) and the mixtures of M10, M20, and M30 (Series III), rapid flowslides were initiated. Therefore, in the following, the interpretations of the test phenomena will mainly concentrate on the description of these two different phenomena: retrogressive sliding and flowsliding.

5.3.3.1 Retrogressive sliding

Among the tests on S7 in which retrogressive sliding were initiated (Series I), according to the video recordings, it was observed that the motion of failed mass was affected greatly by the initial density. The test phenomena were summarized in **Figure 5.2** (Type A and Type B). Although the more detailed failure process than **Figure 5.2** was differing for different tests conditions, to have a brief understanding on the whole failure process, the failure mode was divided into type A and type B, and the failure process was divided into four periods.

- (1) **Wetting:** After sprinkling, the water came down toward the base gradually, and wetting front was approximately parallel to the base. During this period, there appeared obvious normal displacement in type A, while there was no visible normal displacement in type B.
- (2) **Precursory failure:** After the wetting front reached the base, with the rising of saturation degree, retrogressive compound shallow sliding appeared at the toe part of slope. After sliding, the masses became very thin and then flowed downward.
- (3) **Major failure:** Following the retrogressive compound shallow sliding, major failure happened. The failed mass slid a certain of distance (ΔS , as shown in **Figure 5.2**), with the styrene foam ball in it, and then stopped. During this period, the sliding behaviors were quite different in type A and in type B. In Type A, during the motion of failed mass, several blocks were formed at about the same time. While Type B is characterized by slow retrogressive sliding. After one (usually big) block failed and slid downward, the next block was formed. This retrogressive process continued several times. The results show that the initial void ratio has great effect on the failure mode. In general, the extremely loose samples were susceptible to the failure of type A, while loose samples were susceptible to the failure of type B.
- (4) **Successive motion:** After the major slides, with continuing of sprinkling, the slid

masses became very shallow and flowed downward slowly. In this process, because the flowslide was too shallow that the foam ball could not be carried to move together, the moving displacement was not obtained.

5.3.3.2 Flowslides

As observed, the initiated flowslide phenomena varied with the samples and samples' initial density. Nevertheless, to make a distinguish between the flowslides and retrogressive slides, here the failure process of flowslides, initiated in test series II and III, were divided into 4 periods also, and summarized in Type C shown in Figure 5.2.

As shown in Figure 5.2, for the failure of Type C, each step has its own characters. (1) In the first period of wetting, the samples behaved the same as that described in Type A and Type B. And obvious normal displacement appeared just in the tests on extremely loose sample. (2) In the precursory failure period, the sample behaved differently from that of Type A and Type B. There happened obvious shear deformation within the whole layer. (3) During the major failure period, failed mass accelerated quickly, run out a certain distance and then stopped. According to the video recordings, it was found that the motion at the surface was faster than that at the flume bottom, i.e., there was relative motion within the failed mass along different thickness, showing the characteristics of flows. (4) As the successive motion, the once stopped failed mass began to move and flew downward slowly.

Compared with the observed retrogressive failures, flowslides usually have greater moving speed and larger moving distance. To examine the motion characteristics of flowslides, here test results of S8_{1.8} (the same in Figure 5.1) are used to interpret the motion process. The time series data of sliding distance and sliding velocity just before and after the failure of the test are shown in Figure 5.3. Because there was relative motion within the soil layer during flowing as mentioned above, the "velocity" used here refers to the velocity along the flume base because the sliding distance was

monitored by the linear-displacement transducer installed along the base. As shown, after failure the mass flowed and showed rapid movement for approximate 45 cm, and then it stopped. With continuing rainfall, the once-stopped soil mass then began to move at an almost constant slow speed.

Figure 5.4 shows the variation of velocity during sliding in relation to the sliding distance. As indicated, the moving process involved three stages as follows:

- (1) **Stage 1 (Accelerating process):** After failure, the sliding mass accelerated until reaching a certain velocity, which was the peak value during the entire sliding process.
- (2) **Stage 2 (Decelerating process):** After velocity reached its peak value, the sliding mass decelerated; with increased sliding distance, the velocity reduced to zero.
- (3) **Stage 3 (Steady slow sliding):** After a certain distance (ΔS) of movement, the mass began to accelerate again and finally shifted to a very slow motion at an almost constant value.

As shown in **Figure 5.4**, the sliding distance (ΔS) was initiated during major failure period. Meanwhile, as described above, for the retrogressive failure of both Type A and Type B, there was a certain of sliding distances (ΔS) happened in the major failure period for each test. Because the excess pore pressure for each test was obtained in the major failure period, to examine the relationship of generated excess pore pressure and initiated sliding distance, the corresponding resulted sliding distance in the major failure process was examined and summarized in **Table 5.1**. For simplification, the sliding distance of movement during the major failure period (ΔS) is termed the “rapid run-out distance” (ΔS) in the following sections, both for the retrogressive failures and flowslide failures.

The sliding velocity (in **Figure 5.4**) undoubtedly is affected by the generation of excess

pore pressure. At stage 1, excess pore pressure was generated which reduced the shear resistance, and then an unbalanced driving force was resulted in, which caused the acceleration of sliding. At stage 2, the pore pressure dissipated with an increase in sliding distance; the shear resistance became greater than the driving force, and then deceleration was resulted in. Finally, in stage 3, the driving force and shear resistance reached a balance, and the sliding velocity tended to the same value.

5.4 EFFECTS OF INITIAL VOID RATIO

The initial void ratio plays an important role in liquefaction. Saturated sands with considerably greater void ratio than those on the steady-state line were found to liquefy when subjected to undrained monotonic shear (Castro 1969). In undrained shear tests, the void ratio still remains at its prefailure value. Therefore, the undrained steady-state shear strength is a function of void ratio only (Ishihara 1993). However, as aforementioned, although most shear tests have been conducted under undrained loading, this is not in itself a prerequisite for liquefaction (Sassa 1985a; Sladen et al. 1985). To study the effect of void ratio on the generation of pore pressure and resulting motion of failed mass under the naturally drained unsaturated situation, a series of tests was conducted on S7 and S8 by changing the initial density.

5.4.1 On Excess Pore Pressure

Excess pore pressure was generated during quick failure of the slope, as shown in **Figure 5.1**. To analyze the relationship between excess pore pressure and failure motion, the excess pore pressure (Δu) of each test was estimated by regarding it approximately as the difference between u_m and u_i (**Figure 5.1**), and then, the relationship of Δu with initial density (expressed as initial density index I_d) was examined.

The test results show that the generated excess pore pressure for each test greatly depended on the initial density index. Excess pore pressures for the series tests on S7

and S8 versus density index are plotted in Figure 5.5. As presented, with increasing density index, the excess pore pressure increased until a certain value of I_d (I_d value at which excess pore pressure reached its peak value is denoted as I_{dm}), and thereafter, it decreased. Although many factors are involved in the build-up of excess pore pressure, in this situation the main reason is considered to be as follows. For the tests in which I_d is smaller than I_{dm} , the permeability is greater; thus, the dissipation will be quicker accordingly, and pore pressure buildup will be weaker. For the tests in which I_d is greater than I_{dm} , because of the smaller void ratio, the volume reduction during shearing will be small; thus, lower pore-water pressure generation will accompany the failure. Therefore, it is concluded that there is an optimal density index for excess pore-pressure generation.

5.4.2 On the Motion of Landslide Mass

5.4.2.1 On the failure mode of retrogressive sliding

In section 5.3.2, the failure processes of retrogressive sliding were classified into two types and each type was divided into four stages to give an illustration in detail. According to the test results, it was made clear that the failure mode was greatly affected by the initial void ratio. Usually, extremely loose sand ($I_d < 0$) was easy to suffer from the failure of type A, although there was an exception of S7_{1A} ($I_d = 0.01$), during which the failure of type A happened also; while the initial density indexes ranged from 0.17 to 0.5 ($0.17 \leq I_d < 0.5$), the samples were more prone to suffer from the failure of type B.

5.4.2.2 On the flowslide motion

In the series tests on S8, M10, M20, and M30, rapid flowslides were initiated. To investigate the characteristics of the initiated flowslides during motion, the relationship of sliding distance and sliding velocity for each test at different initial densities was

examined. Variation of sliding velocity in relation to sliding distance for the tests on S8 is shown in **Figure 5.6**. It could be seen that all the cases show the accelerating, decelerating, and steady slow-movement stages. During the rapid-movement stage (accelerating period and decelerating period), the peak values of velocity and rapid run-out distance (ΔS) differ for the samples with different initial density indexes. However, during the final steady slow-movement stage, there appeared no obvious difference in their sliding velocities.

Although there were some exceptions (S8_{II,9}, S8_{II,10}, as shown in **Table 5.1**) because of the difficulties with test-sample preparation, the peak value of velocity and rapid run-out distance (ΔS) of flowslide became generally greater with increase of the initial density index (**Figure 5.6a**). Also, there was a certain density index at which both of peak velocity and rapid run-out distance (ΔS) reached their maximum values. After that, with increase of initial density index, they tended to decrease (**Figure 5.6b**). This variation was in accord with the tendency of excess pore-pressure generation in relation to initial density index (**Figure 5.5**). As shown, the test with the greater excess pore-pressure generation had greater peak velocity and longer rapid run-out distance. Therefore, high excess pore pressure generated during failure must be responsible for the rapid motion.

5.5 EFFECTS OF GRAIN SIZE AND FINE-PARTICLE (LOESS) CONTENT

As mentioned in **Chapter 4**, sands with different grain size and fine-particle (loess) contents behaved differently in the undrained ring shear tests. To examine the grain size on the fluidization behavior of sands in flume tests, the generated excess pore pressure for the tests on S7 and S8 were examined; and meanwhile, the results of tests on M10, M20, and M30 were added to analyze the effects of fine-particle (loess) contents on the resulting motion of landslide mass.

5.5.1 Differences in Excess Pore Pressure Generation

When we focus on the variation tendency of generated excess pore pressure in relation to initial density index for the tests on S7 and S8 (Figure 5.5), it could be found that S7 and S8 had the same changing tendency, as mentioned in Section 5.4.1. However, an observation on these two curves could find that the generated excess pore pressure for S8 is generally greater than that for S7. It shows that finer sand S8 is easier to suffer from quick failure with higher excess pore pressure.

5.5.2 Differences in Resulting Motion of Landslide Mass

The effects of grain size on the resulting motion of landslide mass were efficient. As introduced above, for the tests on S7, there just appeared retrogressive slides; while in the tests on S8, rapid flowslides were initiated, showing completely different failure mode.

The effects of fine-particle (loess) on the resulting motion of landslide mass were examined by performing tests on S8 with different loess content. At first, the tests were conducted on loess with different initial void ratios. Because the flume was only 15 cm high, the effect of cohesion is relatively greater when the normal stress is relatively small. Under these conditions, flowslides did not occur; there was only surface erosion. However, by adding loess to S8, high-speed flowslides were produced. In this series of tests, the samples were made with different loess contents (10 percent, 20 percent, and 30 percent). To minimize the effects of variation of initial void ratio, the samples were formed by using the same damping method with the same 10-cm height. Due to difficulties in sample preparation, the initial densities were not the same, but were 1.01, 1.06, and 1.03 g/cm³. Their initial density indexes were 1.61, 1.50, 1.58, respectively (Table 5.1). From these limited test results, there was no obvious difference in generated excess pore pressures (Δu) at the time of failure; they were 0.56, 0.55, and 0.58 kPa for M10, M20, and M30, respectively. However, the flow behaviors varied

considerably. Thus, considerable attention was paid to the effects of fine-particle (loess) content on the motion of the initiated flowslides.

Figure 5.7 shows variation in sliding velocity in relation to sliding distance for samples with different fine-particle (loess) contents. As shown, for the tests on S8 and M10, completed curves (including the accelerating, decelerating and steady slow-sliding stages) occurred. However, for the tests on M20 and M30, the landslide mass continued to move without deceleration that might be caused by pore-pressure dissipation. This suggests that a mechanism for maintaining excess pore pressure be at work during motion. This mechanism was proposed by Sassa (1988a), where the maintaining of excess pore pressure was explained by the flotation of finer grains and the resulting increase of specific gravity of pore liquid. Due to pore pressure transducers placed at places of x_2 and x_3 did not work correctly, i.e., there was no data available to proving whether the generated pore pressure within the moving mass was kept without dissipation, the double cylinder mixing apparatus was used to examine the pore pressure maintaining during motion.

5.6 PORE PRESSURE MAINTAINING MECHANISM DURING MOTION THROUGH DOUBLE CYLINDER MIXING TESTS

To scrutinize the relationship of pore pressure maintaining and motion of soil mass, a series of ring-cylinder rotating tests was performed. By changing the rotating velocity, the variation of pore pressure within the moving mass was observed; and through conducting the tests on S7, S8, M10, M20, and M30, the effects of fines on the pore pressure generation were discussed.

According to Casagrande (1936), during shear deformation, the volume decrease of sand in loose state and the volume increase in the dense state would tend to produce the same "critical density" or "critical void ratio". Therefore it could be inferred that the sand would tend to the same void ratio after reaching steady state motion, now matter

the sand was in loose or dense state initially. Hence, in this test series, all the samples were placed by means of dry deposition without tamping, and the effects of initial density was not examined.

5.6.1 Test Phenomena

In this series, tests were conducted on the five samples mentioned above. Although the test phenomenon was differing from each other for different samples, it was found that in each test the measured pore pressure depended greatly not only on the rotating velocity, but also on the changing tendency of rotating velocity (in accelerating or decelerating process). Here the results of test on S8 will be used to illustrate the variation of pore pressure along with rotating velocity.

Figure 5.8 shows the test results for S8, where the pore pressure is plotted against rotating velocity (here the rotating velocity presents that of the mixing rods). As shown in this figure, when the rotating velocity increased from zero, the pore pressure increased consequently; however, after the rotating velocity was increased to a certain value (point T in Figure 5.8), the measured pore pressure was found to decrease with increasing rotating velocity. During the deceleration process (shown in a solid line), the pore pressure was found to decrease with decreasing rotating velocity. When we compare the generated pore pressure in different periods, it could be found that generally the measured pore pressures in the deceleration process were greater than those measured in the acceleration process (shown in a dotted line) when their rotating velocities were the same.

With respect to this increasing pore pressure, an interpretation was given by Sassa (1988a). It was pointed out that when the mixture of sample and water begin to move together, the grains of sample begin to float in the water, and then the mobilized specific gravity of the fluid becomes to increase, and this would necessarily result in the increase of pore pressure consequently. When the rotating velocity becomes greater, grains of

bigger size in diameter begin to float. If every grain floats in water, it could be concluded that the mixture is 100 percent liquefied, namely full liquefaction was resulted in. After point T shown in Figure 5.2, because the mixing rods rotated too fast (relative to the moving mixtures) that the mixtures could not move with the mixing rods together, this then made the mixtures being sheared, and therefore, a reduction in pore pressure was resulted in consequently, just as shown in this figure evidently. During deceleration process, with decreasing rotating velocity, grains of greater size will settle down, and then reduction of pore pressure would be result in as a consequence. But due to the delay in settling down for the floating grains, the grains in this deceleration process would be much more than that in the acceleration process, this would necessarily lead to the difference in pore pressures, with the pore pressure measured in the deceleration process being greater than that measured in the acceleration process even though the rotating velocities are the same.

It is obvious that the generated increment in pore pressure depends on the initial water level and sample height. To compare the effects of rotating velocity and samples, test results were normalized by the total normal stress (σ_t), and were presented by floating ratio(r_f) and pore pressure ratio (r_u). Floating ratio is a kind of pore pressure ratio (the same as excess pore pressure ratio in value) that could be referred to Sassa (1988a), and is formulated as:

$$r_f = \frac{u - u_s}{\sigma_t - u_s} \dots\dots\dots (5.1)$$

Where, u : measured pore pressure;

σ_t : total normal stress ($r_s h_d$);

u_s : static water pressure ($r_w h_w$), is regarded as the initial water pressure that was measured before the rotating;

r_w : unit weight of water, was regarded as 1.0 gf/cm³ during calculation;

r_s : unit weight of saturated soil, was obtained from the calculated dry unit weight ($r_d = \text{weight of the used sample} / \text{occupied volume}$) of the soil in cylinder and the corresponding void ratio (e), namely,

$$r_s = r_w \frac{e}{1+e} + r_d \dots\dots\dots (5.2)$$

It was pointed out that if every grain floats in water, namely 100 percent liquefied, $r_f = 1.0$.

Figure 5.9 presents an illustration of the test results in the form of floating ratio r_f and pore pressure ratio r_u , where the acceleration process is plotted by dotted line, and deceleration process by solid line. As shown, the floating ratio increases from zero with increasing rotating velocity and reaches 0.62 at 32.4 cm/sec, while the pore pressure ratio increases from approximately 0.68 to 0.88 correspondingly, with an increment of approximate 20%.

5.6.2 Effects of Sample

As mentioned above, the measured pore pressure during rotating depends on not only the rotating velocity, but also the sample itself. According to the test results, it was found that in all the tests, the pore pressure increased with increasing rotating velocity, and vice versa, the measured pore pressure for the same sample was greater in the deceleration process than that in the acceleration process, showing the same tendency as that described in Figure 5.8. To examine the effects of samples, the tests results for all these samples normalized by the total normal stresses are shown in Figure 5.10, in the form of floating ratio and pore pressure ratio. For clarity, the floating ratios corresponding to the acceleration process for all the tests are plotted in Figure 5.10a against the rotating velocity, while those corresponding to the deceleration process are presented in Figure 5.10b, the pore pressure ratio corresponding to the acceleration

process in Figure 5.10c, and the pore pressure ratio corresponding to deceleration process in Figure 5.10d. From Figure 5.10a, it could be seen that although the floating ratio increases with increasing rotating velocity for all the tests, the floating changing tendency along with rotating velocity is differing for different samples. Corresponding to a certain rotating velocity, for the samples in the order of S7, S8, M10, M20, and M30, namely when the sample becomes finer and the fine-particle (loess) content becomes greater, the generated floating ratio becomes greater, as reflected evidently by the change in curvature of the floating ratio versus rotating velocity plotted in Figure 5.10a. This phenomenon could be interpreted by the main factors controlling the generation of pore pressure during motion. As mentioned above, the increase in pore pressure is due to the floating of grains in the fluid that would increase the mobilized specific gravity of fluid. Finer grains are easier to float. Therefore, corresponding to a certain rotating velocity, there should have more grains for the finer sample involving in floating, and then the resulted pore pressure increment should be greater. Meanwhile, with increasing fine-particle (loess) content, the fine-particle in the mixture would increase, and then the cohesive coefficient would become greater, the increased cohesion coefficient then could prevent or delay the settlement of grains. At the same time, increased clay content would prevent the dissipation of generated pore pressure due to shear deformation. This could be seen from the changing tendency of M20 and M30 shown in Figure 5.10a. Because pore pressure ratio (shown in Figures 5.10c, d) is just another presenting form of the generated pore pressure, it could be seen that the variation tendency of pore pressure ratio in relation to rotating velocity for each sample is the same as that shown in Figures 5.10a, b. Therefore, a detailed description on the changing tendencies of pore pressure ratio in relation to rotating velocity for different samples is neglected here.

5.7 INITIATION PROCESS AND MOTION OF FLUIDIZED LANDSLIDES

5.7.1 Initiation Process of Fluidized Landslides

As mentioned before, fluidized landslides refer to those landslides where liquefaction is initiated and rapid motion is resulted in. Considering that fluidized landslides usually have small apparent friction angles, a criterion for judging the appearance of fluidized landslide was given as 10 degrees in apparent friction angle in Chapter 2, basing on the observation on some typical fluidized landslides. And then using this criterion, the fluidization behavior in undrained ring shear tests was discussed in Chapter 4. Therefore, in this flume test situation, a criterion for fluidized landslides should have the same apparent friction angle of 10 degrees, i.e., the excess pore pressure ratio should be greater than 0.74, given the internal friction angle of sands being 34 degrees.

For practice situation, the apparent friction angle reflects the final state of fluidized landslide, and then in ring shear test, the pore pressure ratio was calculated correspondingly by using the generated pore pressure at steady state when the soil was subjected to undrained shearing. However, for this flume test situation, when the failure was initiated, the soil mass was in a drained condition, and meanwhile, the measured pore pressure could just reflect that initiated at the beginning of the movement, not at the final state (steady state), therefore, it seemed difficult to analyze the initiation of fluidized landslides in flume tests by using the criterion given in chapter 2.

Nevertheless, as stated by Seed (1987), *"There is much evidence to show that if the pore pressure ratio in a soil do not build up to high values, e.g., exceeding a pore pressure ratio of about 60%, liquefaction (in any of its forms) will not be triggered in the soil. If the soil does not liquefy in the sense that a high pore pressure ratio, r_u is developed, then: (1) there is usually no problem of sliding since the soil retains high shear strength; and (2) there is usually no serious deformation problem."* From this statement, it could be seen that 0.6 in pore pressure ratio seemed to be a critical value to initiation of

liquefaction. Therefore, it seems practicable to use a criterion of 0.6 in pore pressure ratio that obtained from the beginning of the movement to judge the initiation of fluidized landslide in this flume test situation.

However, in this flume test situation, although the excess pore pressures at the beginning of the movement were measured, most of the values obtained from the normal stress transducers were incorrect, due to the small size of sample, effect of side friction, and other possible factors that are not clear. Thus it is difficult to make a direct calculation of pore pressure ratio from the observed pore pressure and normal stress. On the other hand, during sprinkling, there was settlement in the sample, this made the void ratio immediately before the failure differing from the initial void ratio, meanwhile, the saturation degree is different for soil layers in different height. Because the settlement of the soil layer and the water content in different soil layers were not observed, a theoretical calculation seemed difficult also. Due to these problems, in this flume test situation, the initial normal stresses were used as the references to the total normal stresses immediately before failure to estimate the excess pore pressure ratio approximately. Considering the measured pore pressure being that in a static place, not that within a certain soil mass during motion (in most situation, the pore pressure will increase with increasing moving velocity), here a modified criterion of excess pore pressure ratio being 0.5 will be used as the criterion for judging the initiation of fluidized landslide in flume tests.

As stated above, the excess pore pressures were generated during, rather than before, the failure, and the generation of excess pore pressure greatly depended on the initial relative density, and the sample itself. As shown in Table 5.1, in the series tests on S7, there was just one test (S7_{1.4}) where the estimated excess pore pressure ratio was greater than 0.5, while there were seven tests (tests S8_{0.3} – S8_{0.9}) where the estimated excess pore pressure ratios were greater than 0.5 in the series tests on S8; meanwhile, it could be found that in the series tests on mixtures of S8 with different loess content

(M10_{II.1}, M20_{II.1}, M30_{II.1}), all the estimated excess pore pressure ratios were greater than 0.5. Therefore, it could be concluded that the initiation of fluidized landslide depends not only on the initial relative density, but also (and much more) on the sample itself (its grain size and fine-particle content).

5.7.2 Motion of Fluidized landslides

As mentioned before, rapid movement will be necessarily commenced as the result of liquefaction for a practice fluidized landslide. Nevertheless, it is not to say that large movement will be necessarily resulted in, the motion of fluidized landslide greatly depends on the persisting of liquefaction, i.e., on the maintaining of high pore pressure.

As reflected in Table 5.1, among the tests where fluidized landslides were initiated, the peak values of velocity during motion for all of them were greater than 10 cm/sec, except for the test of S8_{II.7}. This exception may be due to the problem in the sliding-distance-measurement system, sometimes, the foam ball connecting with the liner displacement transducer (see Figure 3.3) failed to move with the moving soil mass together. Considering the prototype size, it could be said that rapid movement had been initiated in these fluidized landslides. Of course, there were some tests (Tests S8_{II.10} ~ S8_{II.12}) where the moving velocities were greater than 10 cm/sec. It could be interpreted as follows: although the measured excess pore pressures at the beginning of the failure were small, i.e., fluidization was not initiated (judged from the measured excess pore pressure during failure), high pore pressure might be initiated during motion, according to the results of double cylinder mixing tests.

The dissipation of generated high pore pressure may be the main factor controlling the failure mode and run-out distance. As shown in Figure 5.2, the tests on S7 just showed retrogressive slide, without any flowslide, even though there were two tests were recognized as fluidized landslides, and the resulted run-out distances were small in general. This could be interpreted by the greater permeability of S7. During failure, due

to the quick shearing, pore pressures were generated within the shear zone, but due to the great permeability, they dissipated very quickly, and then the once fluidized landslide stopped very soon with a small run-out distance. On the contrary, due to the low permeability of S8, it became difficult for the generated high pore pressure to dissipate, and then, large movement could be resulted in. Meanwhile, when the fine-particle (loess) content became greater, the permeability of sample would be necessarily reduced, and then the dissipation of generated high pore pressure would become more difficult to happen; meanwhile, with increasing moving velocity, much more grains would float during motion. Hence, the resulted fluidized landslide would be characterized by larger run-out distance and greater moving velocity, with the sand becoming fine and fine-particle (loess) content becoming greater. This tendency could be seen from Table 5.1. In terms of magnitude, for a slope of only 10-cm thick in prototype, this tendency was phenomenal.

5.8 COMPARISON OF RING SHEAR TEST AND FLUME TEST

As aforementioned, undrained ring shear tests were carried out to simulate those failures that happened so quickly that pore pressure could not dissipate immediately within the quite short period of failure, and during the failure, shear zone was formed and liquefaction was initiated within the shear zone. Flume tests represented a kind of failure situation that the soil mass was in drained condition, and the build-up of pore pressure was resulted from the collapse of contractive soil structure where little if any grain crushing was involved, and dependent on the permeability of soil mass. Therefore, these differences would necessarily result in differing tendency in the generation of pore pressures. As shown in Figure 4.21b and Figure 4.22b, when the soil was in undrained condition, with decreasing initial relative density (soil becomes looser), the generated pore pressure at steady state would be greater, showing that fluidization was becoming easier to happen. While results obtained from flume tests showed that there was an optimal density for high pore pressure to generate, as shown in Figure 5.5.

Nevertheless, the results from ring shear tests showed good consistencies with those obtained from flume tests in many aspects. In undrained ring shear tests, S8 of finer grain size showed to be easier to suffer from fluidization failure than S7. Flume tests on S8 and S7 showed the same tendency: most of the tests on S8 showed fluidized failure, while just one of the tests on S7 did, as shown in Table 5.1. Ring shear tests on the sand containing fine-particle (loess) showed that with increasing fine-particle (loess) contents, both peak shear strength and steady state shear strength became smaller, e.g., the sample becomes easier to suffer fluidization failure. Meanwhile, with increasing fine-particle (loess) content, dissipation of the high pore pressure generated in the shear zone became slower when the shear box was turned into drained condition. This means the possible run-out distance of fluidized landslide would become greater. This tendency was certified by the flume tests on the mixtures of S8 with different fine-particle (loess) contents, as shown evidently in Figure 5.7. Therefore, it could be concluded that the initiation and motion of fluidized landslides in practice situation could be predicted by using the ring shear tests results.

5.9 SUMMARY

Using a small flume, a series of tests has been conducted to cause rainfall-induced slope failure. Based on monitoring of sliding distance and pore pressures, the process of excess pore pressure generation in relation to sliding distance is discussed. A set of test results on the temporal and longitudinal variation of sliding velocity for the initiated flowslide is presented. By changing the initial dry density and performing tests on sands with different grain sizes, the effects of these factors on the generated pore pressure and resulting motion of failed soil mass have been analyzed. To investigate the influence of fine-particle (loess) contents on flowslide motion, samples are prepared by mixing loess into the silica sand at three different contents. A series of tests on these samples has been carried out in which the different modes of flowslide motion are observed; and then to examine the pore-pressure generation during motion, double cylinder mixing

tests have been conducted on sands with different grain size and fine-particle (loess) contents. Basing on these tests results, finally the initiation and motion of fluidized landslides have been discussed.

Chapter 6

CASE STUDY ON THE MECHANISM OF A FLUIDIZED LANDSLIDE TRIGGERED BY THE AUGUST 1998 HEAVY RAINFALL, FUKUSHIMA PREFECTURE, JAPAN

6.1 INTRODUCTION

There was a heavy rainfall distributed in the Northeastern Japan from August 26 to 31, 1998. During this rain-falling period, many landslides and debris flows occurred, and great losses of properties and lives were resulted in. Around the area of Taiyonokuni, a place of Nishigo Village, Nishi-Shirakawa County, Fukushima Prefecture, 13 landslides were triggered with high mobility, and among them, the biggest one was the Karamatsu-so landslide, which destroyed a general welfare institution naming Karamatsu-so, and five deaths were brought in. Although all these landslides were characterized by deep scarps, the bedrock above which sliding surface was developed, was relatively gentle. Nevertheless, irrespective of the gentle slope angle and small scale, almost all these landslides were characterized by high mobility and long run-out distance.

These failures are of great interesting, because this kind of area does not belong to the prevention area according to two Japanese laws concerning slope hazards. One is the

Landslide Prevention Law issued in 1958, which is chiefly to prevent reactivated large-scale landslides in gentle slopes (the characteristic landslide topography is visible) on which houses or paddy fields are constructed; the other is the Law for Prevention of Failure of Steep Slopes issued in 1969, which aims to the prevention of small-scale shallow landslides in steep slopes back of houses (Sassa, 1999). The source area of the landslide before failure is neither steep nor showing old landslide topography. The landslide is just virginal, which is induced initially by the rainfall. Therefore, how could these failures with high mobility be initiated on gentle slopes is of great interesting, and it is highly desirable to make the mechanism of this kind of failure clear.

As mentioned previously, among these landslides, Karamatsu-so landslide is the biggest and of the most hazards. However the motion was stopped by houses and the deposits were moved away immediately after the failure for rescue, to examine the characteristics of these landslides and make the sliding mechanism clear, another long-runout landslide, Hiegaesi landslide, triggered by the same rainfall and located in Hiegaesi, Otakura, approximate 3 km south to Taiyonokuni, was investigated in detail. Landslide mass of this long-runout landslide slipped out of the source area, traveled across a drain channel, and deposited in a paddy field after moved a long distance. This landslide was kept in natural state without any man-made disturbance. This made the investigation on the mechanism of initiation, motion and deposition possible.

6.2 LANDSLIDE PROPERTY

Both of the Karamatsu-so landslide and the Hiegaesi landslide located in Nishigo village, Fukushima Prefecture, approximate 6 km west of Shin-Shirakawa station of Shin-Kansen super-express (as shown in **Figure 6.1**). **Figure 6.2** is a photograph taken by Dr. Chigira when he investigated the geo-hazards induced by this rainfall as a member of the Urgent Investigation Team of Japanese Landslide Society. The sliding direction is near due west. The main scrape is visible at the left of the photograph. The

landslide mass deposited above the rice plants on the paddy field. Trees standing on the landslide mass show that this fluidized landslide moved as a block. During the heavy rainfall period, the bottom of the paddy field was full of water.

On November 3, this landslide was investigated in detail by Sassa and colleagues. The height of the slope where the landslide occurred is several tens meters. It is observed that all the failed mass had slipped out of the source area, divided into three fingers, traveled across a drain channel, and finally run into and deposited on the paddy field. It was observed that the landslide almost jumped over the drain channel, showing very high mobility. By means of a total station, the plane shape and the central longitudinal section of the landslide were surveyed. **Figure 6.3a** illustrates the plane shape and traveling distances of the three fingers of this landslide. They are 67.3 m, 63.6 m, and 48.2 m from the measure point at the end of the source area, respectively. **Figure 6.3b** is the central longitudinal section. Travel angle of the landslide, which is defined as an inverse tangent function of the ratio of landslide height to landslide total length (see **Figure 6.3b**) (Cruden and Varnes, 1996), is about 11.2 degrees, substantiating its high mobility and long-runout character.

Figure 6.4 is a photograph showing the source area. The width, length and depth of the surface of rupture are approximately 23.0 m, 32.8 m, and 2.5 m, respectively; and the volume of the landslide mass is approximately 1200 m³. The angle of the base slope is approximately 25 degrees. The base slope consisting of dacite tuff is dominant, and it could be seen clearly in this photograph that a yellow bond of pumice layer is over the dacite tuff. And it was examined that the landslide occurred in the weathered dacite tuff layer.

A common phenomenon between the landslides in this site and that in Karamatsu-so is that, after the landslide mass slipped from the source area, the bamboo grasses in front of the source area were just brought downwards to the sliding direction, and they are

keeping alive without any obvious damage in their leaves (Figure 6.5) From this phenomenon, it could be inferred that when the landslide mass slipped on them, the shear force acting on bamboo grasses be very small, showing the possibility of a full fluidization failure.

To investigate the sliding behavior of the landslide during motion, especially the formation of shear zone, a pit was dug in the deposition area. The pit location is indicated in Figure 6.3 (Point P). Figure 6.6 is a photograph taken in the pit. As shown, the rice plants were brought down towards the sliding direction, with the landslide mass overlaying on them. A soil-layer, approximately 20 cm in thickness, was confirmed as the sliding zone, which was differing from the soil above this shear zone evidently in color. The soil within the shear zone is completely disturbed due to the long-distance shearing, while the overlaying soil mass remains relatively integrated with little if any disturbance. Meanwhile, the soil within the shear zone is softer and greater in water-content than the soil layer overlaying on it, examined by hand touching. To examine whether there is grain crushing or not, two samples were taken from this pit, one from the shear zone and another from the soil layer above the shear zone, and laboratorial grain size analyses were performed later. Figure 6.7 presents the analysis results of grain size distribution of the two samples. The soil from the sliding zone is obviously finer, compared with the soil above the shear zone, substantiating that grain crushing occurred within the shear zone. From the visible gray tuff at the bottom of the pit, it could be inferred that this shear zone formed from the source area was kept through the whole long distance movement. Therefore, it could be concluded that if there was liquefaction happened, it must be limited in this shear zone, namely, be a kind of sliding surface liquefaction.

According to the field observation, besides the grain crushing that is confirmed by the results shown in Figure 6.7, another two questions are raised; how was the landslide initiated with very small shear resistance when it slipped out of the slope, and why

could the landslide mass travel over the rice plants for such a long distance? To make these problems clear, using the sample taken from the source area (sample S3, shown in Figure 6.3) and sample S2, three sets of ring shear tests were carried out.

6.3 RING SHEAR TESTS

6.3.1 Ring Shear Test on the Sample From Source Area

As described above, the landslide showed a small friction resistance after the soil mass slipped out of the source area. During the heavy rainfall, the strongly weathered dacite tuff layer ensures that the landslide mass above the fresh base rock be fully saturated. As observed in the field, the landslide shows high-mobility character. Therefore, it is inferred that high pore pressure was generated during the failure.

To study the mechanism of soil mass slipped out of the source area, with small shear resistance, two tests were planned. The first one is saturated undrained ring shear test by means of speed-control to observe the generation of pore pressure, and its purpose is to examine whether the soil from the field is liquefiable. The second one is saturated drained ring shear test by means of torque-control, and its purpose is to examine whether high mobility with small shear resistance could be initiated under drained condition, because in the field, the depth is small and the soil might be in drained condition when the failure was initiated.

6.3.1.1 Saturated undrained speed-control ring shear test

This test is to examine whether the soil from the source area is liquefiable or not. At first, the sample from the source area is saturated and a high saturation degree ($B_D = 0.98$) is ensured with help of CO_2 and de-aired water. And then, the sample is normally consolidated at a normal stress of 40 kPa, which is corresponding to the initial normal stress acting on the soil mass at the bottom of the landslide mass in the source area before failure. To observe the generation of pore pressure along with the shear

deformation correctly, speed-controlled method with a final shear speed of 2 mm/sec was selected during this undrained test.

Figure 6.8a presents the variation of normal stress, pore pressure, and shear resistance in relation to shear displacement. To check the shear behavior at the beginning of the test more precisely, logarithm shear displacement is used as the abscissa. As shown in this figure, normal stress was kept constant through the whole shear process. With increasing shear displacement, shear resistance increased gradually from zero, and when the shear displacement reached 0.5 mm, shear resistance reached its peak value (point "B"). Thereafter, it decreased with the increasing shear displacement. After sheared to 100 mm, the shear resistance reduced approximately to zero. Meanwhile, it could be found that pore pressure increased quickly along with the increasing shear displacement in the earlier shearing period, and reached to approximately 37 kPa, very close to the normal stress at the shear displacement of 100 mm.

Figure 6.8b shows the corresponding effective stress path (ESP) and total stress path (TSP) monitored in the test. From the start point "A", shear resistance increased directly to point "B" (black points). Then due to the quick generation of excess pore pressure, the effective stress moved to point "C" almost horizontally. After point "C", the shear resistance decreased rapidly. When effective stress was about 20 kPa, the effective stress path reached the failure line (approximate 41 degrees in inclination angle), and decreased along it to a very small value (approximate zero). In this effective stress path, it is recognized that the shear resistance reached its peak strength before reaching the failure line, and there is quick shifting of effective stress path from point "B" to the failure line, showing a collapse failure process that could be resulted from the failure of metastable soil structure. The late part of effective stress path shows a typical stress path of sliding-surface liquefaction.

To examine the grain crushing susceptibility of the sample under the applied small

normal stress of 40 kPa, after the test was finished, the shear box was opened, and the soil within the shear zone was taken out for grain size distribution analysis. **Figure 6.9** presents the results, where the grain size distribution of the sample from the shear zone is illustrated by the line with filled point, while that of the original sample from the source area by the line with blank point. As presented, the line for the sample from shear zone is locating quite above that for the original sample, showing that huge grain crushing happened within the shear zone, even though the normal stress is very small.

As illustrated in **Figure 6.8b**, the stress path, falling down along the failure line, indicates that the generation of the excess pore is mainly caused by grain crushing within the shear zone along with the shearing. Therefore, it is concluded that the soil mass from the source area is liquefiable, due to the high grain crushing susceptibility.

6.3.1.2 Saturated drained torque-control ring shear test

Although the soil mass from the source area is certified liquefiable in undrained condition, considering that the soil mass in the source area is just 2.5 m in thickness, and undrained condition could not be ensured during the failure. Therefore, it is desirable to examine whether liquefaction could be initiated in drained condition. With the same method as described above, the sample was prepared, saturated (with high saturation degree, $B_D = 0.98$), and normally consolidated at normal stress of 40 kPa. Thereafter, shear stress is applied at a loading rate of 0.1 kPa/sec until sample failed, while keeping the normal stress being constant and shear box being in drained condition. In this test, medium gear is selected.

Figure 6.10 illustrates the test results, where the variation of normal stress, shear resistance, and pore pressure in relation to elapsed time are presented in **Figure 6.10a**; and variation of sample height and shear displacement in relation to elapsed time in **Figure 6.10b**; **Figure 6.10c** shows the corresponding effective stress path. As illustrated in **Figures 6.10a, b**, with increasing shear stress, shear displacement increased slowly;

after approximate 135 seconds (Dotted line A), shear displacement began to increase a little more quickly, while the sample height began to decrease obviously along with the further increasing shear stress. During this period, the monitored shear displacement probably was resulted from the creep deformation within the soil mass, and the decrease in sample height might be resulted from the deformation or the failure of some soil structures; however, no pore pressure was monitored during this period, probably due to the lower pore pressure generation rate and relatively quicker dissipation rate. Nevertheless, after 235 seconds (Dotted line B), shear displacement showed quicker increasing, and then sample height decreased more quickly, along with the time. This quicker change in sample height resulted in the quick built-up of pore pressure, not only within, but also outside the shear zone; as the result, a transient increase in pore pressure was monitored (as shown in Figure 6.10a), irrespective the drained condition. After a short duration (from dotted line B to dotted line C, approximate 7 seconds), the sample failed, and shear resistance decreased quickly until to zero. Thereafter, along with the elapsed time, shear resistance recovered slowly due to the slow but existing dissipation.

As shown in Figure 6.10c, when the shear stress increased from A, the start point, the effective stress path (ESP) raised almost vertically to point B, and after that, due to the quick pore pressure generation, ESP shifted left-upward but did not reach the failure line (obtained in Figure 6.8b), fell down to zero, and finally tended to the End point. Because the shear box is in drained condition, and the pore pressure within the shear zone was not monitored correctly, then the ESP after the failure point did not fall down along the failure line. Nevertheless, the shear resistance was monitored correctly, and the apparent friction angle in this drained test situation was approximately 7.0 degrees.

From these results presented above, it is concluded that full liquefaction could be initiated even in drained condition. As a possible reason, it could be interpreted as follows: high containing of fines (greater than 40% in Figure 6.9) makes the permeability very slow, and then enables the accumulation of pore pressure during

shearing. This might be the main reason why pore pressure was monitored accompanying the faster changing in shear displacement and sample height in the drained condition after dotted line B, as shown in Figure 6.10a, even though this monitored pore pressure could only present that above the shear zone (see the measurement of pore pressure in Figure 3.2e). Meanwhile, grain crushing increases the fines within the shear zone, while makes the quick generation of pore pressure possible, and then decreases the permeability further more. For this reason, high pore pressure was accumulated quickly within the shear zone, and shear resistance decreased consequently to a very small value within limited shear distance (0.7 m), and then landslide soil mass could slip out of the source area rapidly, with little if any damage to the grasses. It is worth to note here that although the permeability is small, the sample height in the ring shear box is limited (the thickness above the shear zone was less than 5.5 cm at the point of full liquefaction), the dissipation rate of pore pressure from the shear zone must be quite faster than that in the field situation (where the depth is approximately 2.5 m). Therefore, provided that soil mass within the shear zone on the field being in drained condition, full liquefaction failure could be initiated and the recovering of shear strength could be much slower than that in this drained ring shear test situation.

With these test results, the small friction resistance phenomenon observed in the source area of fluidized landslide can be well explained. As confirmed by the field grain crushing data, the soil within the sliding zone has high grain crushing susceptibility. During the heavy rainfall, the soil layer was fully saturated. Along with the increasing pore pressure induced by rainfall, shear resistance of the landslide mass reduced. Then through a creep deformation at first, the complete failure of soil mass was followed. It can be assured that high excess pore pressure is generated quickly after the failure, and then quick reduction of shear resistance is resulted consequently. Loose structure and high grain crushing susceptibility of the soil are the main reason for the accumulation of

great excess pore pressure. And the fines (including the original fines and newly formed fines due to grain crushing) reduce the permeability of soil and then retard the dissipation of generated high pore pressure, and finally enable the high mobility with long run-out distance.

6.3.2 Examining the Motion of Failed Landslide Mass on the Rice Plants Based on Ring Shear Test

As aforementioned, the maintaining of generated pore pressure is of great importance to the motion of a fluidized landslide. It is made clear that high pore pressure was generated and kept within the shear zone while the soil slipped out of the source area. Because the failed landslide mass run into the paddy field immediately after it slipped out of the slope and kept sliding on the rice plants, the shear between the soil and rice plants seemed to be the most important controlling factor for this fluidized landslide. Therefore, it is desirable to examine the shear behavior of soil mass shearing along the rice plants, and the maintaining of pore pressure during motion.

The sample was prepared following the procedures illustrated in Figure 6.11. In the lower part of the shear box, the soil taken from the paddy field was set with 5 clusters rice plants vertically inserted in it. There were 15 pieces of wet rice plants in each cluster. Thereafter, the rice plants were brought down towards the direction opposite to that of the shearing near the boundary between upper part and lower part of the shear box. Then, the soil taken from the landslide mass (sample S2) was set on the rice plants.

After saturated, the sample was normally consolidated under a normal stress of 40 kPa. In this test case, only a small B_D value of 0.55 was obtained, probably due to the air left in the stems of rice plants. The shear box was then switched to undrained condition, and thereafter speed-control ring shear test was performed. Shear speed was also set as 2 mm/sec.

Figure 6.12a shows the variation of the normal stress, pore pressure and shear resistance in relation to the shear displacement, where logarithm abscissa of shear displacement is used to have a good view of the initial shearing period. As the shear begin, the shear resistance increases rapidly, and reaches its peak value (point "A") after 20-mm of shearing. Thereafter, the shear resistance reduces along with the shearing, and reaches the steady state at the point of shear displacement being 800 mm. The pore pressure showed an increasing tendency through the whole shearing process, except for a transient reduction. This transient reduction might be resulted from the air left in the stem of rice plants; with increasing pore pressure, water could be extruded into the stem, and then lead to the miss measurement of pore pressure. Nevertheless, from the reduction tendency of shear resistance, it could be inferred that the corresponding pore pressure within the shear zone should have no reduction.

Figure 6.12b shows the corresponding effective stress path (ESP) and total stress path (TSP). A failure line of 36.5 degrees is drawn based on the upper boundary of the shear resistance. Some effective stress points shift from the failure line (point "B"), probably because of the miss-measurement of pore pressure. However, after sheared approximately to 800 mm (point "C"), the sample reaches the steady state, where the shear strength does not decrease further more, and the apparent friction angle obtained from these stress paths is 8.0 degrees. This value shows a good consistency with that of 11.2 degrees for the actual landslide on the field.

Because the failed soil mass was just 2.5 m in thickness in the source area, and was becoming thinner along with motion, it is necessary to have an examination on the dissipation of generated pore pressure form the shear zone. Therefore, the dissipation form the shear zone in ring shear test was examined by switching the shear box to drained condition and observing the recover of shear resistance after the undrained test on the soil mass and rice plants, while keeping the lower part of ring shear box rotating at a speed of 0.1 mm/sec. **Figure 6.13** illustrates the results, where the shear resistance

is plotted against the elapsed time. As shown, after the shear box was turned to drained condition, in the first 30 seconds, there was almost no change in the shear resistance, e.g., no dissipation of pore pressure from the shear zone; and after that the shear resistance recovered very slowly with the elapsed time due to extremely slow dissipation. This result shows good consistency with that obtained from the test on M30 shown in Figure 4.23, where the maintaining of generated pore pressure was interpreted as the result of increasing fines. Here let us see the grain size distribution of the soil from the source area (Figure 6.9), it is not difficult to find that this sample from the source area contains great amount of fines, especially clay content reached to approximately 10%, and at the same time, grain crushing made the grain size finer after a certain distance of shearing. These fines made the permeability extremely slow and then enable the fluidized landslide to travel a long distance, by keeping the generated high pore pressure within the shear zone for a long time.

Because the shear box of the ring shear apparatus is not transparent, whether the shear was initiated between the rice plants and soil mass or not is questionable; to make it clear, the shear surface between the rice plants and landslide mass after the drained test was exposed by cutting it. Figure 6.14a shows a section of the sample, and two pins indicate the border between rice plants and soil from the landslide mass. Figure 6.14b shows a scratch on the bottom of landslide mass caused by the relative motion with rice plants. It is obviously confirmed that the sliding occurred within the border between the rice plants and landslide mass.

Although the undrained shear strength between rice plants and soil mass showed that the apparent friction angle at steady state (8.0 degrees) is higher than that obtained from the undrained tests on the soil only (where a full liquefaction was initiated), compared with those obtained from the drained shear test (7.0 degrees) and field survey (11.2 degrees), it could be concluded that they showed good consistency with each other. The test on rice plants and landslide mass indicated that, high fines content and high grain

crushing susceptibility make the shear between the rice plants and landslide mass must be in an undrained condition, or at least the dissipation rate is extremely small that the generated high pore pressure could be kept within the shear zone, and then enable the failed soil mass to have a large travel distance even in the horizontal paddy field.

6.4 SUMMARY

Based on the field survey and observation, a fluidized landslide was introduced and examined. It was made clear that this landslide is a kind of sliding surface liquefaction failure. On the basis of laboratory ring shear test results, the initiation and motion mechanism of this fluidized landslide were examined. It was found that high grain crushing susceptibility and high content of fine particles made the accumulation and maintaining of high pore pressure possible, and then enabled the failed soil mass to slip out from the source area with high mobility and travel a large distance on the horizontal paddy field.

Chapter 7

CONCLUSIONS

The initiation and motion of fluidized landslides are complicated processes. Different test approaches were used to obtain information from various aspects. The findings obtained from different test approaches were suitable only to the particular conditions of the experiments. Nevertheless, a common result was found that fine-particles played an important role for both the initiation and motion of fluidized landslides. Summarizing the main results of the study:

1. From the ring-shear test results, it was found that in undrained condition, the brittleness index depended greatly on the initial stress state, i.e., brittleness index became greater with larger values of initial shear stress and normal stress; also, both the peak and steady state shear strengths became smaller when the sands became finer in grain size or greater in fine-particle content, given the same initial density and stress state.
2. From the flume tests on sands with the same thickness but different initial densities, it was observed that there was an optimal density for high pore pressure generation for a given sand, at which both the corresponding run-out distance and peak velocity were the greatest. A possible explanation is that below this density, pore pressure

dissipation occurred more quickly due to higher permeability, while above this density less pore pressure was generated because the sand was denser.

3. Observations on the motion of fluidized soil mass in flume tests revealed that sands with greater fine-particle content could tolerate high-speed motion without deceleration. Meanwhile, from double cylinder test results, it was found that sands with greater fine-particle content had greater excess pore pressure when the rotating speed was the same. Therefore, it could be concluded that fine-particles played an important role for maintaining excess pore pressure during motion, i.e., fine-particles floated more easily during motion and then increased the excess pore pressure.
4. From the observations of a pit dug in the deposition area of the Fukushima fluidized landslide, it was found that a shear zone was formed on the bottom of this landslide and fine-particles existed in this shear zone. From the results of ring-shear tests on the volcanic deposits collected from the source area of this landslide, it was inferred that grain crushing in the shear zone caused the generation of high excess pore pressure initiating fluidization; meanwhile, the high content of fine particles in the original soil and the newly formed fines by crushing reduced the permeability further and made the dissipation of excess pore pressure from the shear zone more difficult. The combination of these factors resulted in the fluidized landslide with high-speed and long run-out distance.

It is worth noting that all these results were based on tests on sands, and the examination of the findings to real fluidized landslides is limited. However, this study gives an interpretation for the mechanism of initiation and motion of fluidized landslides.

CONTENTS OF THIS THESIS ARE BASED ON PAPERS AS FOLLOWS:

1. Gonghui WANG & Kyoji SASSA. (1999). Factors affecting rainfall-induced flowslides in laboratory flume tests. *Géotechnique*, 1999. (In contribution)
2. Gonghui WANG & Kyoji SASSA. (1999). Excess Pore Pressure Generation during failure and the resulting movement of sand slope in Flume test by Rainfall. *Journal of Japan Landslide Society*. (In Japanese with English abstract) (In press)
3. Gonghui WANG & Kyoji SASSA. (1999). Effects of Density, Stress State and Shear History on Sliding-Surface Liquefaction Behaviour of Sands in Ring-shear Apparatus. "Slope Stability Engineering" Proceedings of the international Symposium on Slope Stability Engineering-IS-SHIKOKU'99, MATSUYAMA, Japan, pp. 583-588.
4. Fawu Wang, Gonghui Wang and Kyoji Sassa. (1999). Mechanism of a long run-out landslide triggered by the August 1998 heavy rainfall in Fukushima Prefecture. *Proceedings of 8th international Symposium on Landslides*. Cardiff, Wales, UK, 2000 (In press).

ACKNOWLEDGEMENTS

The author wishes to express his deepest appreciation to his supervisor, Professor Kyoji SASSA, for his continued guidance and encouragement. His ideas, consultations and supports were invaluable.

The author would like also to express his appreciation to Associate Professor Hiroshi FUKUOKA for his assistances during testing. Most sincere thanks are due to Professor Kazuo OKUNISHI, Professor Masahiro CHIGIRA, Professor Hideo SEKIGUCHI, Associate Professor Akira SUEMINE, and Dr. Atsuo TAKEUCHI, for their valuable advices in their lectures, field investigations, and seminars.

Thanks are put forward to the former and present postgraduate students in Landslide Section, Disaster Prevention Research Institute, Kyoto University, in particular to Dr. Fawu WANG and Dr. Gen FURUYA. Many thanks go to Miss T. Kubota, Forestry and Forest Products Research Institute, Ibaraki, Japan, for her helps in the flume test.

The author acknowledges the financial support provided by the Japanese Government. Meanwhile, the supports provided by his old affiliation, Lanzhou University, China, during his studying in Japan are also appreciated.

Finally, my special thanks go to his wife, Li Fengying and his daughter, Wang Di. It is their endless love, supports and encouragements that make the author being able to indulge in his research completely. Meanwhile, the author extends his deepest gratitude to his parents, his brothers and young sister, for their love, encouragement and patience.

BIBLIOGRAPHY

1. Alarcon-Guzman, A., Leonards, G. A. and Chameau, J. L. (1988). Undrained monotonic and cyclic strength of sands. *J. Geotech. Engrg., ASCE*. 103(10), 1089-1110.
2. Anderson, S. A., and Sitar, N. (1995). Analysis of Rainfall-Induced Debris Flow. *J. Geotech. Engrg., ASCE*. 121(7), 544-552.
3. Been, K. & Jefferies, M. G. (1985). A state parameter for sands. *Géotechnique* 35, No. 2, 99-112.
4. Been, K., Jefferies, M. G. & Hachey, J. (1991). The critical state of sands. *Géotechnique* 41, No. 3, 365-381.
5. Been, K., Jefferies, M. G. & Hachey, J. (1992). Discussion: The critical state of sands. *Géotechnique* 42, No. 4, pp655-663.
6. Bishop, A.W. 1967. Progressive failure-with special reference to the mechanism causing it. *Proc. Geotech. Conf., Oslo, Norway* 2, 142-150.

7. Bishop, A.W., Green, G. E., Garge, V. K., Andersen, A. & Brown, J. D. (1971). A new ring shear apparatus and its application to the measurement of residual strength. *Géotechnique* 21, No. 1, 273-328.
8. Bishop, A.W. (1973). The stability of tips and spoil heaps. *Q.J. Engrg. Geol.* 6, 335-376.
9. Brand, E. W. (1981). Some thoughts on rainfall induced slope failures. *Proc. 10th Int. Conf. on Soil Mech. and Found. Engrg.*, A. A. Balkema, Brookfield, Vt., pp.373-376.
10. Brenner, R. P., Tam, H. K., and Brand, E. W. (1985). Field stress path simulation of rain-induced slope failure. *Proc. 11th Int. Conf. on Soil Mech. and Found. Engrg.*, A. A. Balkema, Brookfield, Vt., Vol. 2, pp.373-376.
11. Bromhead, E. N. (1979). A simple ring shear apparatus. *Ground Engineering*, Vol. 12, No. 5, pp. 40-44.
12. Casagrande, A. (1936). Characteristics of cohesionless soils affecting the stability of slopes and earth fills, *Journal of the Boston society of civil engineers*, reprinted in Contributions to soil mechanics, 1925 to 1940, Boston Society for Civil Engineers, 257-276.
13. Casagrande, A. (1938). The shearing resistance of soils and its relation to the stability of earth dams. Proceedings, Soils and Foundation Conference on the U. S. Engineer Department.
14. Casagrande, A. (1971). On liquefaction phenomenon. *Géotechnique* 21, No. 3, 197-202.

15. Casagrande, A. (1976). Liquefaction and cyclic mobility of sands-a critical review. *Harvard Soil Mechanics Series*. 88.
16. Castro, G. (1969). *Liquefaction of sands*. Ph.D. Thesis, Harvard University, Cambridge, Massachusetts.
17. Castro, G. (1975). Liquefaction and Cyclic Mobility of Saturated Sands. *Journal of Geotechnical Engineering*, ASCE Vol. 101, No. 6, pp551-569.
18. Castro, G., Seed, R. B., Keller, T. O., and Seed, H. B. (1992). Steady-state strength analysis of Lower San Fernando Dam slide. *Journal of Geotechnical Engineering*, ASCE, 118(3), 406-427.
19. Castro, G. & Poulos, S.J. (1977). Factors affecting liquefaction and cyclic mobility. *J. Geotech. Engrg. Div., ASCE*. 103, 501-516.
20. Castro, G., Enos, J. L., France, J. W. and Poulos, S. J. (1982). Liquefaction induced by cyclic loading. *Report to National Science Foundation*, Washington, DC, No. NSF/CEE-82018.
21. Cruden, D. M. and D. J. Varnes (1985): *Landslides: Investigation and Mitigation*. Transportation Research Board, National Academy of Science.
22. Eckersley, J. D. (1985): Flowslides in stockpiled coal. *Engrg Geol.* 22, 13-22.
23. Eckersley, J. D. (1990). Instrumented Laboratory Flowslides. *Géotechnique* 40, No. 3, 489-502.
24. Finn, W.D.L. (1981). Liquefaction potential: developments since 1976. *Proc., 1st International Conference on Recent Advances in Geotechnical Earthquake Engineering and Soil Dynamics*, St. Louis, 2, 655-681.

25. Finno, R.J., Harris, W.W., Mooney, M.A., and Viggiani, G. (1996). Strain Localization and Undrained Steady State of Sand, *Journal of Geotechnical Engineering*, ASCE, Vol. 122, No. 6, pp. 462-473.
26. Finno, R. J., W. W. Harris, M. A. Mooney and Viggiani, G. (1997). Shear bands in plane strain compression of loose sand. *Géotechnique* 47, No. 1, 149-165.
27. Georgiannou, V. N., Burland, J. B. & Hight, D., W. (1990). The undrained behaviour of clayey sands in triaxial compression and extension. *Géotechnique* 40, No. 3, 3431-449.
28. Gibo, S. (1994). Ring shear apparatus for measuring residual strengths and its measurement accuracy. *Journal of Japan Landslide Society*, Vol. 31, No. 3, pp. 24-30.
29. Guo Tianqiang & Shamsheer Prakash. (1999). Liquefaction of silts and silt-clay mixtures. *Journal of Geotechnical and Geoenvironmental Engineering*, ASCE, Vol. 125, No. 8, pp. 706-710.
30. Hird, H.H. & Hassona, F.A.K. (1990). Some factors affecting the liquefaction and flow of saturated sands in laboratory tests. *Engrg. Geol.* 28, 149-170.
31. Hungr, O. and Morgenstern, N., R. (1984a). Experiments on the flow behaviour of granular materials at high velocity in an open channel. *Géotechnique* 34, No. 3, 405-413.
32. Hungr, O. and Morgenstern, N., R. (1984b). High velocity ring shear tests on sand. *Géotechnique* 34, No. 3, 415-421.
33. Inokuchi, T. (1985): The Ontake rock slide and debris avalanche caused by the

- Naganoken-Seibu earthquake, 1984. *Proc. 4th International Conference and Field Workshop on Landslides*, pp.329-338.
34. Ishihara, K. (1993). Liquefaction and flow failure during earthquakes. *Géotechnique* 43, No. 3, 349-451.
35. Ishihara, K. and Koseki, J. (1989). Cyclic shear strength of fines-containing sands. *Proc. Earth-quake Geotechnical Engineering, 12th International Conference on Soil Mechanical and Foundation Engineering, Rio de Janeiro*, pp. 101-106.
36. Ishihara, K., Okusa, S., Oyagi, N., & Ischuk, A. (1990). Liquefaction-induced flowslide in the collapsible loess deposit in Soviet Tajik. *Soils and Foundations* 30, No. 4, 73-89.
37. Kamai, T. (1998). Monitoring the process of ground failure in repeated landslides and associated stability assessments. *Engineering Geology*, 50, 71-84.
38. Konrad, J. M. (1990a). Minimum undrained strength of two sands. *J. Geotech. Engrg., ASCE*, 116(6), 932-947.
39. Konrad, J. M. (1990b). Minimum undrained strength versus steady-state strength of sands. *J. Geotech. Engrg., ASCE*, 116(6), 948-963.
40. Konrad, J. M. (1993). Undrained response of loosely compacted sands during monotonic and cyclic compression test. *Géotechnique* 43, No. 1, 69-89.
41. Kramer, K.L. (1988). Triggering of liquefaction flow slides in coastal soil deposits. *Engrg. Geol.* 26. 17-31.
42. Kramer, K. L. & H. B. Seed (1988). Initiation of soil liquefaction under static loading conditions. *J. Geotech. Engrg.*, 114: 412-430.

43. Kramer, K.L. (1989). Uncertainty in steady-state liquefaction evaluation procedure. *Journal of Geotechnical Engineering*, ASCE, Vol.115, No. 10, pp.1402-1419.
44. Kubota, T. (1997). *An experimental study on the mechanism of liquefied landslides*. MS Thesis, Nagoya University, Japan.
45. Kokusho, T. (1999). Water film in liquefaction sand and its effect on lateral spread. *Journal of Geotechnical and Geoenvironmental Engineering*, ASCE, Vol.125, No. 10, pp.817-826.
46. Lade, P. V., Yamamura, J. A., and Bopp, P. A. (1996): Significance of particle crushing in granular materials. *Journal of Geotechnical Engineering*, ASCE, Vol.122, No.4, pp. 309-316.
47. Lucia, P. C. (1981). *Review of Experiences with Flow Failures of Tailings Dams and Waste Impoundments*. Ph.D. Thesis, University of California, Berkeley.
48. Marui, H. (1996). Preliminary report on the Gamahara torrent debris flow of 6 December 1996, Japan. *Jour. Natural Disaster Science*. 18, 89-97.
49. Miyagi, T., Furuya, T., Umemura, J., Chiba, N., Marui, H., Chigira, M., 1998. Prompt report on the disaster triggered by heavy rainfall in southern Fukushima Prefecture, August 1998. *Journal of Japan Landslide Society* 35(2), 91-98 (in Japanese).
50. Negussey, D., Wijewickreme, W. K. D., and Vaid, Y. P. (1988). Constant volume friction angle of granular materials. *Can. Geotech. J.* Vol. 25, pp. 50-55.
51. OVANDO-SHELLEY, E., and B. E. PEREZ. (1997). Undrained behaviour of clayey sands in load controlled triaxial tests. *Géotechnique* 47, No. 1, 97-111.

52. Pitman, T. D., Robertson, P. K., and Segoo, D. C. (1994). Influence of fines on the collapse of loose sands. *Can. Geotech. J.* Vol. 31, pp. 728-739.
53. Poulos, S. J. (1981). The steady state of deformation. *J. Geotech. Engng Div. ASCE* 107, No. GT5, 553-562.
54. Poulos, S. J., Castro, G. & France, J. W. (1985). Liquefaction evaluation procedure. *J. Geotech. Engng. Div. ASCE* 111, No. 6, 772-792.
55. Reynolds, O. (1885). The dilating of media composed of rigid particles in contact. *Philosophical Magazine*, S. 5, Vol. 20, No. 127, pp. 469-481, London.
56. Roscoe, K. H., and Scholfield, A. N. (1958). On the yielding of soils. *Géotechnique*, Vol. 7, pp. 25-53.
57. Sasitharan, S., Robertson, P. K., Segoo, D. C., and Morgenstern, N. R. (1994). State-boundary surface for very loose sand and its practical implications. *Can. Geotech. J.* Vol. 31, pp. 321-334.
58. Sassa, K. (1984). The mechanism starting liquefied landslides and debris flows. *Proc. 4th Int'l. Symp. on Landslides*, Toronto, Canada, 2, 349-354.
59. Sassa, K. (1985). The mechanism of debris flows. *Proc., XI Int'l. Conf. Soil Mech. Found. Engrg.*, San Francisco, 3, 1173-1176.
60. Sassa, K., M. Kaibori and N. Kitera (1985). Liquefaction and undrained shear of torrent deposits as the cause of debris flows. *Proc. International Symposium on Erosion, Debris Flows and Disaster Prevention*, Tsukuba, pp.231-236.
61. Sassa, K. (1986). The mechanism of debris flows and the forest effect on their prevention. *Proc. 18th IUFRO World Congress*, Div.1, Vol.1, pp.227-238.

62. Sassa, K. (1988a). *Motion of Landslides and Debris Flows-Prediction of hazard area-*. Report for Grant-in-Aid for Scientific Research by Japanese Ministry on Education, Science and Culture (Project No. 61480062), pp.15.
63. Sassa, K. (1988b). Geotechnical model for the motion of landslides. Special Lecture of 5th International Symposium on Landslides, "*Landslides*", 1. Rotterdam: Balkema. 37-55
64. Sassa, K. (1989): Geotechnical classification of landslides. *Landslide News* No.3, pp.21-24.
65. Sassa, K., Fukuoka, H., Vibert, C. (1989). A new high-speed high-stress ring shear apparatus and the undrained shear strength during motion, *Proceedings of the Japan-China Symposium on Landslides and Debris Flows*, Niigata and Tokyo, pp. 93-97.
66. Sassa, K. (1992): Keynote lecture: Access to the dynamics of landslides during earthquakes by a new cyclic loading high-speed ring shear apparatus. Proc. of the 6th International Symposium on Landslides, In "*Landslides*" Balkema, Vol.3, pp.1919-1938.
67. Sassa, K. (1994): *Development of a new cyclic loading ring shear apparatus to study earthquake-induced-landslides*, Report for Grant-in-Aid for Developmental Scientific Research by the Ministry on Education, Science and Culture, Japan (Project No. 03556021), pp.1-106.
68. Sassa, K., H. Fukuoka, S. Evans, G. Furuya, D. Vanikov, D. X. Zhang and K. Araiba. (1995): *Rapid landslide triggered by the "Hyogoken-Nanbu earthquake" in Nishinomiya City, Hyogo Prefecture*, Report for Grant-in-Aid

- for Scientific Research by the Ministry on Education, Science and Culture, Japan (Project No.06306022), pp.244-258 (in Japanese).
69. Sassa, K. (1995). Keynote Lecture: Access to the dynamics of landslides during earthquakes by a new cyclic loading high-speed ring shear apparatus. Proc. 6th International Symposium on Landslides, "*Landslides*", Vol. 1, Balkema Ltd., pp. 115-132.
70. Sassa, K. & H. Fukuoka. (1995). Prediction of rapid landslide motion. *Proc. XX IUFRO World Cong.*, Finland.
71. Sassa, K. (1996). Prediction of earthquake induced landslides. Special Lecture of 7th International Symposium on Landslides, "*Landslides*", Rotterdam: Balkema, 1, 115-132.
72. Sassa, K., Fukuoka, H., Scarascia-Mugnozza, G. & S. Evans (1996). Earthquake-induced-landslides: Distribution, motion and mechanisms. Special Issue for the great Hanshin Earthquake Disaster, *Soils and Foundations*, 53-64.
73. Sassa, K. (1997). A new intelligent type of dynamic loading ring-shear apparatus. *Landslide News*. No.10, pp.33.
74. Sassa, K., H. Fukuoka, and F. W. Wang. (1997a). A geotechnical simulation test on the Gamahara torrent debris flow with ring shear apparatus (in Japanese). *Journal of the Earth*, Vol.19, No.10, pp.645-651.
75. Sassa, K., Fukuoka, H. and Wang, F. W. (1997b). Mechanism and risk assessment of landslide-triggered-debris flows: Lesson from the 1996.12.6 Otari debris flow disaster, Nagano, Japan. *Landslide Risk Assessment* (ed. Cruden and Fell), *Proceedings of the Int'l Workshop on Landslide Risk Assessment*, 347-356.

Rotterdam: Balkema.

76. Sassa, K. (1998a). Recent urban landslide disasters in Japan and their mechanisms. *Proc. 2nd International Conference on Environmental Management, "Environmental Management"*, Rotterdam: Balkema, 1, 47-58.
77. Sassa, K. (1998b). Mechanisms of Landslide Triggered Debris Flows. *Environmental Forest Science, Proc. of IUFRO Division 8 Conference*, pp. 499-518.
78. Sassa, K. (1998c). Mechanisms of landslide triggered debris flow. In "Environmental Forest Science" (edited by K. Sassa), Proceedings of IUFRO Div. 8 Conference, Kyoto, Kluwer Academic Publisher, 471-490.
79. Sassa, K., Fukuoka, H. and Wang, F. W. (1998). Mechanism of Rapid Long Runout Motion in the may 1997 Sumikawa Reactivated Landslide in Akita Prefecture and the July 1997 Harihara Landslide-Debris Flow, Kagoshima Prefecture, Japan. *Journal of Japan Landslide Society*, Vol. 32, no. 2, pp. 29-37.
80. Sassa, K. (1999). Introduction. In *Landslides of the World* (Sassa K. eds), Japan Landslide Society, Kyoto University Press, IX-XXIV.
81. Seed, H.B. (1968). Landslides during earthquakes due to soil liquefaction. *Journal Soil Mechanics Foundations Division, ASCE*, 94, No. 5, 1055-1122.
82. Seed, H. B. (1966). A Method for Earthquake Resistant Design of Earth Dams. *J. Geotech. Engrg Div. ASCE*, Vol. 92, No. SM1, Proc. Paper 4616, pp. 13-41.
83. Seed, H. B. (1979). Soil liquefaction and cyclic mobility evaluation for level ground during earthquakes. *J. Geotech. Engrg Div. ASCE*, 105, 201-255.

84. Seed, H. B., and Hon, M. (1987). Design problems in soil liquefaction. *J. Geotech. Engrg.*, ASCE, 113(8), 827-845.
85. Shoaei, Z. and Sassa, K. (1994). Basic study on the shear behaviour of landslides during earthquakes: Excess pore pressure generation in the undrained cyclic loading ring shear tests. *Bulletin of the disaster Prevention Research Institute, Kyoto University*, Vol. 44, part 1, pp.1-44.
86. Sitar, N., Anderson, S. A., and Johnson, K. A. (1992). Conditions leading to the initiation of rainfall-induced debris flows. *Geotech. Engrg. Div. Specially Conf.: Stability and Perf. of slopes and Embankments- II*, ASCE, New York, N. Y., pp. 834-839.
87. Skempton, A. W. (1954). The pore-pressure coefficient A and B. *Géotechnique* 4, No. 4, 143-147.
88. Sladen, J. A., D'Hollander, R. D. & Krahn, J. (1985). The liquefaction of sands, a collapse surface approach. *Can. Geotech. J.* 22, 564-578.
89. Soroush, A. (1996). *Numerical analysis of static liquefaction*. PhD thesis. University of Alberta.
90. Spence, K. J. & Guymet, I. (1997). Small-scale laboratory flowslides. *Géotechnique* 47, No. 5, 915-932.
91. Suzuki, Y., Minami, N., Tsuchiya, S., Kitahara, A., Ohsaka, O., Shuin, Y. (1998). Report of sediment-related hazard caused by heavy rainfall in Fukushima Prefecture (prompt report), A case of "Taiyo-no-kuni Karamatsu-so" in Nishigo Village, Nishi-Shirakawa County. *Journal of the Japan Society of Erosion Control Engineering* 51 (4), 40-42 (in Japanese).

92. Terzaghi, K. (1925). *Erdbaumechanik auf Bodenphysikalischer Grundlage*, Vienna, Deuticke.
93. Terzaghi, K. (1950). *Mechanics of landslides*. Berkey Volume, New York, pp. 81-124.
94. Terzaghi, K. (1956). Varieties of submarine slope failures. *Proc. 8th Texas Conf. Soil Mech. Found. Engrg.*, 1-41.
95. The Japanese Geotechnical Society (1990). *Standard Methods for the Geotechnical Tests*, pp.43-115.
96. Thevanayagam, S. (1998). Effects of fines and confining stress on undrained shear strength of silty sands. *Journal of Geotechnical and Geoenvironmental Engineering, ASCE*, Vol. 124, No. 6, pp. 479-491.
97. Thevanayagam, S., Ravishankar, K., and Mohan, S. (1996). Steady state strength, relative density and fines content relationship for sands. *Transp. Res. Record* 1547, 61-67.
98. Tika, TH. E., and Hutchinson, J. N. (1999). Ring shear tests on soil from the Vaiont landslide slip surface. *Géotechnique*, Vol. 49, No. 1, pp. 59-74.
99. Tika, T. E., Vaughan, P. R., Lemos, L. J. L. J. (1996). Fast shearing of pre-existing shear zones in soil. *Géotechnique*, Vol. 46, No. 2, pp.197-223.
100. Turner, A. K., and Schuster, R. L. (1996). *Landslides: Investigation and mitigation*. National academy press, Washington, D. C.
101. Vaid, Y. P., and Chern, J. C. (1983). Effects of static shear on resistance to liquefaction. *Soils and Foundations*, Vol. 23, No. 1, pp. 47-60.

102. Vaid, Y. P., and Chern, J. C. (1985). Cyclic and monotonic undrained response of saturated sands. *In advances in the art of testing soils under cyclic conditions*. Edited by V. Khosla. ASCE, New York, pp. 120-147.
103. Vaid, Y. P., Chung, E. K. F., and Kuerbis, R. H. (1989). Stress path and steady state. *Can. Geotech. J.* Vol. 27, pp. 1-7.
104. Vankov D.A., and Sassa, K. (1998). Dynamic testing of soils by ring-shear apparatus. *Proc. 8th Congr. of the Int'l Assoc. Engrg. Geol. and the Environ.*, Vancouver, Canada. Rotterdam: Balkema, Vol.1, pp485-492.
105. Varnes, D. J. (1978): Slope movement types and processes. *In special report 176: Landslides: Analysis and control* (R. L. Schuster and R. J. Krizek, eds.), Transportation Research Board, Washington, D. C., pp.11-33.
106. Wang, F. W. 1998. *An experimental study on grain crushing and excess pore pressure generation during-shearing of sandy soils-A key factor for rapid landslide motion*. PhD Thesis. Kyoto University.
107. Yoshimi, Y., Richart, F.E., Prakash, S., Balkan, D. D. & Ilyichev, V. A. (1977). Soil dynamics and its application to foundation engineering. *Proc., 9th Int. Conf. Soil Mech.* 2, 605-650.
108. Zeng, X. and Arulanandan, K. "Modeling the Lateral Sliding of a Slope due to Liquefaction of a Sand layer," *Journal of Geotechnical Engineering*, ASCE, Vol. 121, No.11, 814-817, 1995.
109. Zlatovic, S. and Ishihara, K. (1995). On the influence of nonplastic fines on residual strength. *Proc., IS-TOKYO'95, 1st Int. Conf. on Earthquake Geotech. Engrg.*, K. Ishihara, ed., A. A. Balkema, Rotterdam, The Netherlands, 239-244.

CAPTIONS AND LIST OF SYMBOLS

1. CAPTIONS

Table 4.1a Summary of the ring shear tests data for S7 (Note: see that below **Table 4.1c**).

Table 4.1b Summary of the ring shear tests data for S8 (Note: see that below **Table 4.1c**).

Table 4.1c Summary of the ring shear tests data for M10, M20, and M30.

Table 5.1 Summary of the flume tests data

Figure 2.1 Description of critical void ratio concept introduced by Casagrande.

- (a): variation of void ratio along with shear stress for sands at loose and dense state (after Casagrande, 1936);
- (b): critical void ratio line in void ratio-effective confining plane (after Casagrande, 1936);
- (c): Results of simple shear tests on 1 mm steel balls with a normal stress equal to 20 lb/sq in. (after Roscoe and Schofield, 1958).

Figure 2.2 Effective stress paths for undrained triaxial tests.

(SSL: Steady state line; σ' : Effective normal stress; τ : shear stress.)

Figure 2.3 Stress path and illustration of mass liquefaction and sliding surface liquefaction (After Sassa et al. 1996).

(a): mass liquefaction; (b): sliding surface liquefaction.

Figure 2.4 The steady state line (SSL) (after Soroush, 1996).

Figure 2.5 Collapse line (after Sladen et al., 1985).

Figure 2.6 Shear stress-axial strain curve in triaxial test.

(τ_f : shear stress at failure; τ_r : residual shear strength; τ_i : initial shear stress)

Figure 2.7 Shear stress-shear displacement curve in ring shear test.

(τ_f : shear stress at failure; τ_r : residual shear strength; τ_i : initial shear stress; R_L : static liquefaction resistance; I_B : brittleness index)

Figure 2.8 Varnes landslide movement scale and proposed landslide velocity scale (after Turner and Schuster, 1996).

Figure 2.9 Velocity distribution for slide and flow.

Figure 2.10 Definition of apparent friction angle.

(a): Definition of apparent friction angle for a landslide;

(b): Definition of apparent friction angle in ring shear test.

Figure 3.1 Grain size distribution curves for silica sand no. 7, no. 8 and loess.

Figure 3.2 Ring shear apparatus (DPRI-Ver.6).

(a): Photograph of ring shear apparatus DPRI-Ver.6;

(b): Control system of ring shear apparatus DPRI-Ver.6;

(c): Schematic diagram of ring shear apparatus DPRI-Ver.6;

- (d): Annular ring-shaped sample in ring shear box;
- (e): Close-up diagram of the edges and the pore pressure measurements.

Figure 3.3 Arrangement of flume test apparatus.

Figure 3.4 Arrangement of apparatus to measure pore pressure in moving saturated soils (after Sassa, 1988).

Figure 4.1 Ring shear test on loose sand showing mass liquefaction phenomenon.

(Test: S8_{r,6}; B_D=0.99, D_r= 63.3%; SSP: Steady State Point.)

- (a): Variation of pore pressure and shear resistance in relation to shear displacement;
- (b): Effective stress path.

Figure 4.2 Ring shear test on dense sand showing sliding surface liquefaction

(Test: S8_{r,7}; B_D=0.99, D_r= 95.2%, $\sigma = 196$ kPa, PTP: Phase Transformation; SSP: Steady State Point; F: Failure Point; E: Ending of the test).

- (a): Variation of pore pressure and shear resistance in relation to shear displacement;
- (b): Effective stress path.

Figure 4.3 Results of tests on S8 at different initial normal stresses.

(Tests: S8_{r,6}, S8_{r,16}, S8_{r,17}, S8_{r,18}; D_r = 63.3%; SSP: Steady State Point).

Figure 4.4 Results of tests on samples at different initial shear stresses.

(Tests: S8_{r,21}, S8_{r,22}, S8_{r,23}, S8_{r,25}; D_r = 68.2%–69.4%; SSP: Steady State Point).

- (a) Effective stress paths;
- (b) Variation of shear resistance in relation to shear displacement.

Figure 4.5 Comparison of the results of tests on S7 and S8 in loose state.

(Tests: S8_{r,6}, S7_{r,11}, S7_{r,15}; D_r = 63.3% for S8_{r,6}; D_r = 47.2% and 57.9 % for S7_{r,11} and S7_{r,15}, respectively).

- (a): Variation of shear resistances in relation to shear displacement;

- (b): Variation of pore pressures in relation to shear displacement;
- (c): Effective stress paths.

Figure 4.6 Typical test results for dense S7 and S8.

(Tests: S8_{r,7}, S7_{r,7}; $D_r = 88.3\%$ for S7_{r,7}; $D_r = 95.2\%$ for S8_{r,7})

- (a): Shear resistance versus shear displacement;
- (b): Pore pressures versus shear displacement;
- (c): Effective stress paths.

Figure 4.7 Comparison on the results of tests on loose M10, M20, and M30.

(Tests: M10_{r,6}, M20_{r,5}, M30_{r,5}; $D_r = 52.6\%$, 63.3% , and 67.5% for M10, M20, and M30, respectively)

- (a): Variation of shear resistance in relation to shear displacement;
- (b): Variation of pore pressure in relation to shear displacement;
- (c): Effective stress paths.

Figure 4.8 Comparison on the results of tests on dense M10, M20, and M30.

(Tests: M10_{r,4}, M20_{r,4}, M30_{r,1}; $D_r = 70.4\%$, 79.4% , and 80.5% for M10, M20, and M30, respectively; PT: Phase transformation)

- (a): Variation of shear resistance in relation to shear displacement;
- (b): Variation of pore pressure in relation to shear displacement;
- (c): Effective stress paths.

Figure 4.9 Ring shear test on loose sand showing mass liquefaction phenomenon.

(Test S8_{r,6} and its complementary test; $B_D=0.99$, $D_r=63.3\%$, $\sigma = 196$ kPa, SSP: Steady State Point.).

- (a): Variation of pore pressure and shear resistance in relation to shear displacement for the host test;
- (b): Variation of pore pressure and shear resistance in relation to shear displacement for the complementary test;

(c): Effective stress paths.

Figure 4.10 Shear deformation of vertically inserted slice of Toyoura sand after 3-cm shear for the complementary test on Test S8_{r,6} (showing mass liquefaction).

Figure 4.11 Ring shear test on dense sand showing sliding surface liquefaction phenomenon.

(Test S8_{r,7} and its complementary test; $B_D = 0.99$, $D_r = 95.2\%$ and 94.9% for the host test and complementary test on dense S8, respectively; SSP: Steady State Point).

(a): Variation of pore pressure and shear resistance in relation to shear displacement for the host test;

(b): Variation of pore pressure and shear resistance in relation to shear displacement for the complementary test;

(c): Effective stress paths.

Figure 4.12 Shear deformation of vertically inserted slice of Toyoura sand after 3-cm shear in the complementary test showing sliding surface liquefaction for test S8_{r,7} ($B_D = 0.99$; $D_r = 94.9\%$).

Figure 4.13 Formation of shear zone in the test on loose S8 showing mass liquefaction (Test S8_{r,6}; $B_D = 0.99$; $D_r = 63.3\%$).

Figure 4.14 Grain-size distribution curves for the original sample and that taken from the shear zone after test on loose S8 showing mass liquefaction.

(Test S8_{r,6}; $B_D = 0.99$; $D_r = 63.3\%$; shear displacement: 10 m).

Figure 4.15 Grain-size distribution curves for the original sample and that taken from the shear zone after test on dense S8 showing sliding surface liquefaction.

(Test S8_{r,7}; $B_D = 0.99$; $D_r = 95.2\%$; shear displacement: 210 m).

Figure 4.16 Formation of shear zone in the test on dense S8 showing sliding surface

liquefaction.

(Test S8_{r,7}; $B_D = 0.99$; $D_r = 95.2\%$; shear displacement: 210 m).

Figure 4.17 Results of tests on loose S7 at different initial normal stresses for two different test series.

(a): Effective stress paths for the tests with D_r being approximately 47.2% (S7_{r,10}; S7_{r,11}; S7_{r,12}; S7_{r,13});

(b): Effective stress paths for the tests with D_r being approximately 56.6% (S7_{r,14}; S7_{r,15}; S7_{r,16}; S7_{r,17}).

Figure 4.18 Brittleness indexes at different initial stress states.

(a) Variation of brittleness index in relation to initial normal stress (S8_{r,6}, S8_{r,16}, S8_{r,17}, S8_{r,18});

(b) Variation of brittleness index in relation to initial shear stress (S8_{r,6}, S8_{r,16}, S8_{r,17}, S8_{r,18}).

Figure 4.19 Variation of generated pore pressure in relation to relative density during different undrained shear periods for S7 and S8.

(a): Generated pore pressure during Stage 1 due to the failure of metal stable soil structure and orientation of grains;

(b): Generated pore pressure during Stage 2 due to the dilatancy of dense sand accompanying the further shearing;

(c): Generated pore pressure during Stage 3 due to grain crushing accompanying the shear displacement.

Figure 4.20 D_r versus peak shear strength.

(a) For the tests on S7 and S8;

(b) For the tests on M10, M20, and M30.

Figure 4.21 Ring shear test data for S7 and S8 at steady state.

(a): D_r versus $\log(\tau_s)$; (b): D_r versus $\log(\sigma_s')$.

Figure 4.22 Ring shear test data for M10, M20, and M30 at steady state.

(a): D_r versus $\log(\tau_s)$; (b): D_r versus $\log(\sigma_s')$.

Figure 4.23 Recovering of shear resistance due to excess pore pressure dissipation from the shear zone.

Figure 5.1 Time series of pore pressure and sliding distance for test $S8_{N,8}$.

(Sample: silica sand no. 8; Capacities of linear-displacement transducer and laser-displacement sensor are 100 cm and 15 mm, respectively; the displacements greater than the capacities were not determined.)

(a): Time series of pore pressure and sliding distance immediately before and after the failure.

(b): An enlargement of Figure 5.1a during the very short period of failure.

Figure 5.2 Summarized failure modes.

Figure 5.3 Variation of shear displacement, sliding distance and sliding velocity for test $S8_{I,8}$.

Figure 5.4 Variation of sliding velocity in relation to sliding distance ($S8_{I,8}$).

S3: Beginning of Stage 3

Figure 5.5 Relationship between excess pore pressure and initial density index.

Figure 5.6 Variation of sliding velocity for samples with different initial density indexes.

(a): for tests with initial density index $I_d \leq 0.22$ ($S8_{I,5}$, $S8_{I,6}$, $S8_{I,8}$, $S8_{I,12}$);

(b): for tests with initial density index $I_d \geq 0.22$ ($S8_{I,1}$, $S8_{I,2}$, $S8_{I,5}$).

Figure 5.7 Variation of sliding velocity in relation to sliding distance for samples with

different loess contents.

S8: Silica sand no. 8; M10: Mixture of silica sand no. 8 with 10 percent loess by weight; M20: Mixture of silica sand no. 8 with 20 percent loess by weight; M30: Mixture of silica sand no. 8 with 30 percent loess by weight.

Figure 5.8 Variation of pore pressure in relation to rotating velocity for the test on saturated S8.

Figure 5.9 Pore pressure during motion for test on saturated S8 in the form of floating ratio and pore pressure ratio.

Figure 5.10 Results of double cylinder mixing tests on S7, S8, M10, M20, and M30.

- (a): Variation of floating ratio against rotating velocity in the acceleration process;
- (b): Variation of floating ratio against rotating velocity in the deceleration process;
- (c): Variation of pore pressure ratio against rotating velocity in the acceleration process;
- (d): Variation of pore pressure ratio against rotating velocity in the deceleration process.

Figure 6.1 Location of the fluidized landslides.

Figure 6.2 The Hiegaesi landslide triggered by the August 1998 heavy rainfall depositing in a paddy field in Hiegaesi of Otakura, Nishigo Village (photograph courtesy of M. Chigira).

Figure 6.3 Plane sketch and longitudinal section of the landslide based on field survey (S1, S2 and S3: sampling points; P: observation pit).

- (a): Sketch of plane shape;
- (b): Central longitudinal section.

Figure 6.4 Source area of the Hiegaesi landslide (a yellow bond over the dacite tuff is

pumice layer).

Figure 6.5 Bamboo grasses in front of the source area brought down by landslide are keeping alive.

Figure 6.6 A close-up photograph in the observation pit (S1, S2: sampling points).

Figure 6.7 Grain-size distribution of sample S1 and S2.

Figure 6.8 The undrained ring shear test results on soils (sample S3) taken from the source area (Shear speed = 2 mm/sec, $B_D = 0.98$, $e = 1.93$).

- (a) Variation of normal stress, pore pressure and shear resistance with shear displacement;
- (b) Effective stress path (ESP) and Total stress path (TSP).

Figure 6.9 Grain-size distributions of sample S3 and that after sheared for 6.5 m in the drained condition.

Figure 6.10 The drained ring shear test results on soils (sample S3) taken from the source area (Loading rate = 0.1 kPa/sec, $B_D = 0.98$, $e = 1.82$).

- (a) Variation of normal stress, shear resistance and sample height;
- (b) Variation of shear displacement;
- (c) Effective stress path.

Figure 6.11 Schematic diagrams of sample preparation of rice plants and the soil from the landslide mass in ring shear box.

- (a) A section in the central line of the shear box and the plane of it showing how to set the soil from paddy field and rice plants in the lower half of the shear box;
- (b) A section in the central line of the shear box showing how to bring-down the rice plants in the opposite direction to the shear direction at the shear surface, and set the soil from the landslide mass on it.

Figure 6.12 The ring shear test results on rice plants and soil from landslide mass (shear

speed = 2 mm/sec, $B_D = 0.55$).

- (a) Variation of normal stress, pore pressure and shear resistance with shear displacement;
- (b) Effective stress path (ESP) and Total stress path (TSP).

Figure 6.13 Recovering of shear resistance after shear box was switched to drained condition for the test on rice plants and soil.

Figure 6.14 Lower part of the shear box after the drained ring shear test.

- (a) Shear zone between rice plants and sliding soil mass. Pins show the border;
- (b) Scratch on the bottom of the sliding soil mass caused by the relative motion with rice plants in the drained condition.

2. LIST OF SYMBOLS

B_D : parameter of saturation in the direct shear state

D_{10} : effective grain size

D_{50} : Mean grain size

D_r : relative density

e : void ratio

e_{max} : maximum void ratio

e_{min} : minimum void ratio

U_c : uniformity coefficient

I_B : brittleness index

I_d : density index

I_{dm} : optimal density index for excess pore pressure generation

σ : normal stress

τ_f : undrained shear strength at failure (peak shear strength)

τ_r : residual shear strength

- τ_s : shear resistance at steady state
- σ_s' : effective normal stress at steady state
- σ_i : initial normal stress
- τ_i : initial shear stress
- R_L : static liquefaction resistance
- r_d : unit weight of dry sample
- r_f : floating ratio
- r_u : pore pressure ratio
- r_w : unit weight of water
- r_s : unit weight of saturated soil
- u_s : static water pressure
- u_m : observed peak value of pore pressure during failure of slope
- u_i : observed pore pressure before the failure of slope
- ϕ_m : apparent friction angle of a landslide.
- Δu : generated excess pore pressure during major failure process of rainfall-induced slope failure.
- ΔS : run-out distance of failed soil mass during the major failure process of rainfall-induced slope failure.
- G_s : specific gravity of sample
- V_p : the peak velocity of moving failed mass during the major failure.
- S7: silica sand no. 7
- S8: silica sand no. 8
- M10: mixture of silica sand with 10 percent loess by weight
- M20: mixture of silica sand with 20 percent loess by weight
- M30: mixture of silica sand with 30 percent loess by weight

Table 4.1a Summary of the ring-shear tests data for S7 (Note: see that below **Table 4.1c**).

Test	Sample	e	D _r %	σ _v kPa	τ ₁ kPa	τ ₁ kPa	τ ₂ kPa	σ' kPa	U ₁ kPa	U ₂ kPa	U ₃ kPa	R _L kPa	I _B	Φ _m degree
S7 _{r,1}		0.92	57.9	196		80.3	34.3	49.2	109.4	-35.2	75.3	79.3	0.57	9.9
S7 _{r,2}		0.93	56.8	196		70.4	29.0	46.8	116	-22.9	56.4	70.4	0.59	8.4
S7 _{r,3}		0.92	58.5	196		90.5	36.1	46.2	106	-48	97.2	90.5	0.60	10.4
S7 _{r,4}		0.94	54.7	196		55.7	*	*	123.7	-18.9	37.9	55.7	*	*
S7 _{r,5}		0.93	57.1	196		75.7	*	*	113.1	-30.0	49.4	75.7	*	*
S7 _{r,6}		0.81	79.9	196		184.6	58.5	87.7	66.1	-136.9	179.1	184.6	0.68	16.6
S7 _{r,7}		0.76	88.3	196		220.0	65.0	90.3	27	-144.6	193.3	220.0	0.70	18.3
S7 _{r,8}		0.87	68.8	196		168.4	46.5	77.3	86	-130.3	174.3	168.4	0.72	13.3
S7 _{r,9}	S7	0.82	76.9	196	0	188.6	51.7	75.2	38.4	-87.1	169.5	188.6	0.73	14.5
S7 _{r,10}		0.98	47.2	147		36.8	11.6	19.0	+	+	+	36.8	0.68	4.5
S7 _{r,11}		0.98	47.2	196		45.6	10.9	20.4	+	+	+	45.6	0.76	3.2
S7 _{r,12}		0.98	47.2	245		65.9	13.8	21.6	+	+	+	65.9	0.79	3.2
S7 _{r,13}		0.98	47.6	294		57.7	10.6	20.3	+	+	+	57.7	0.82	1.5
S7 _{r,14}		0.93	56.6	147		43.2	23.8	36.3	93.2	-15	30	43.2	0.45	9.2
S7 _{r,15}		0.93	56.6	196		55.6	24.6	38.1	123.6	-18.5	52.1	55.6	0.56	7.2
S7 _{r,16}		0.93	56.6	245		87.2	26.1	39.7	147.1	-29.2	88.3	87.2	0.70	6.1
S7 _{r,17}		0.93	56.6	294		94.7	25.3	36.3	188.1	-22.9	90	94.7	0.73	4.9

Table 4.1b Summary of the ring-shear tests data for S8 (Note: see that below Table 4.1c).

Test	Sample	e	D _r %	σ _i kPa	τ _i kPa	τ _r kPa	τ _s kPa	σ' kPa	U ₁ kPa	U ₂ kPa	U ₃ kPa	R _L kPa	I _B	φ _m degre e
S8 _{r,1}	S8	1.03	78.4	196	0	74.7	25.1	48.5	88.9	-7.9	67.2	74.7	0.66	7.3
S8 _{r,2}		1.05	75.7	196	0	57.6	27.1	40.2	102.7	-4.5	57.6	64.3	0.53	7.9
S8 _{r,3}		1.06	74.1	196	0	45.7	23.9	35.4	129.0	-6.0	40.1	45.7	0.48	7.0
S8 _{r,4}		1.04	76.0	196	0	63.4	30.4	46.5	103.5	-4.7	54.7	63.4	0.52	8.8
S8 _{r,5}		0.92	91.2	196	0	171.7	60.6	82.3	80.7	-117.1	152.3	171.7	0.65	17.2
S8 _{r,6}		1.15	63.3	196	0	53.5	15.2	28.3	+	+	+	53.5	0.72	4.4
S8 _{r,7}		0.89	95.2	196	0	210.2	33.5	47.9	61.9	-126.1	224.7	210.2	0.84	9.7
S8 _{r,8}		0.99	82.6	196	0	111.0	20.4	35.4	85	-47.6	125.1	111.0	0.82	5.9
S8 _{r,9}		1.00	81.1	196	94.5	100.4	30.4	45.1	+	+	+	5.9	0.70	8.8
S8 _{r,10}		1.07	72.7	196	100.6	105.7	24.7	41.3	+	+	+	5.1	0.77	7.2
S8 _{r,11}		1.10	68.4	196	26.4	61.5	23.1	33.6	+	+	+	35.1	0.62	6.7
S8 _{r,12}		1.09	69.9	196	59.9	73.1	22.0	29.9	+	+	+	13.2	0.70	6.4
S8 _{r,13}		1.07	72.3	196	73.3	85.9	28.7	37.8	+	+	+	12.6	0.67	8.3
S8 _{r,14}		1.16	61.5	196	56.8	84.3	16.1	21.6	+	+	+	27.5	0.81	4.7
S8 _{r,15}		0.91	92.5	196	0	193.9	*	*	+	+	+	193.9	*	*
S8 _{r,16}		1.15	63.3	294	0	71.5	15.9	29.8	+	+	+	71.5	0.78	3.1
S8 _{r,17}		1.15	63.3	147	0	36.7	14.8	20.2	+	+	+	36.7	0.60	5.7
S8 _{r,18}		1.15	63.3	245	0	61.4	15.7	27.7	+	+	+	61.4	0.75	3.6
S8 _{r,19}		1.08	71.7	196	105.6	136.8	26.6	37.4	+	+	+	31.2	0.81	7.7
S8 _{r,20}		1.08	71.7	196	86.5	105.6	*	*	+	+	+	19.1	*	*
S8 _{r,21}		1.10	69.0	196	34.6	68.3	21.3	28.9	+	+	+	33.7	0.69	6.2
S8 _{r,22}		1.10	69.1	196	71.8	85.9	19.7	30.1	+	+	+	14.1	0.77	5.7
S8 _{r,23}		1.10	69.4	196	109.4	117.3	22.2	28.3	+	+	+	7.9	0.81	6.5
S8 _{r,24}		1.05	75.3	196	80.3	104.7	29.1	41.4	+	+	+	24.4	0.72	8.4
S8 _{r,25}		1.11	68.2	196	0	51.4	22.5	38.9	+	+	+	51.4	0.56	6.5

Table 4.1c Summary of the ring-shear tests data for M10, M20, and M30.

Test	Sample	e	D _r %	σ _i kPa	τ _i kPa	τ _f kPa	τ _s kPa	σ' kPa	U ₁ kPa	U ₂ kPa	U ₃ kPa	R _L kPa	I _B	Φ _m degree
M10 _{r,1}	M10	1.13	48.5	147		30.1	4.6	11.7	+	+	+	30.1	0.85	1.8
M10 _{r,2}		1.13	48.5	98		19.2	4.9	11.9	+	+	+	19.2	0.74	2.9
M10 _{r,3}		1.10	52.1	196		48.0	19.3	31.0	+	+	+	48.0	0.60	5.6
M10 _{r,4}		0.96	70.4	196	0	112.3	37.7	56.3	85.1	-43.1	97.7	112.3	0.66	10.9
M10 _{r,5}		1.07	56.3	294		70.4	23.7	34.1	+	+	+	70.4	0.66	4.6
M10 _{r,6}		1.10	52.6	196		57.9	13.3	19.7	+	+	+	57.9	0.77	3.9
M10 _{r,7}		1.02	62.7	196		74.8	*	*	+	+	+	74.8	*	*
M20 _{r,1}	M20	1.06	58.5			49.0	6.6	13.2	+	+	+	49.0	0.87	1.9
M20 _{r,2}		0.97	70.1			55.8	9.5	14.0	+	+	+	55.8	0.83	2.8
M20 _{r,3}		0.94	73.0	196	0	61.3	11.3	16.0	116.7	-6.3	69.6	61.3	0.82	3.3
M20 _{r,4}		0.89	79.4			104.6	14.7	18.3	101.6	-35.9	112	104.6	0.86	4.3
M20 _{r,5}		1.02	63.3			51.8	12.4	20.6	+	+	+	51.8	0.76	3.6
M30 _{r,1}	M30	0.89	80.5			56.2	6.5	8.8	+	+	+	56.2	0.88	1.9
M30 _{r,2}		0.86	84.0			74.0	11.8	15.8	+	+	+	74.0	0.84	3.4
M30 _{r,3}		0.88	82.4	196	0	61.6	8.8	12.8	+	+	+	61.6	0.86	2.5
M30 _{r,4}		0.98	69.8			52.3	4.2	7.9	+	+	+	52.3	0.92	1.2
M30 _{r,5}		1.00	67.5			50.0	2.8	4.9	+	+	+	50.0	0.94	0.8

Note: The subscript r, such as in M10_{r,1}, means ring-shear test; S7, and S8: Silica sand no. 7 and no. 8, respectively; M10, M20, and M30: Mixture of silica sand no. 8 with 10%, 20%, and 30% loess by weight, respectively; e: Initial void ratio; D_r: Initial relative density; σ_i: Initial normal stress; τ_i: Initial shear stress; τ_f: Undrained shear strength at failure; τ_s: Undrained residual shear strength (usually undrained shear strength at steady state); σ' Effective normal stress at steady state; U₁, U₂, and U₃: Initiated pore pressure within Stage 1, Stage 2, and Stage 3 (shown in Figure 4.2a) respectively, for those tests shown sliding surface liquefaction; R_L: Static liquefaction resistance; I_B: Brittleness index; Φ_m: Apparent friction angle; *: Failed to shear to steady state due to water leakage in the final shear stage; +: Without re-hardening process that would result in minus pore pressure generation.

Table 5.1 Summary of the flume tests data

Test	Test series	Sample	G_s	e_{max}	e_{min}	e	I_d	Δu : kPa	ΔS : cm	V_p : cm/s
$S7_{I.1}$	I	S7	2.63	1.23	0.70	0.97	0.49	0.14	1.1	0.7
$S7_{I.2}$						1.01	0.41	0.03	*	*
$S7_{I.3}$						1.14	0.17	0.21	3.2	4.5
$S7_{I.4}$						1.22	0.01	0.72	8.3	14.5
$S7_{I.5}$						1.24	-0.06	0.54	5.3	10.6
$S7_{I.6}$						1.35	-0.23	0.23	*	*
$S7_{I.7}$						1.41	-0.34	0.32	5.5	7.6
$S7_{I.8}$						1.49	-0.49	0.17	8.2	9.5
$S7_{I.9}$						1.50	-0.51	0.18	2.3	7.3
$S8_{II.1}$	II	S8	2.63	1.66	0.85	1.29	0.46	0.10	13.4	4.1
$S8_{II.2}$						1.41	0.31	0.48	33.9	8.6
$S8_{II.3}$						1.46	0.25	0.53	*	*
$S8_{II.4}$						1.46	0.25	0.62	*	*
$S8_{II.5}$						1.48	0.22	1.01	81.2	36.8
$S8_{II.6}$						1.50	0.20	1.02	79.0	35.0
$S8_{II.7}$						1.51	0.19	0.99	29.6	8.5
$S8_{II.8}$						1.58	0.10	0.64	45.6	29.8
$S8_{II.9}$						1.68	-0.03	0.51	58.6	39.6
$S8_{II.10}$						1.70	-0.05	0.13	11.8	16.1
$S8_{II.11}$						1.71	-0.06	0.33	24.0	31.1
$S8_{II.12}$						1.77	-0.14	0.20	39.3	18.1
$M10_{III.1}$	III	M10	2.64	1.51	0.73	1.61	-0.13	0.55	90.7	59.3
$M20_{III.1}$		M20	2.65	1.52	0.73	1.50	0.01	0.54	>100	68.2
$M30_{III.1}$		M30	2.66	1.56	0.73	1.58	-0.02	0.58	>100	77.6

V_p : Peak value of velocity for each test; ΔS : Run-out distance during main failure; Δu : Generated excess pore pressure during main failure; *: Unable to measure distance, because the "Ball" of the distance measurement system in Figure 5.3 did not properly move with the soil.

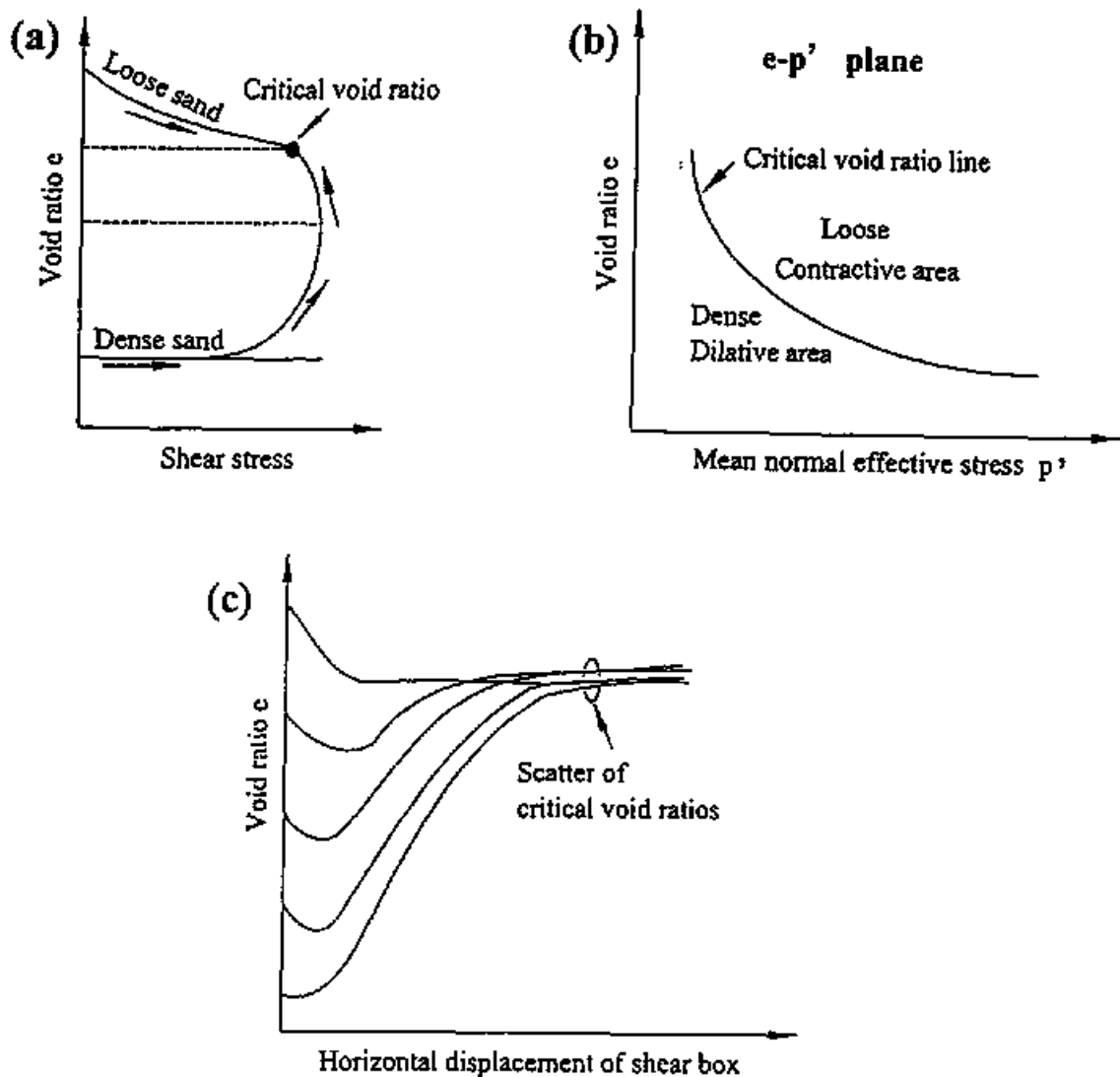


Figure 2.1 Description of critical void ratio concept introduced by Casagrande.

- (a): variation of void ratio along with shear stress for sands at loose and dense state (after Casagrande, 1936);
- (b): critical void ratio line in void ratio-effective confining plane (after Casagrande, 1936);
- (c): Results of simple shear tests on 1 mm steel balls with a normal stress equal to 20 lb/sq in. (after Roscoe and Schofield, 1958).

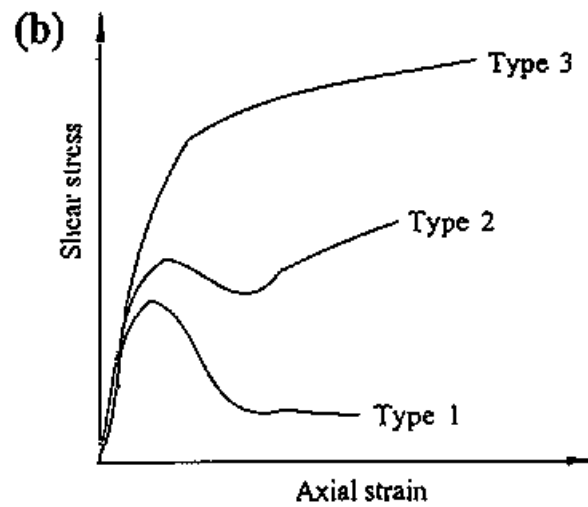
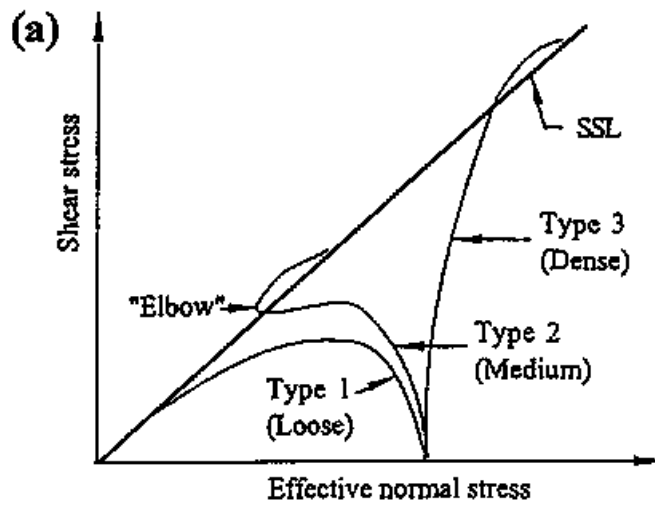
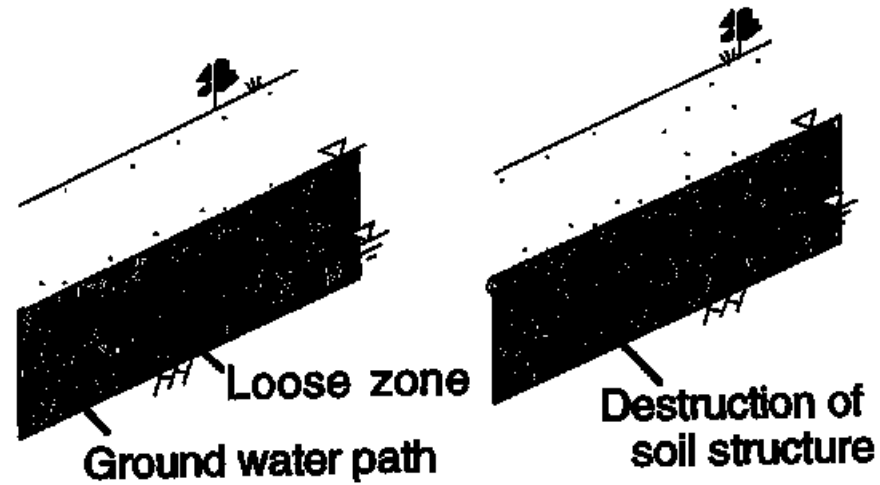
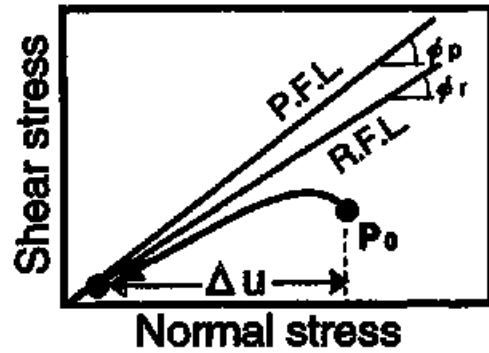


Figure 2.2 Effective stress paths for undrained triaxial tests.

(SSL: Steady state line; σ' : Effective normal stress; τ : shear stress)

A. (Mass) Liquefaction



B. Sliding surface liquefaction

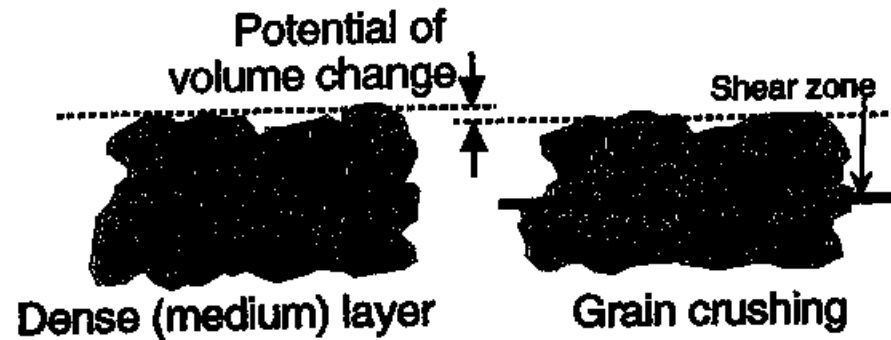
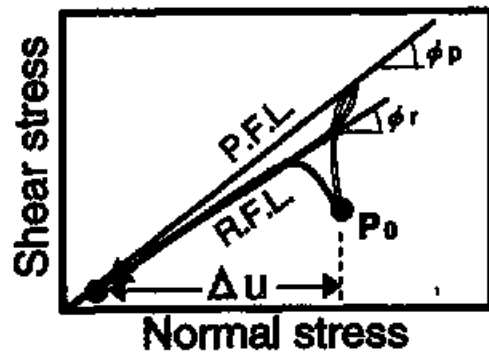


Figure 2.3 Stress path and illustration of mass liquefaction and sliding surface liquefaction (After Sassa et al. 1996).

(a): mass liquefaction; (b): sliding surface liquefaction.

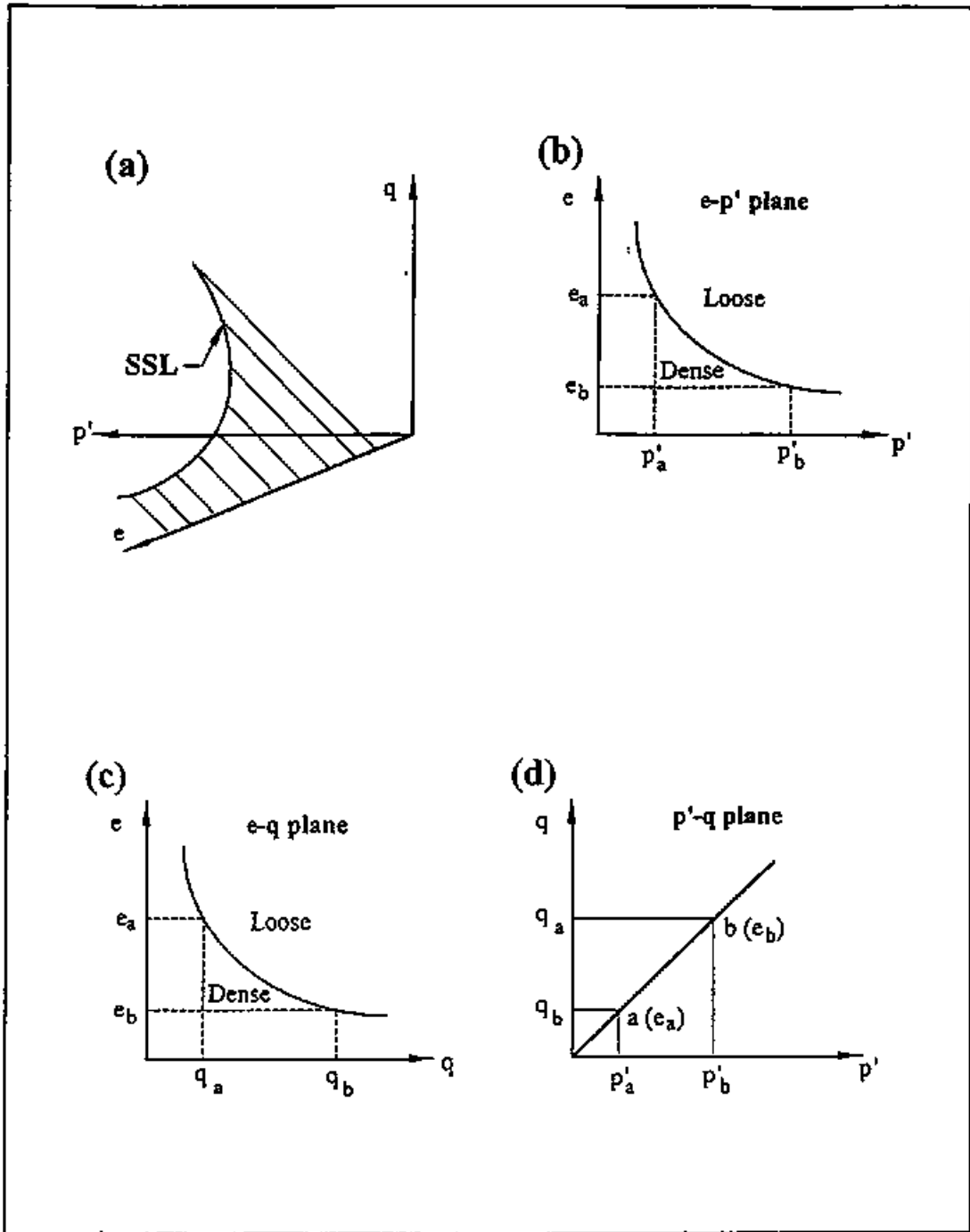


Figure 2.4 The steady state line (SSL) (after Soroush, 1996).

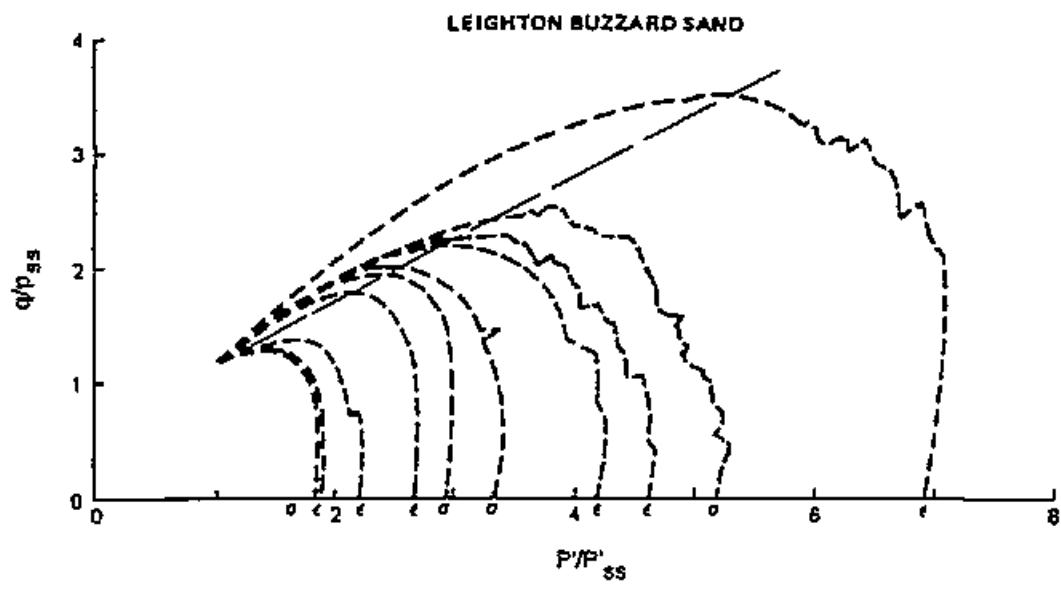


Figure 2.5 Collapse line (after Staden et al., 1985).

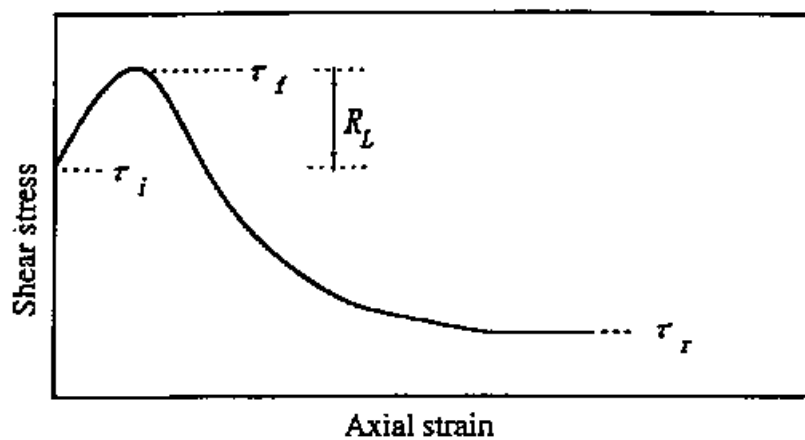


Figure 2.6 Shear stress-axial strain curve in triaxial test.

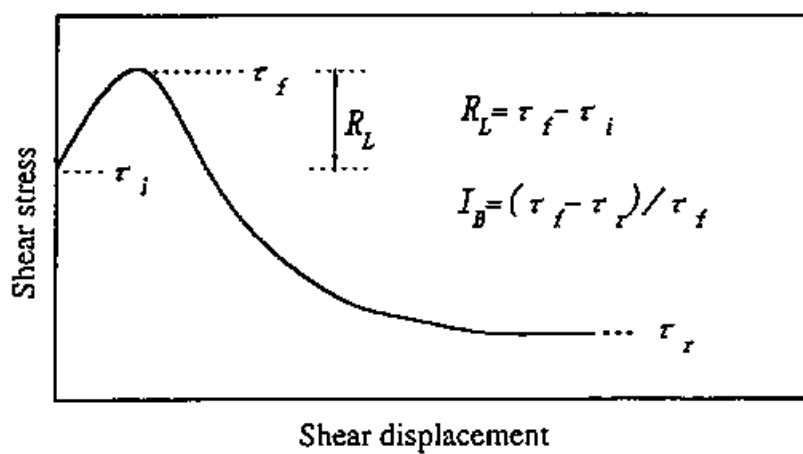
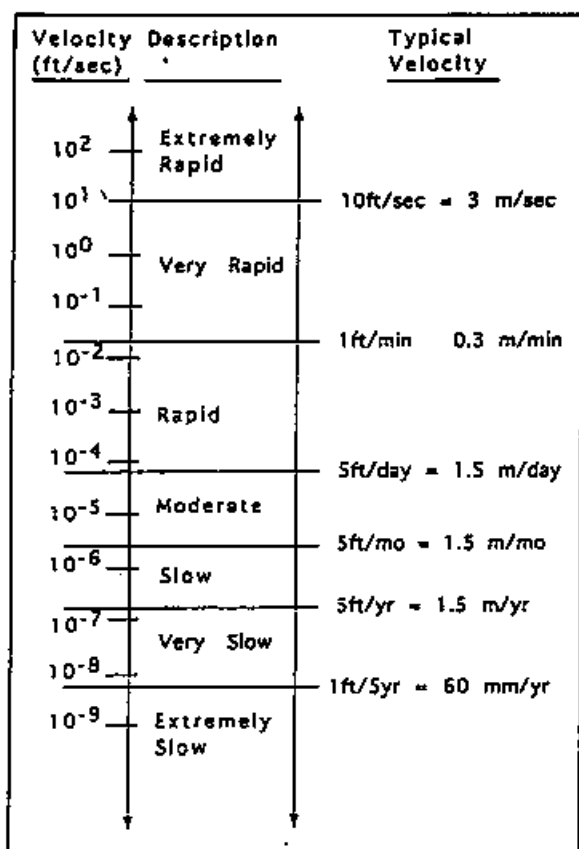
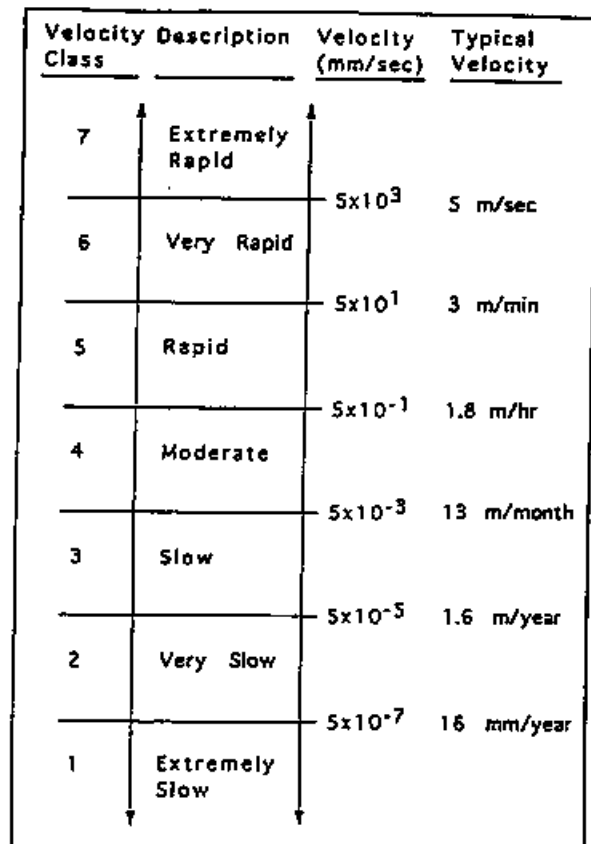


Figure 2.7 Shear stress-shear displacement curve in ring shear test.



(a)



(b)

Figure 2.8 Varnes landslide movement scale and proposed landslide velocity scale (after Turner and Schuster, 1996).

(a): Varnes landslide movement scale;

(b): Proposed landslide velocity scale.

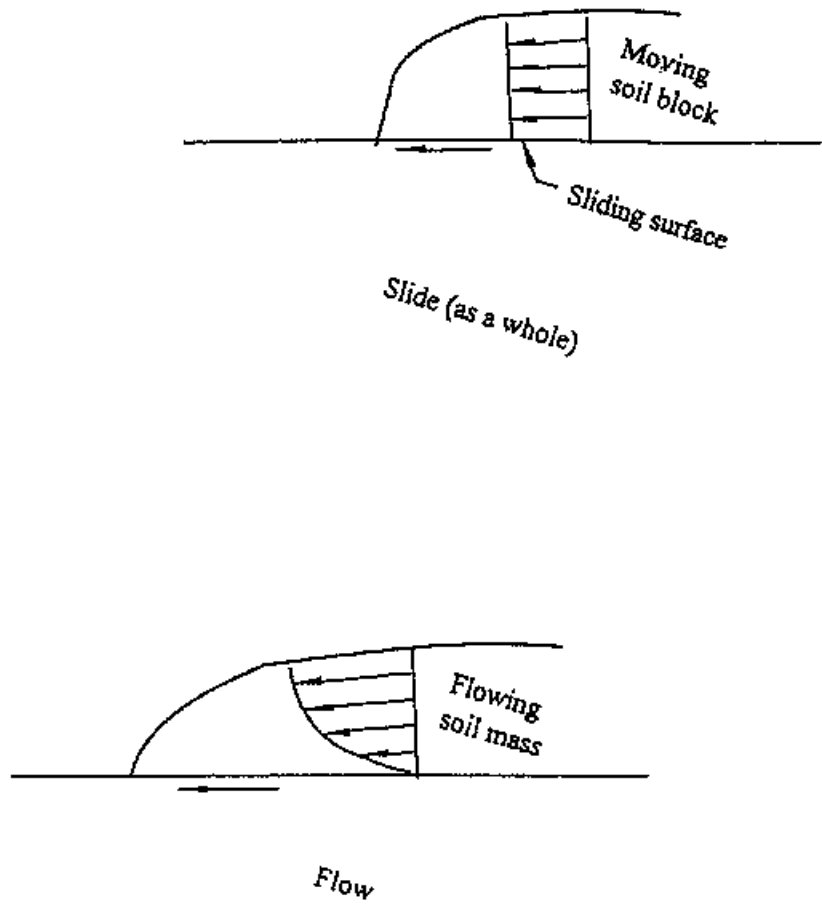


Figure 2.9 Velocity distribution for slide and flow

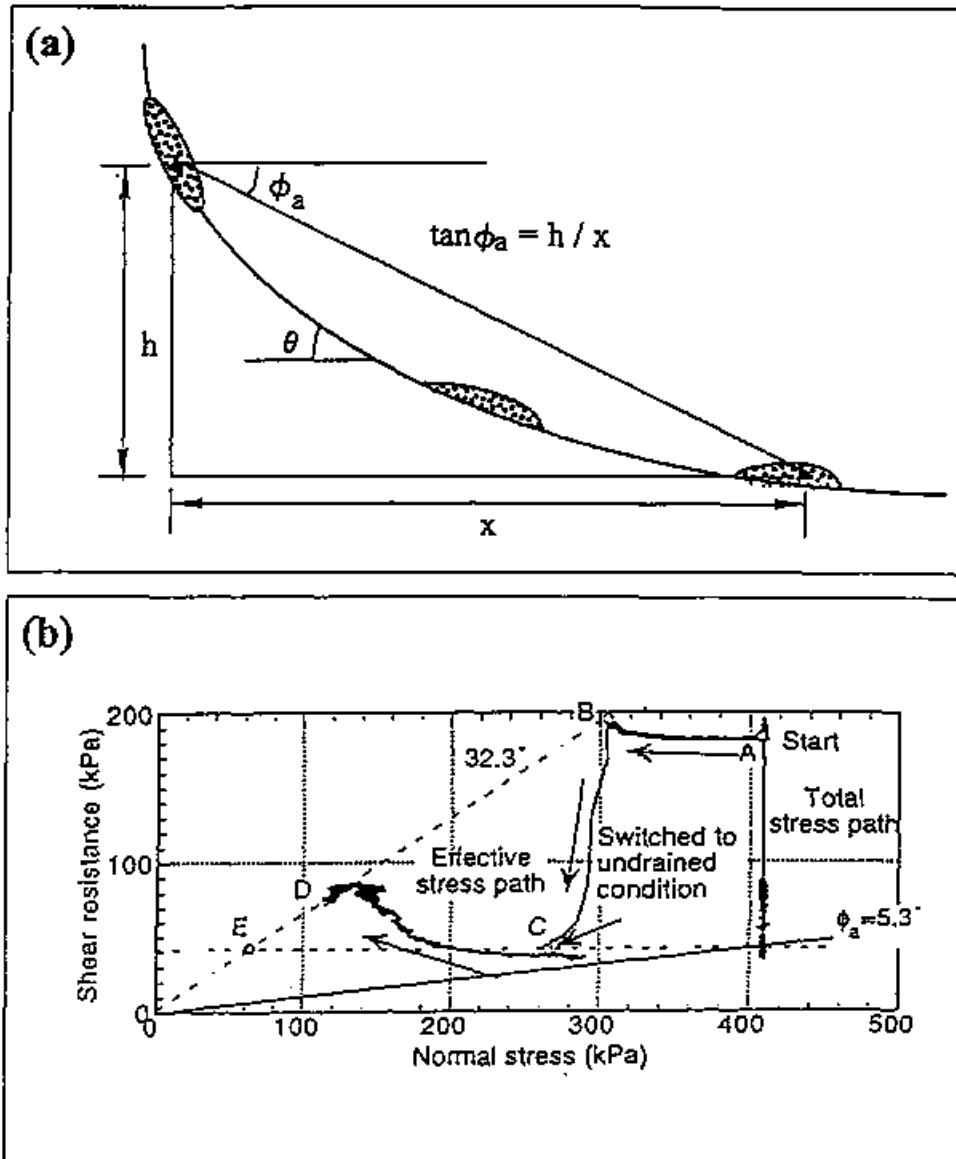


Figure 2.10 Definition of apparent friction angle.

(a): Definition of apparent friction angle for a landslide (after Sassa, 1985);

(b): Definition of apparent friction angle in ring-shear test (after Sassa et al. 1998).

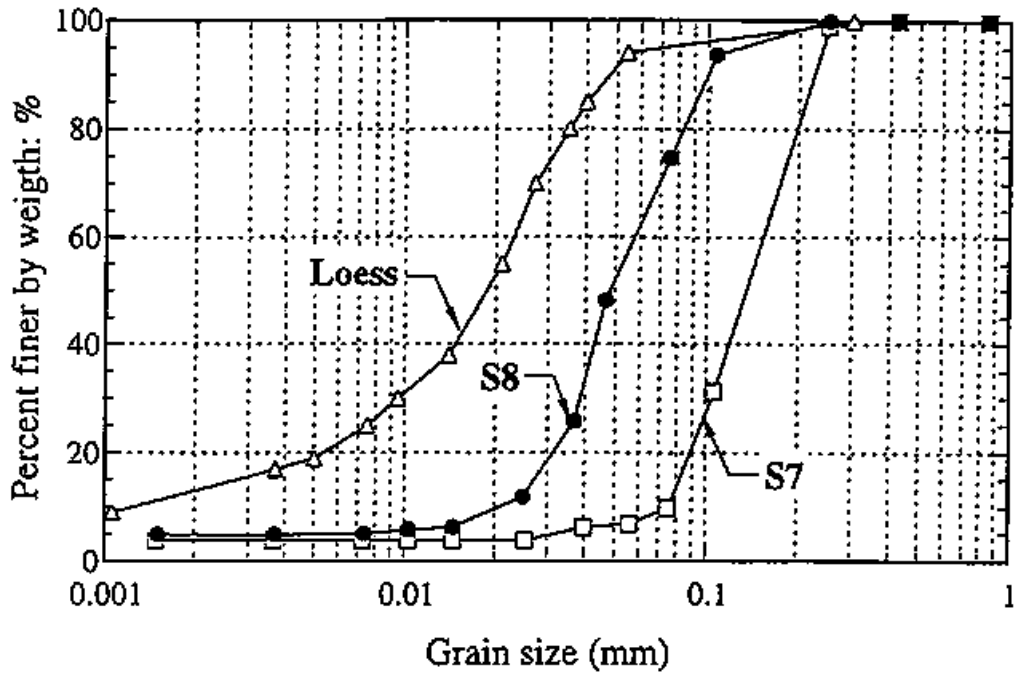


Figure 3.1 Grain-size distribution of silica sand no. 7, silica sand no. 8 and loess. (S7: Silica sand no. 7; S8: silica sand no. 8)

(a)

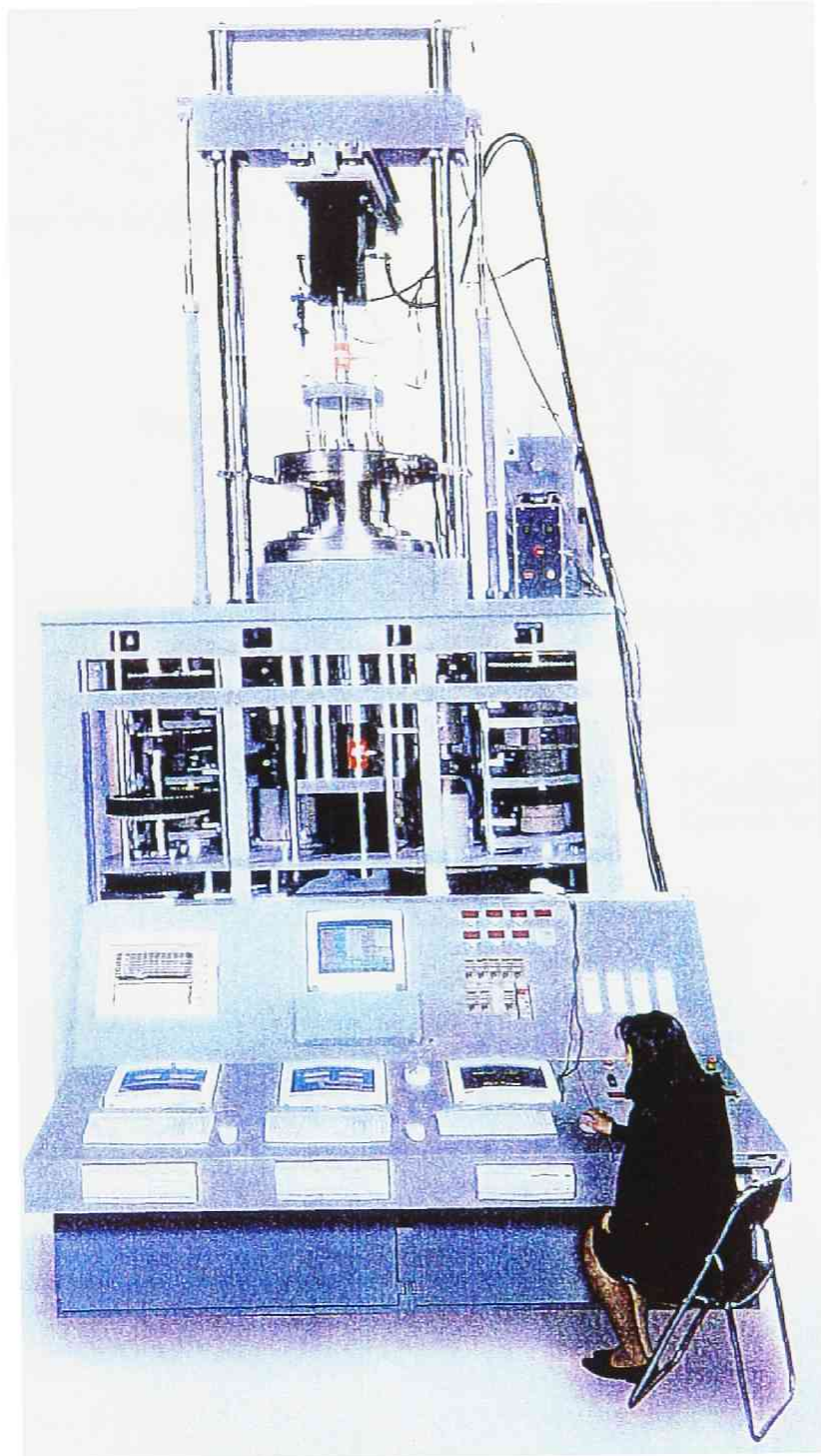


Figure 3.2 Ring shear apparatus (DPRI-Ver.6).

(a): Photograph of ring shear apparatus DPRI-Ver.6;

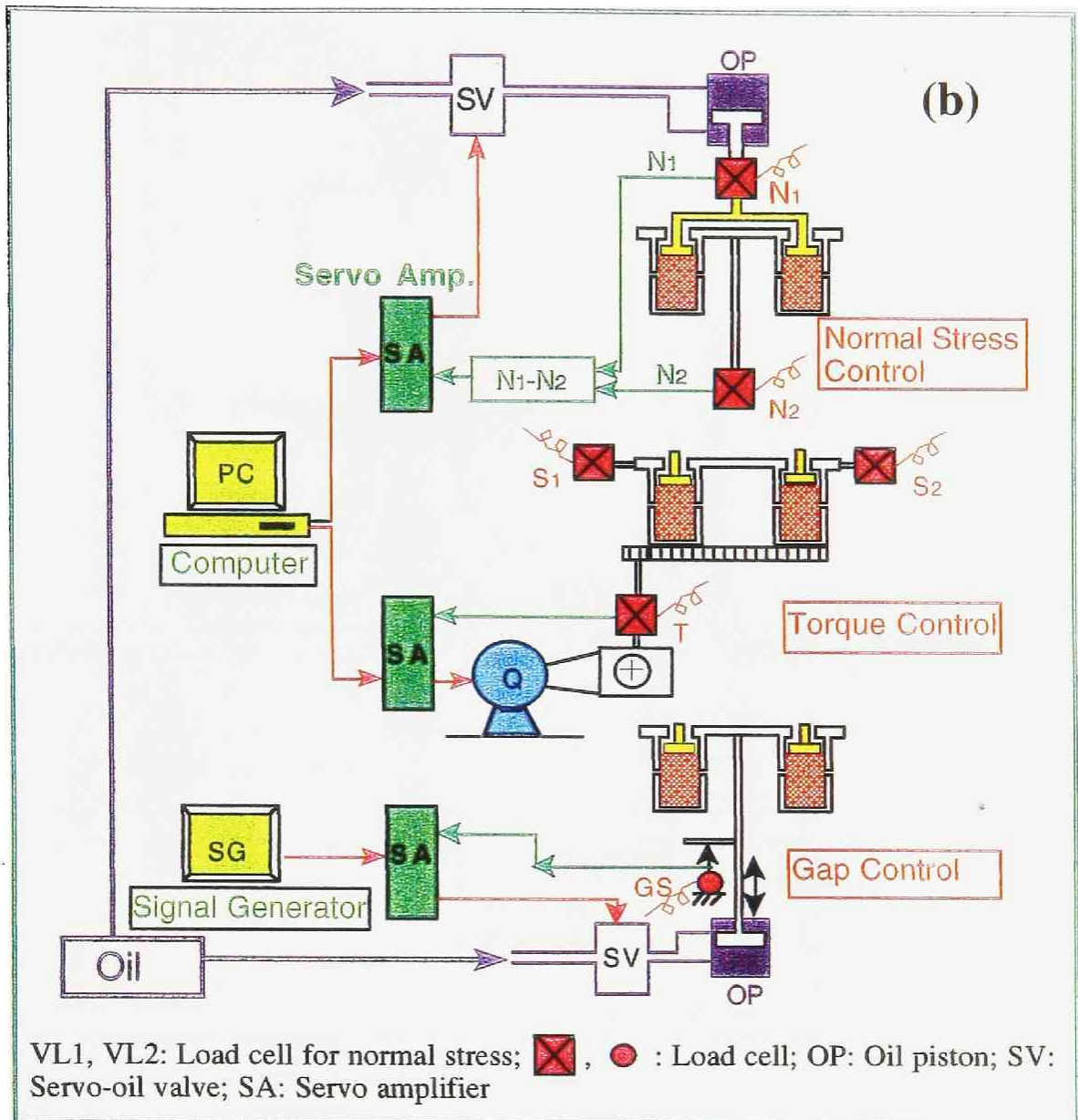
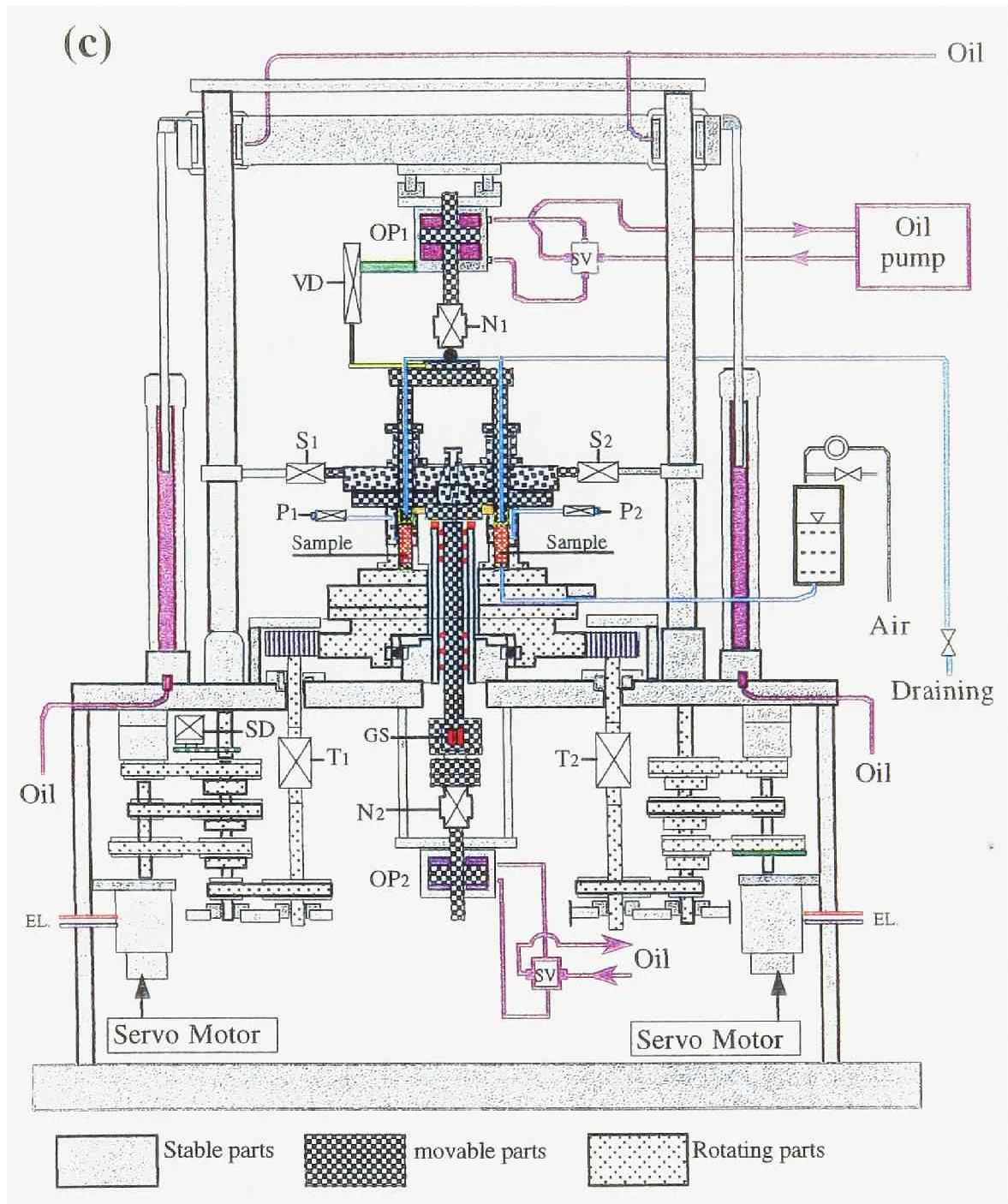


Figure 3.2 Ring shear apparatus (DPRI-Ver.6).

(b): Control system of ring shear apparatus DPRI-Ver.6;



N_1 , N_2 : Load cell for normal stress; S_1 , S_2 : Load cell for shear resistance; P_1 , P_2 : Pore-pressure transducer; GS: gap sensor; OP1, OP2: Oil piston; VD: Vertical displacement meter; SD: Shear displacement meter; T_1 , T_2 : Load cell for Torque

Figure 3.2 Ring shear apparatus (DPRI-Ver.6).

(c): Schematic diagram of ring shear apparatus DPRI-Ver.6;

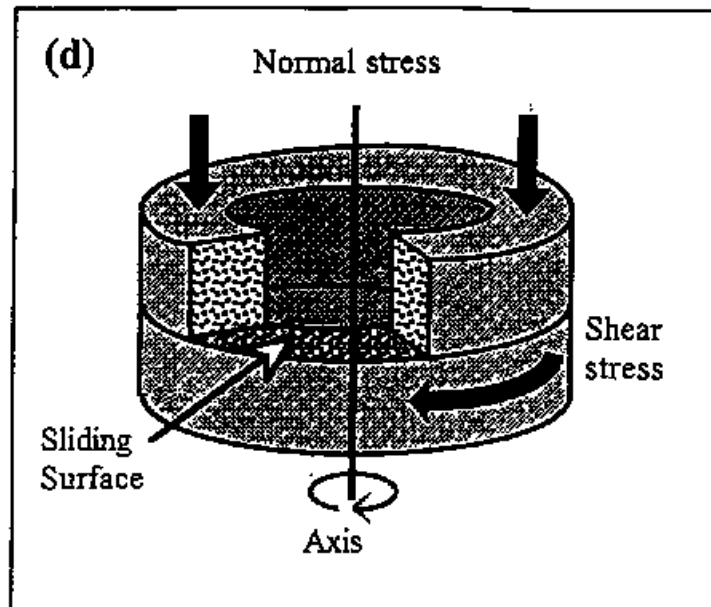


Figure 3.2 Ring shear apparatus (DPRI-Ver.6).

(d): Annular ring-shaped sample in ring shear box;

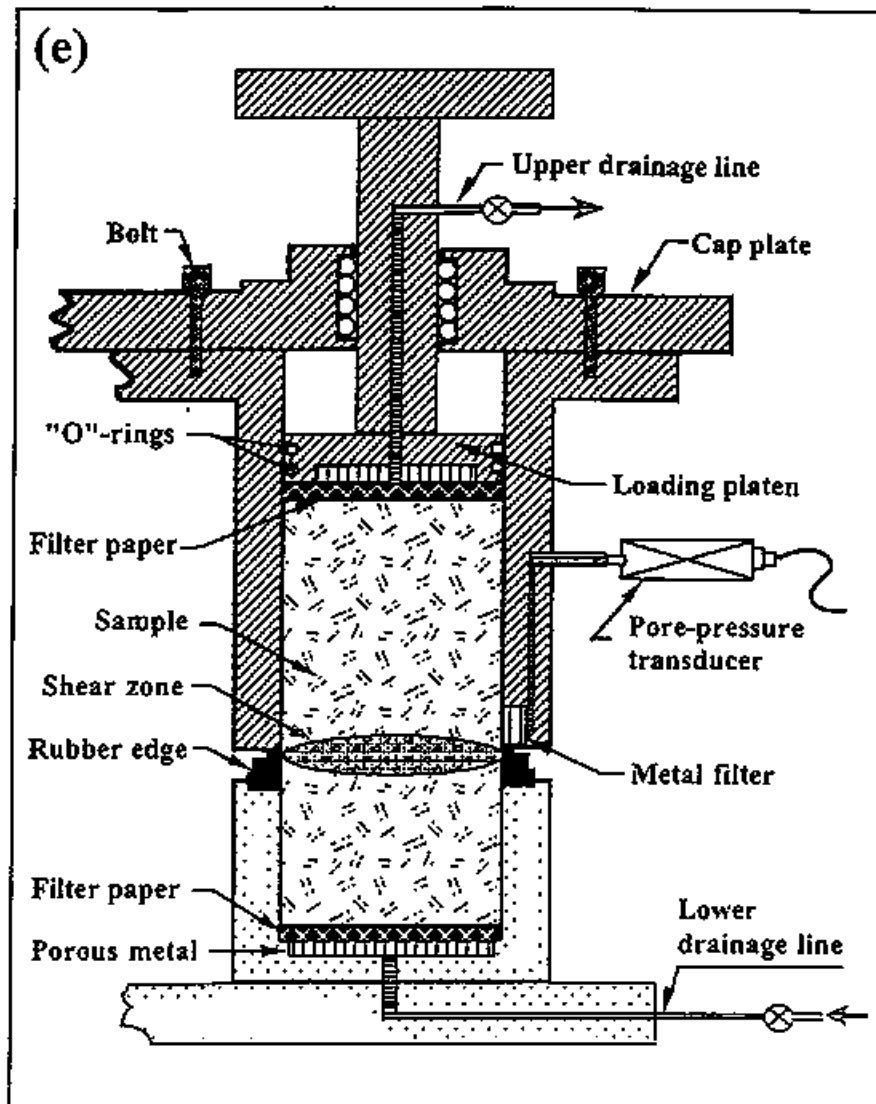


Figure 3.2 Ring shear apparatus (DPRI-Ver.6).

(e): Close-up diagram of the edges and the pore pressure measurements.

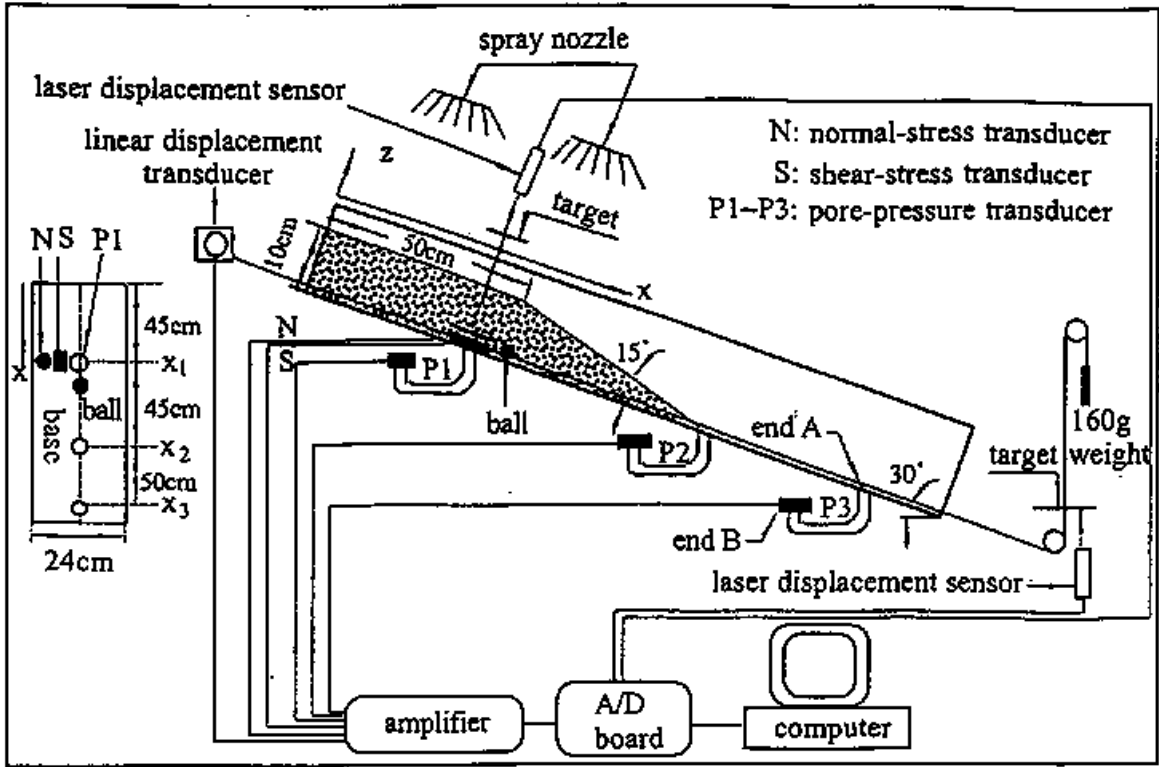


Figure 3. 3 Arrangement of experimental apparatus.

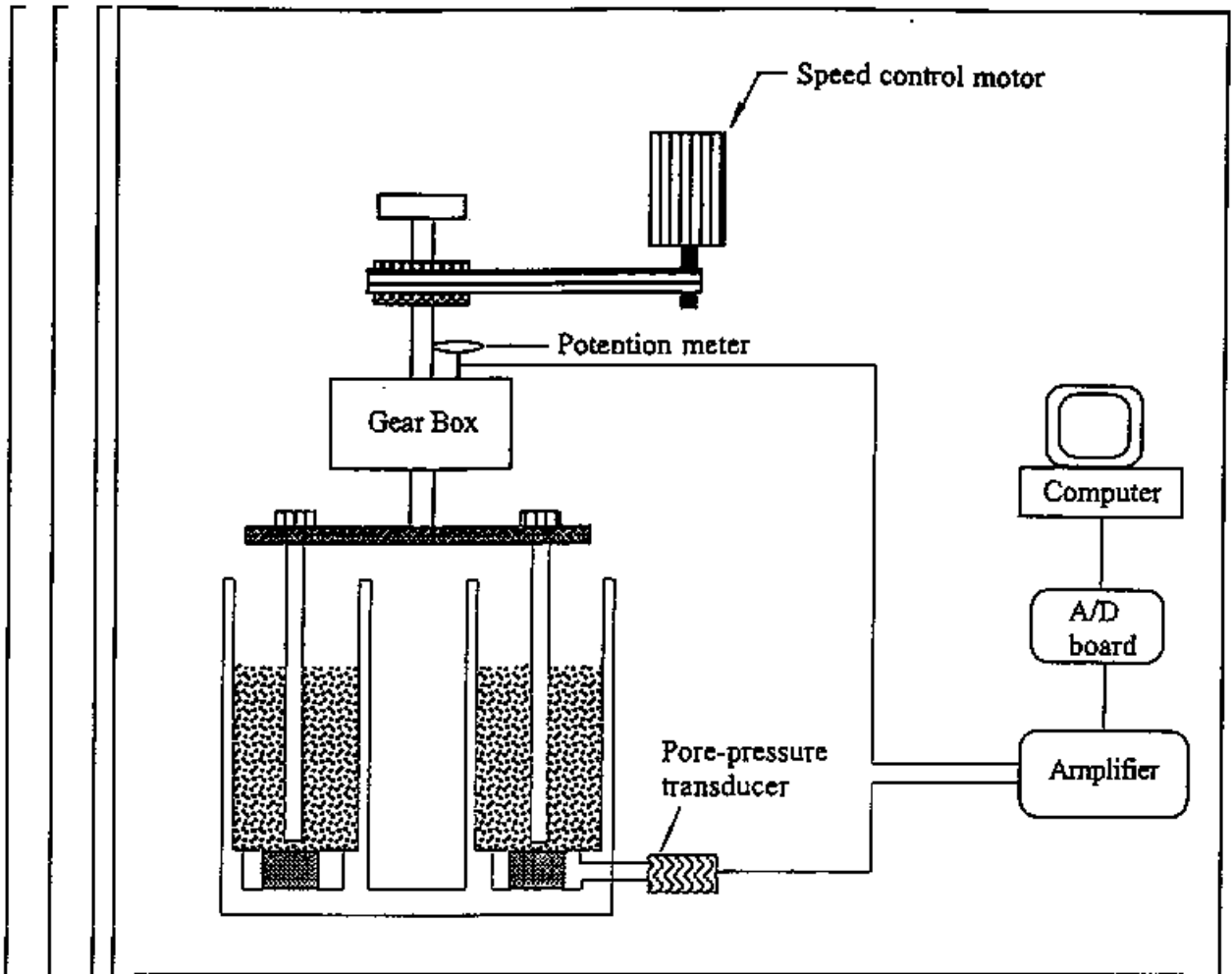


Figure 3.4 Arrangement of apparatus to measure pore pressure in moving saturated soils (after Sassa, 1988).

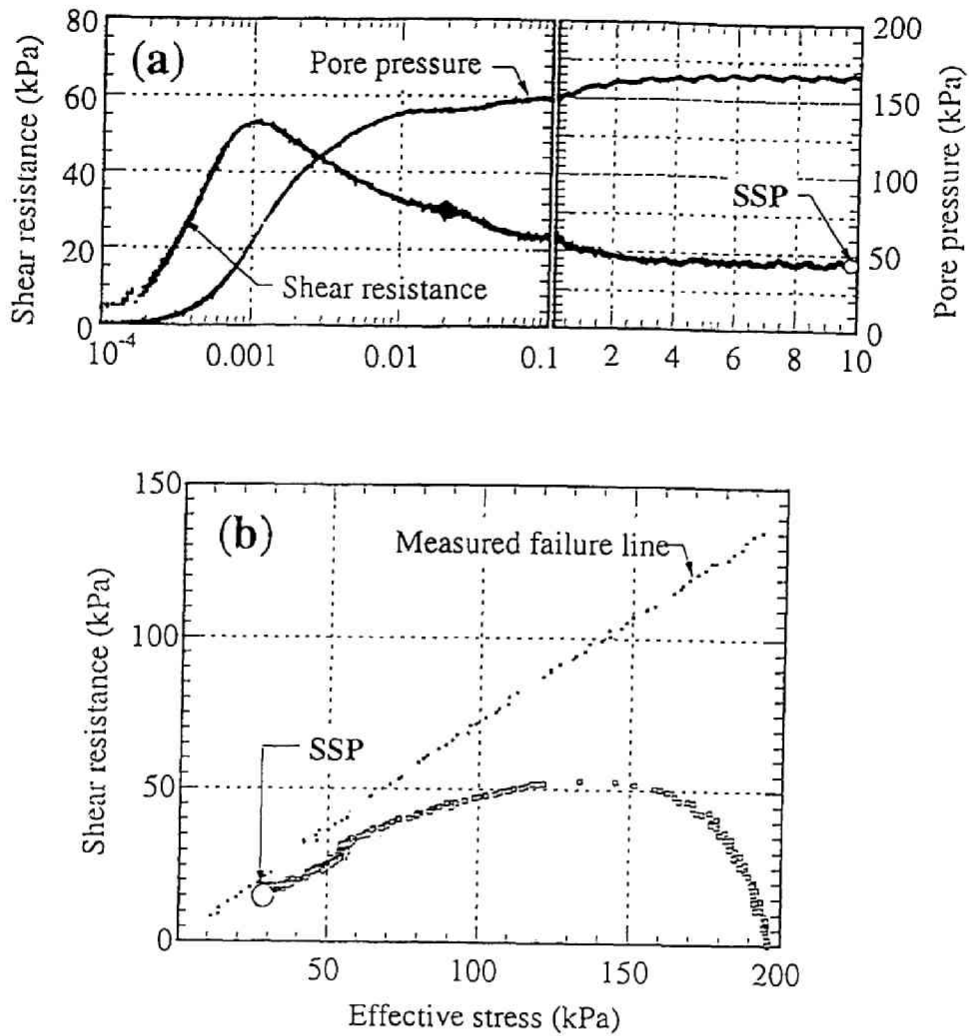


Figure 4.1 Ring shear test on loose sand showing mass liquefaction phenomenon.

(Test: S8_{r,6}; $B_D=0.99$, $D_r=63.3\%$; SSP: Steady State Point.)

(a): Variation of pore pressure and shear resistance in relation to shear displacement;

(b): Effective stress path.

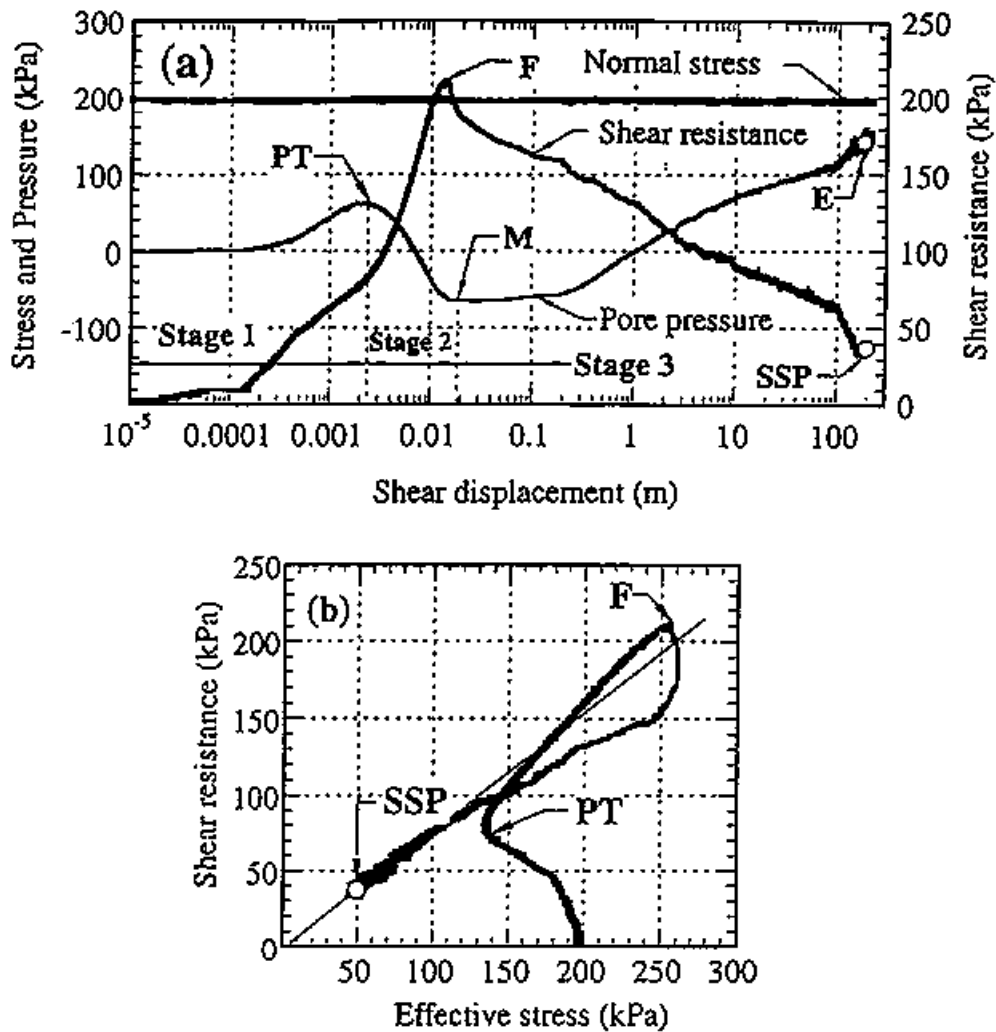


Figure 4.2 Ring shear test on dense sand showing sliding surface liquefaction

(Test: S8_{r7}; $B_D=0.99$, $D_r=95.2\%$, $\sigma = 196$ kPa, PTP: Phase Transformation; SSP: Steady State Point; F: Failure Point; E: Ending of the test).

(a): Variation of pore pressure and shear resistance in relation to shear displacement;

(b): Effective stress path.

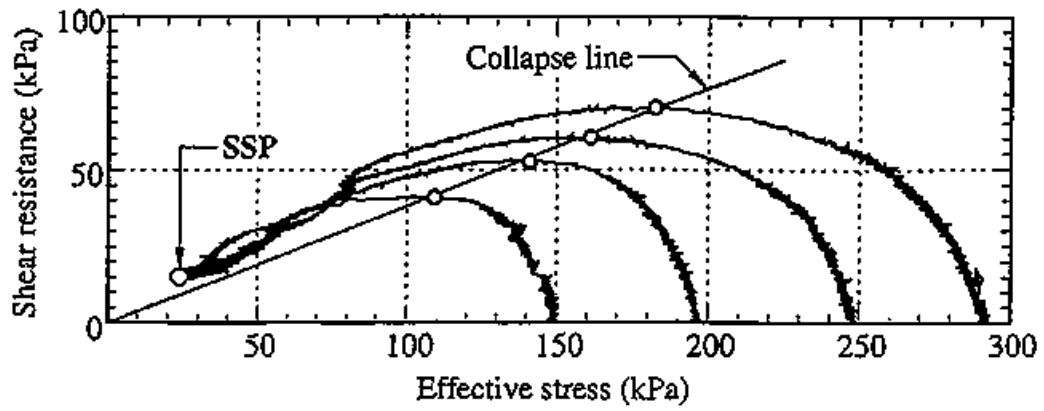


Figure 4.3 Results of tests on S8 at different initial normal stresses.

(Tests: S8_{r,6}, S8_{r,16}, S8_{r,17}, S8_{r,18}; D_r = 63.3%; SSP: Steady State Point).

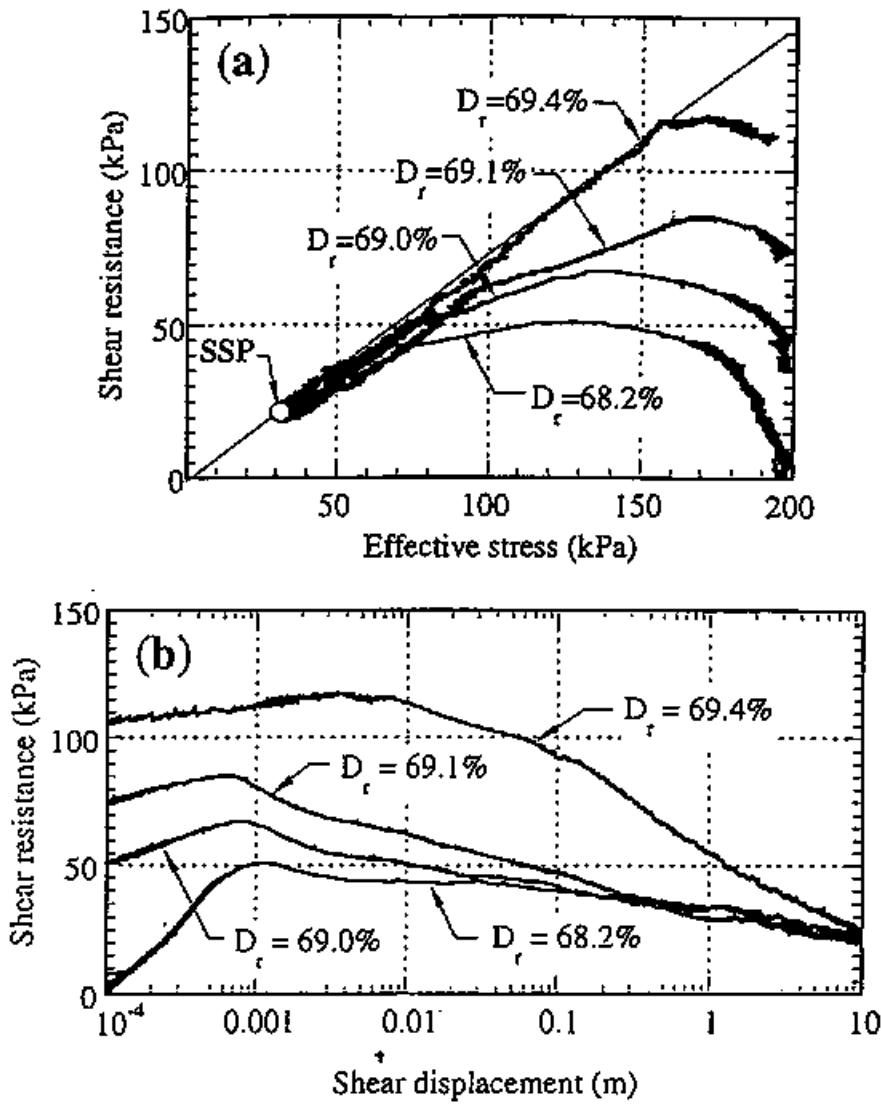


Figure 4.4 Results of tests on samples at different initial shear stresses.
 (Tests: S8_{r,21}, S8_{r,22}, S8_{r,23}, S8_{r,25}; $D_r = 68.2\%$ – 69.4% ; SSP: Steady State Point).
 (a) Effective stress paths;
 (b) Variation of shear resistance in relation to shear displacement.

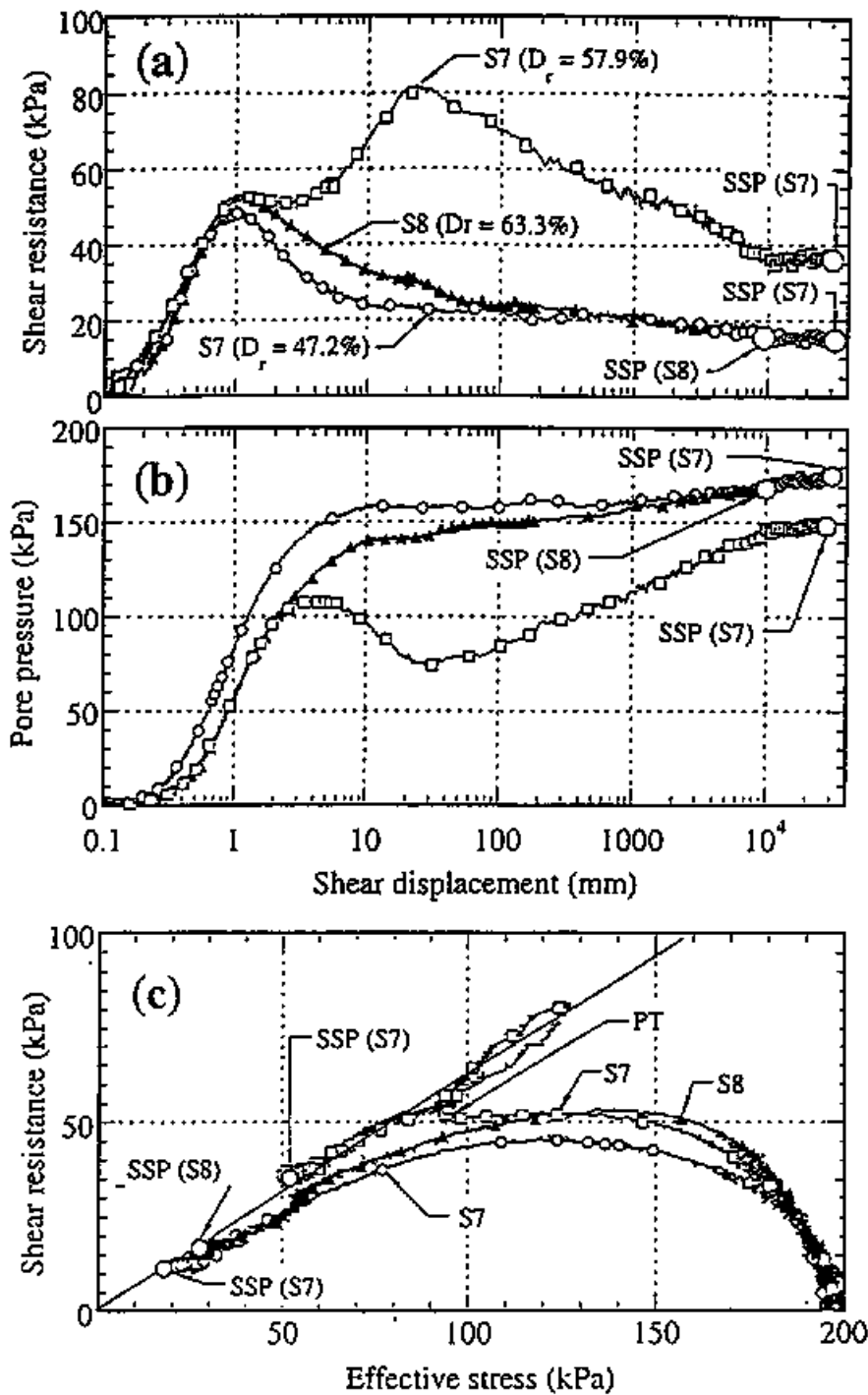


Figure 4.5 Comparison of the results of tests on S7 and S8 in loose state.

(Tests: $S8_{r,6}$, $S7_{r,11}$, $S7_{r,15}$; $D_r = 63.3\%$ for $S8_{r,6}$; $D_r = 47.2\%$ and 57.9% for $S7_{r,11}$ and $S7_{r,1}$, respectively).

(a): Variation of shear resistances in relation to shear displacement;

(b): Variation of pore pressures in relation to shear displacement;

(c): Effective stress paths.

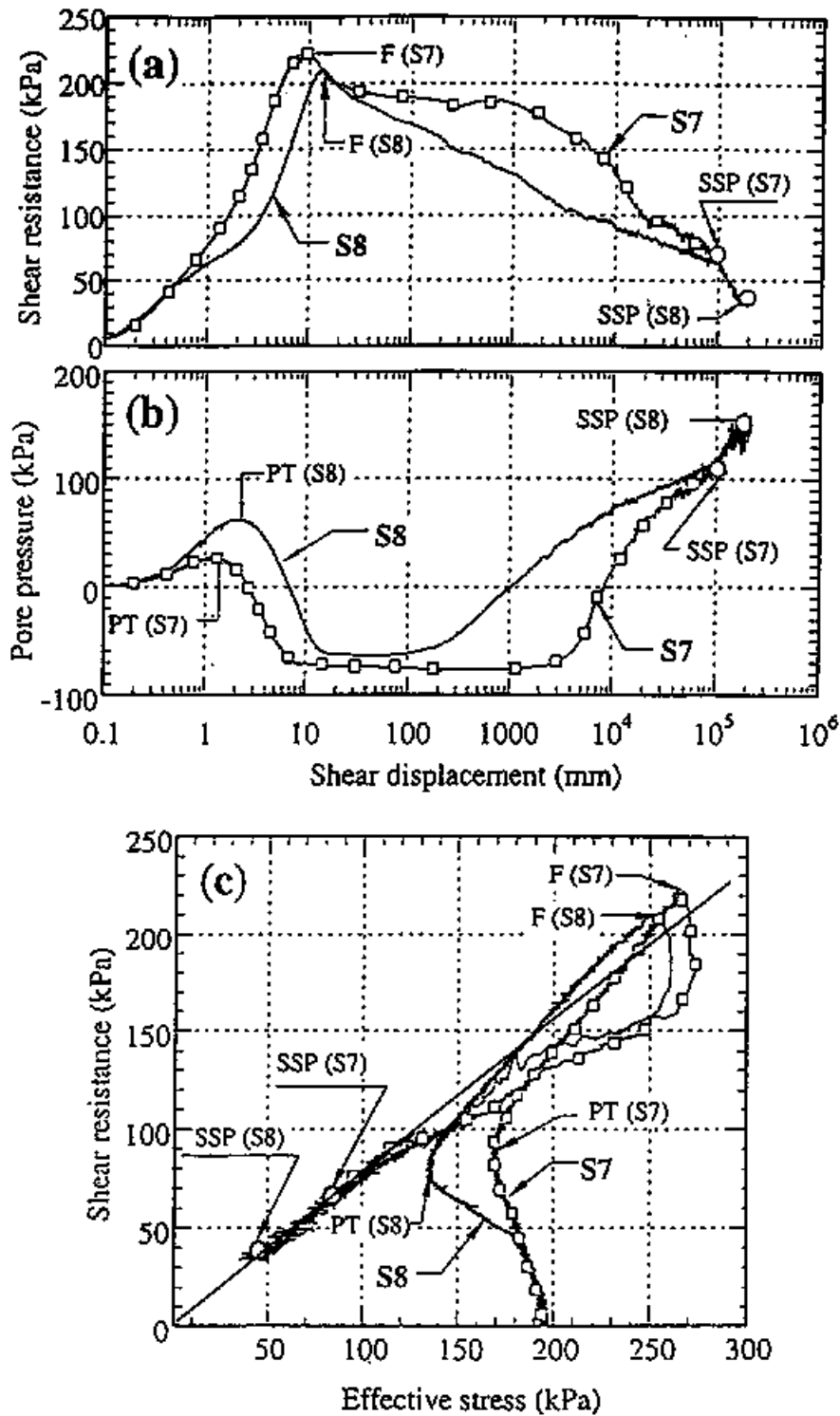


Figure 4.6 Typical test results for dense S7 and S8.

(Tests: $S8_{r,7}$, $S7_{r,7}$; $D_r = 88.3\%$ for $S7_{r,7}$; $D_r = 95.2\%$ for $S8_{r,7}$)

(a): Shear resistance versus shear displacement;

(b): Pore pressures versus shear displacement;

(c) Effective stress paths.

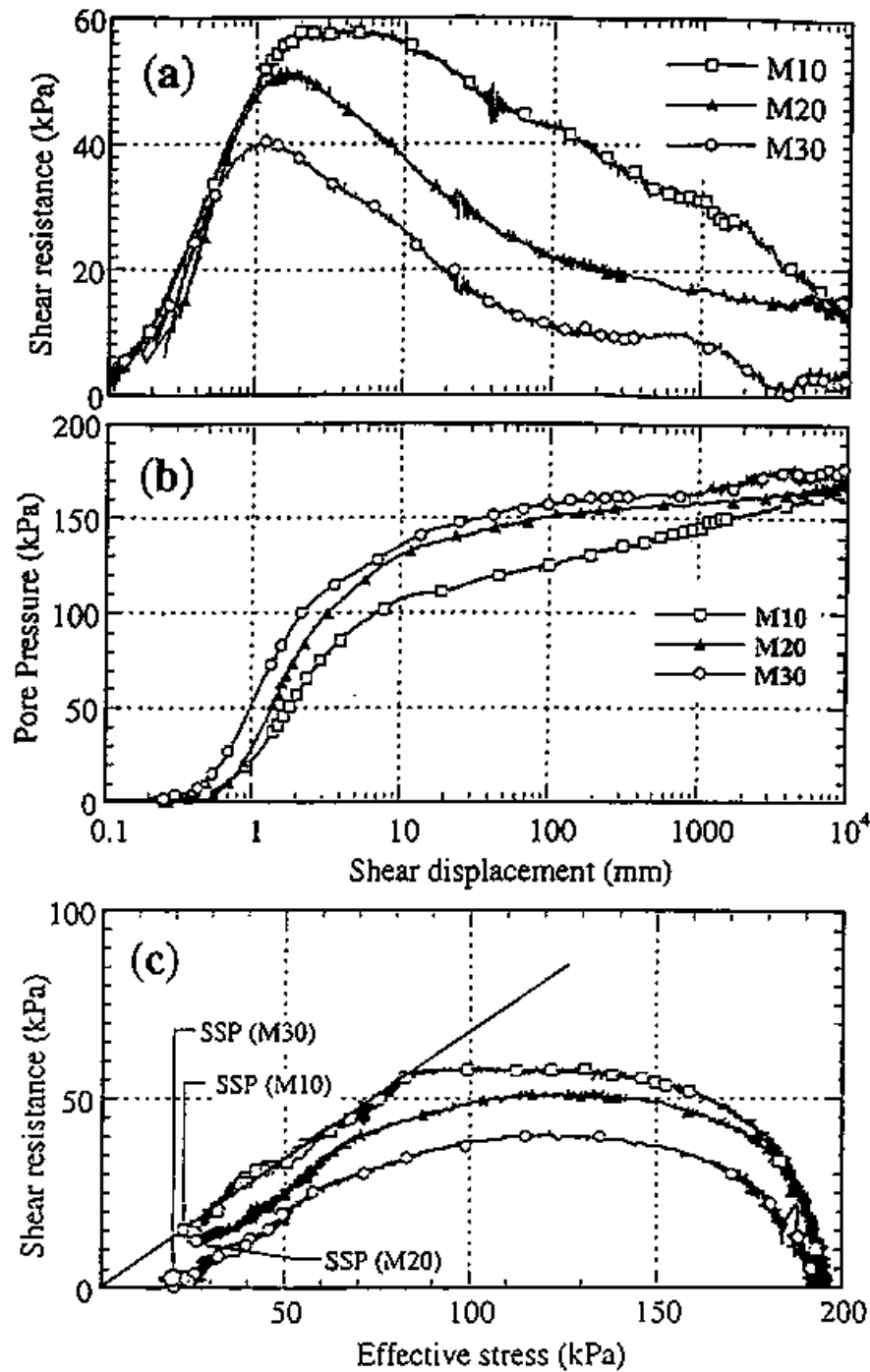


Figure 4.7 Comparison on the results of tests on loose M10, M20, and M30.

(Tests: M10_{r,6}, M20_{r,5}, M30_{r,5}; $D_r = 52.6\%$, 63.3% , and 67.5% for M10, M20, and M30, respectively)

(a): Variation of shear resistance in relation to shear displacement;

(b): Variation of pore pressure in relation to shear displacement;

(c): Effective stress paths.

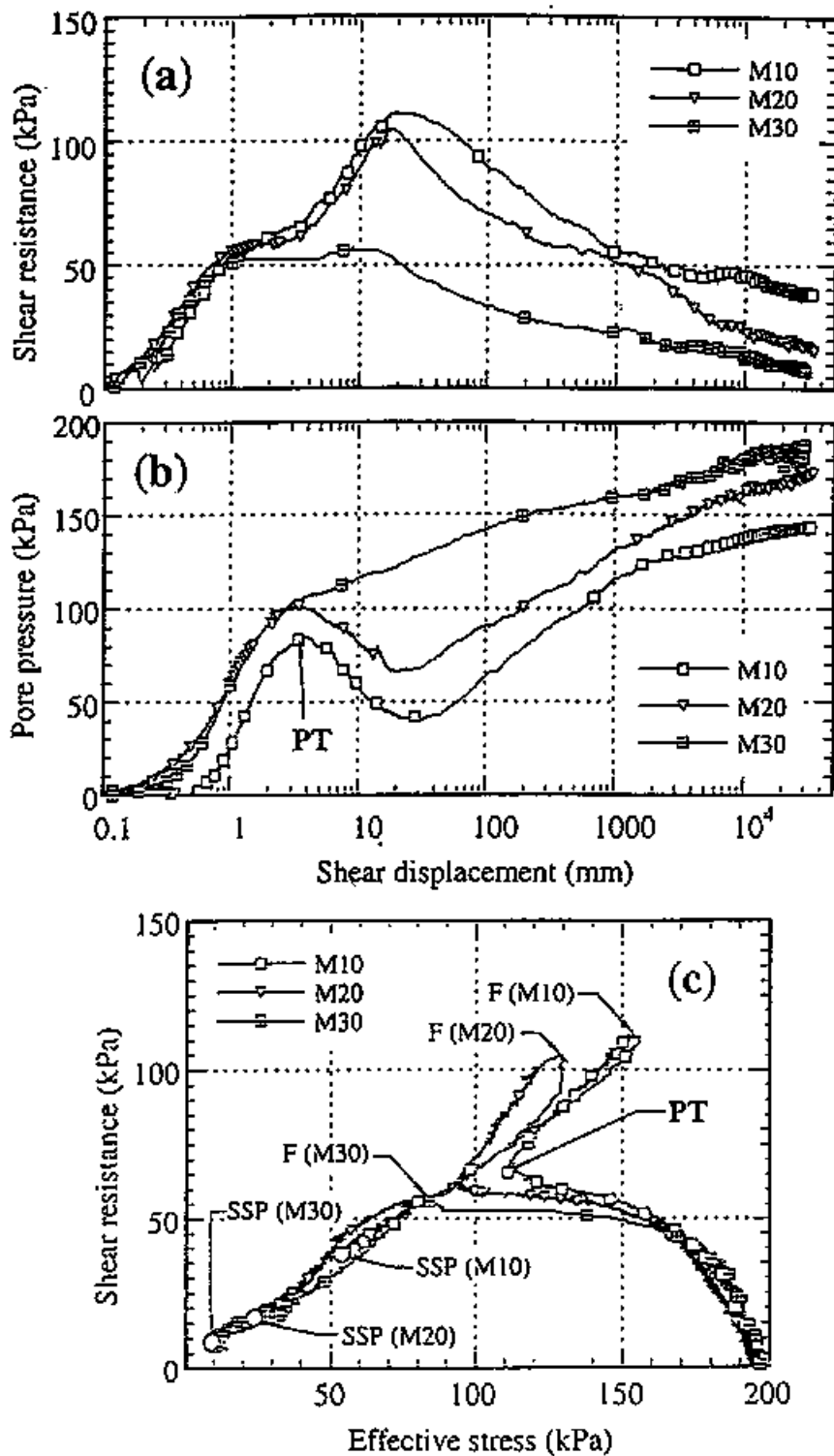


Figure 4.8 Comparison on the results of tests on dense M10, M20, and M30.

(Tests: M10_{r,t}, M20_{r,t}, M30_{r,t}; Dr = 70.4%, 79.4%, and 80.5% for M10, M20, and M30, respectively; PT: Phase transformation)

(a): Variation of shear resistance in relation to shear displacement;

(b): Variation of pore pressure in relation to shear displacement;

(c): Effective stress paths.

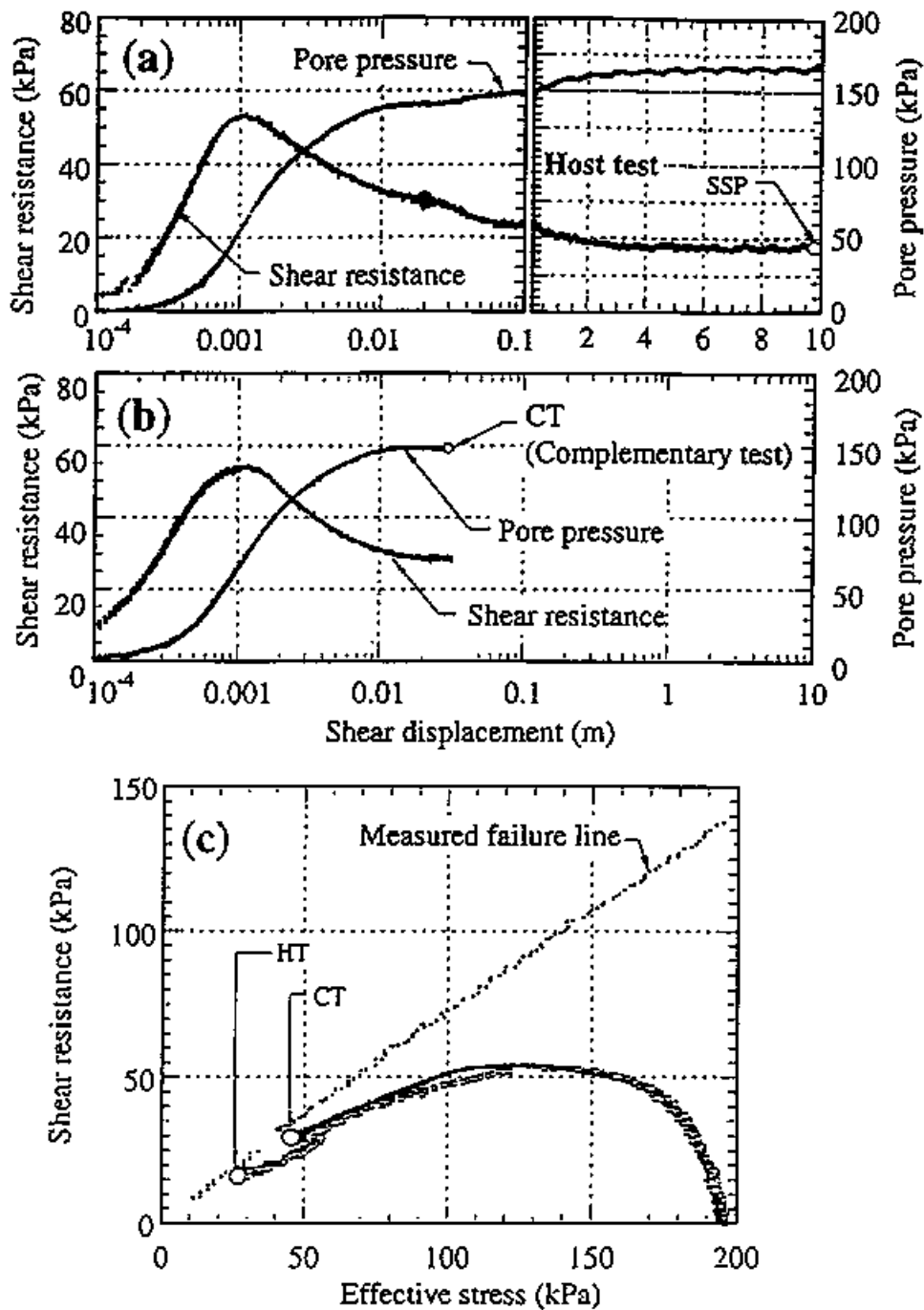


Figure 4.9 Ring shear test on loose sand showing mass liquefaction phenomenon.

(Test S8r.6 and its complementary test; $B_D=0.99$, $D_r=63.3\%$, $\sigma=196$ kPa, SSP: Steady State Point.).

- (a): Variation of pore pressure and shear resistance in relation to shear displacement for the host test;
- (b): Variation of pore pressure and shear resistance in relation to shear displacement for the complementary test;
- (c): Effective stress paths.

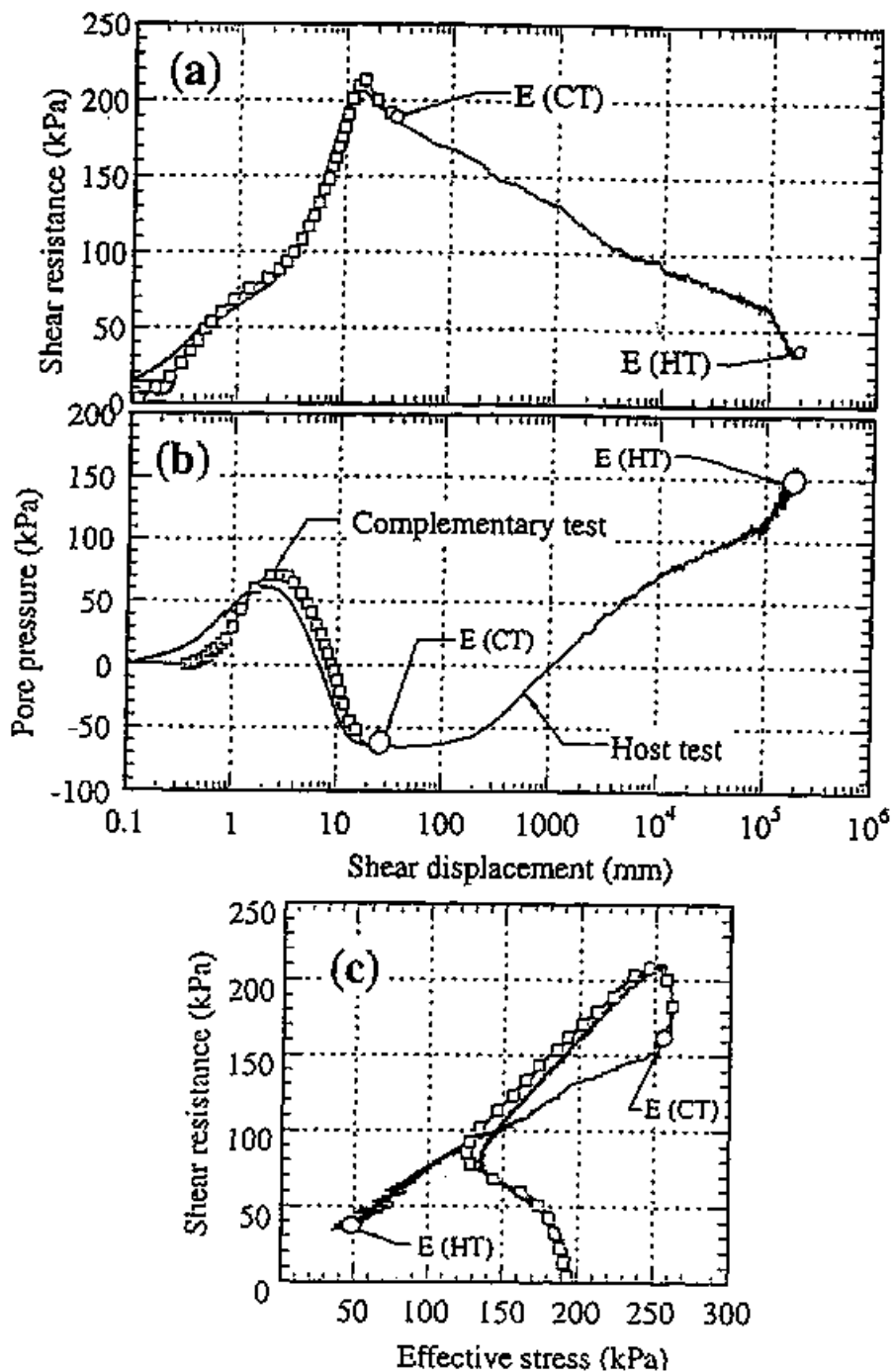


Figure 4.11 Ring shear test on dense sand showing sliding surface liquefaction phenomenon.

(Test S8_{r,7} and its complementary test; $B_D = 0.99$, $D_r = 95.2\%$ and 94.9% for the host test and complementary test on dense S8, respectively; SSP: Steady State Point).

(a): Variation of pore pressure and shear resistance in relation to shear displacement for the host test;

(b): Variation of pore pressure and shear resistance in relation to shear displacement for the complementary test;

(c): Effective stress paths.



Figure 4.10 Shear deformation of vertically inserted slice of Toyoura sand after 3-cm shear for the complementary test on Test S8r.6 (showing mass liquefaction).

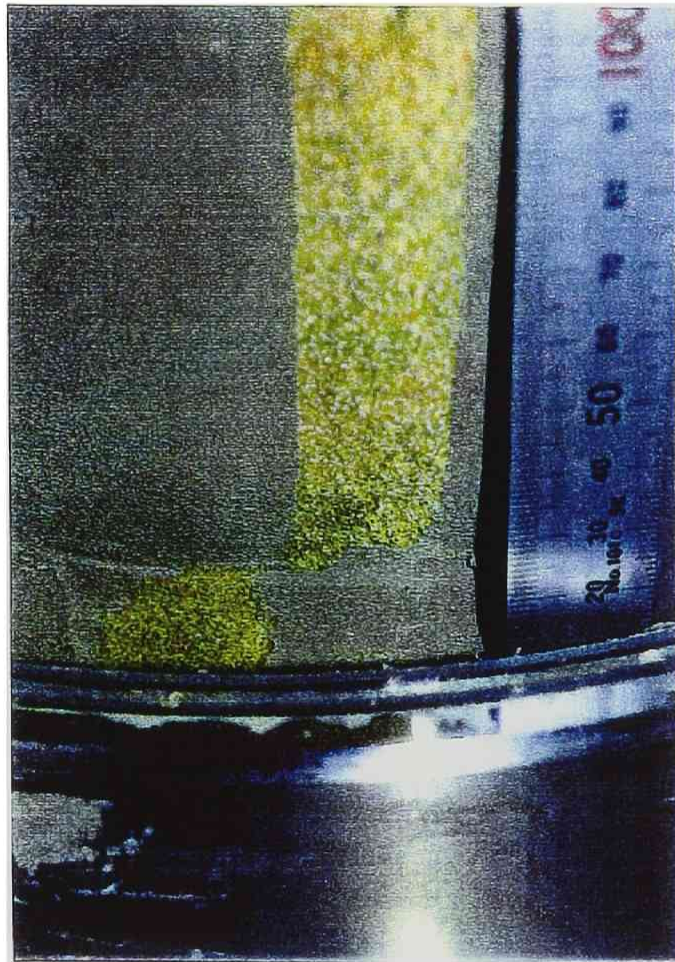


Figure 4.12 Shear deformation of vertically inserted slice of Toyoura sand after 3-cm shear in the complementary test showing sliding surface liquefaction for test S8_{r,7} ($B_D = 0.99$; $D_r = 94.9\%$).

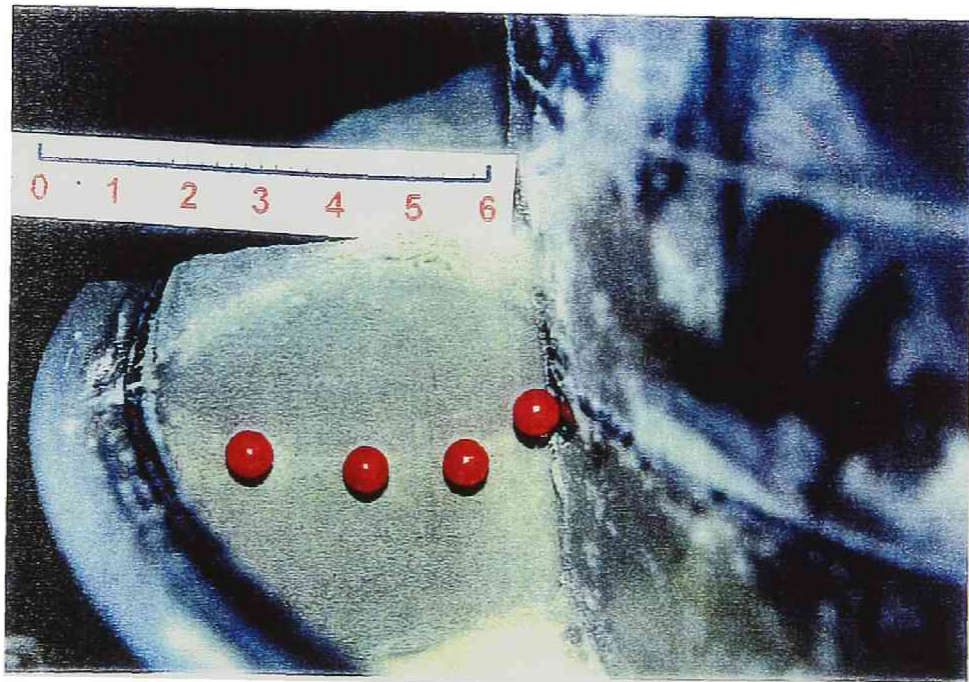


Figure 4.13 Formation of shear zone in the test on loose S8 showing mass liquefaction (Test S8_{r,6}; $B_D = 0.99$; $D_r = 63.3\%$).

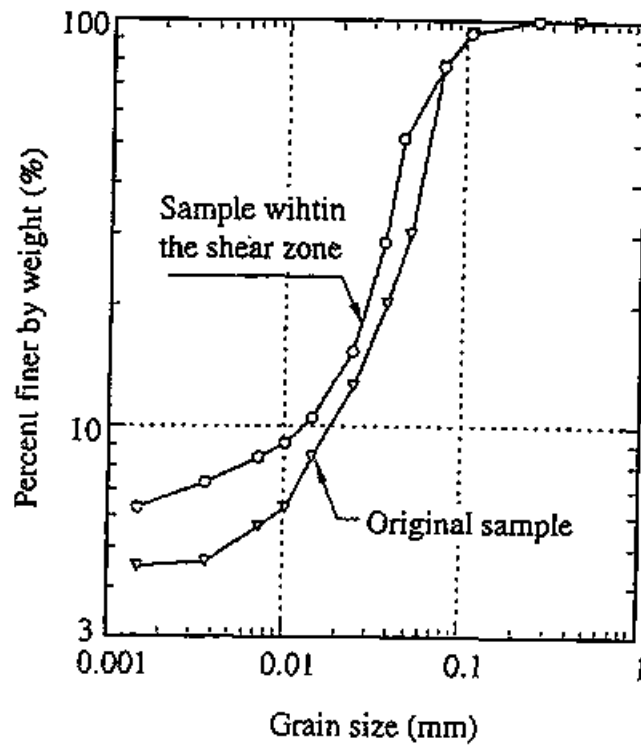


Figure 4.14 Grain-size distribution curves for the original sample and that taken from the shear zone after test on loose S8 showing mass liquefaction. (Test S8_{r,6}; $B_D = 0.99$; $D_r = 63.3\%$; shear displacement: 10 m).

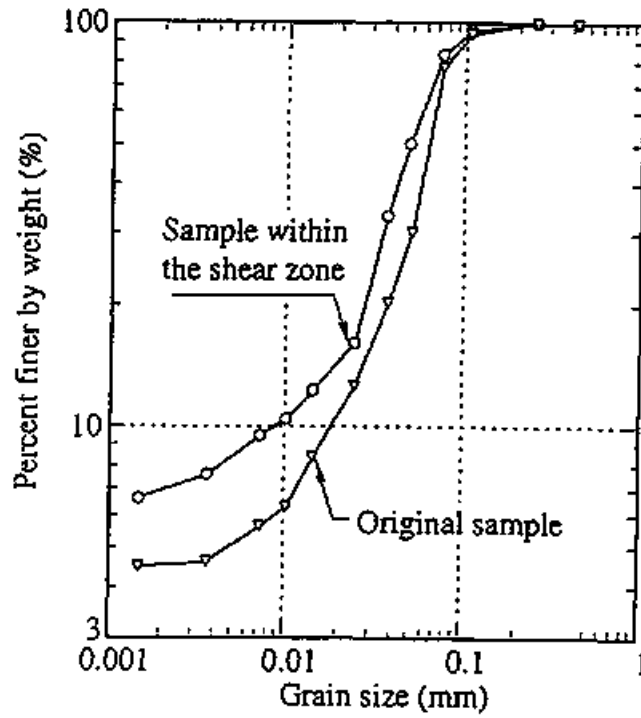


Figure 4.15 Grain-size distribution curves for the original sample and that taken from the shear zone after test on dense SS showing sliding surface liquefaction. (Test S8_{r7}; B_D = 0.99; D_r = 95.2%; shear displacement: 210 m).



Figure 4.16 Formation of shear zone in the test on dense S8 showing sliding surface liquefaction.

(Test S8_{r,7}; $B_D = 0.99$; $D_r = 95.2\%$; shear displacement: 210 m).

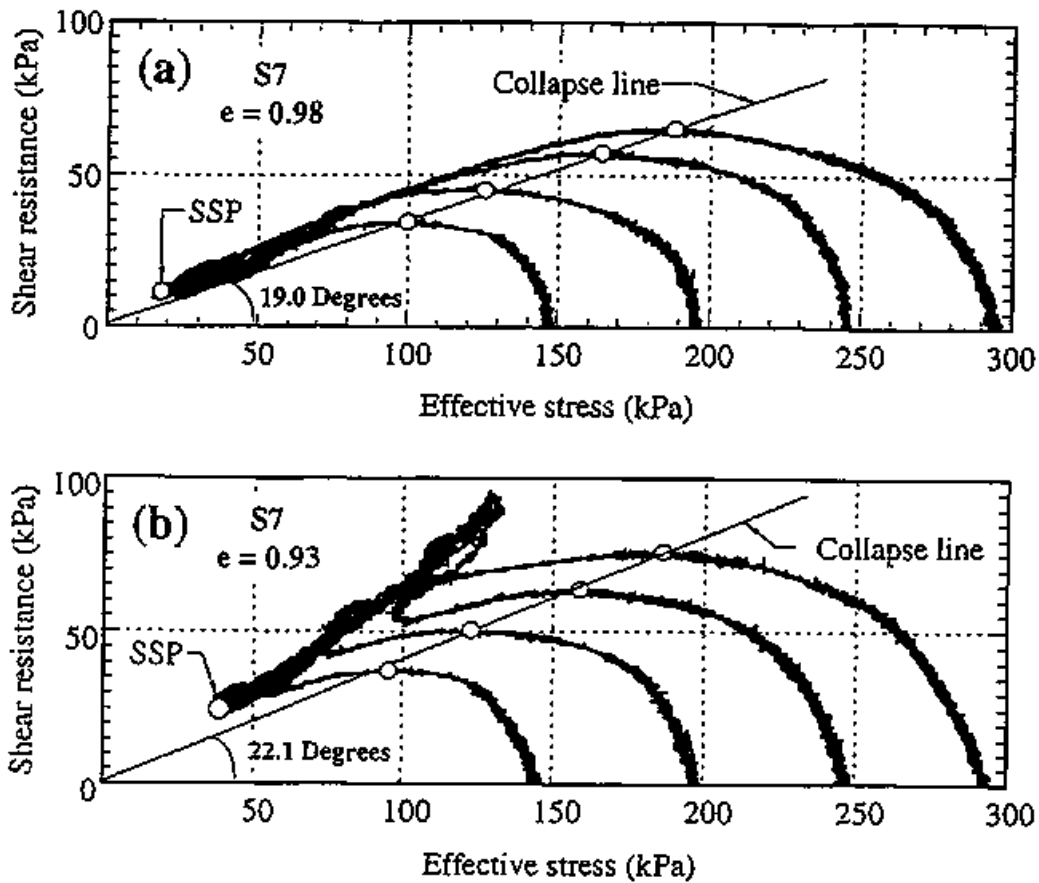


Figure 4.17 Results of tests on loose S7 at different initial normal stresses for two different test series.

- (a): Effective stress paths for the tests with D_r being approximately 47.2% ($S7_{r,10}$; $S7_{r,11}$; $S7_{r,12}$; $S7_{r,13}$);
- (b): Effective stress paths for the tests with D_r being approximately 56.6% ($S7_{r,14}$; $S7_{r,15}$; $S7_{r,16}$; $S7_{r,17}$).

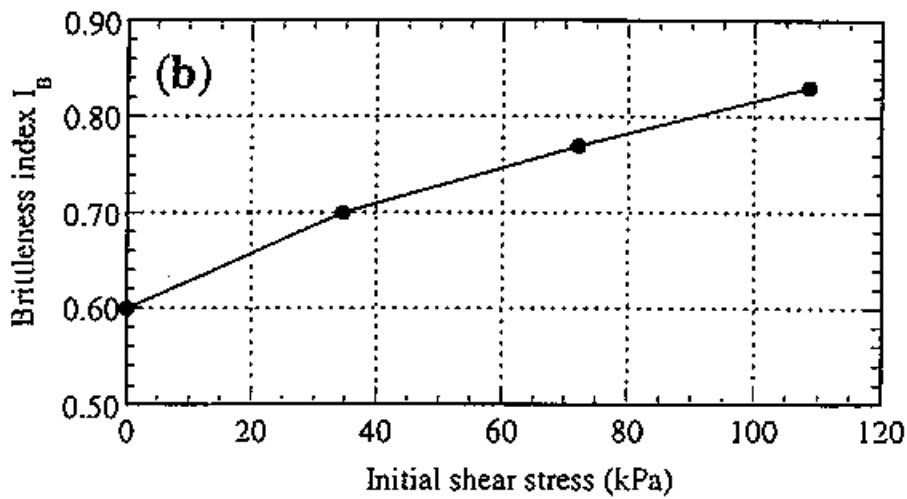
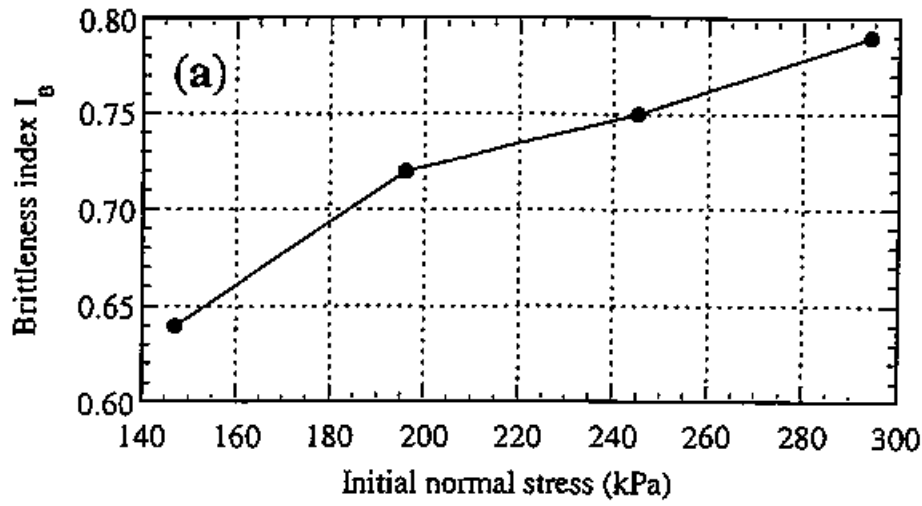


Figure 4.18 Brittliness indexes at different initial stress states.

- (a) Variation of brittliness index in relation to initial normal stress ($S8_{r,6}$, $S8_{r,16}$, $S8_{r,17}$, $S8_{r,18}$);
- (b) Variation of brittliness index in relation to initial shear stress ($S8_{r,6}$, $S8_{r,16}$, $S8_{r,17}$, $S8_{r,18}$).

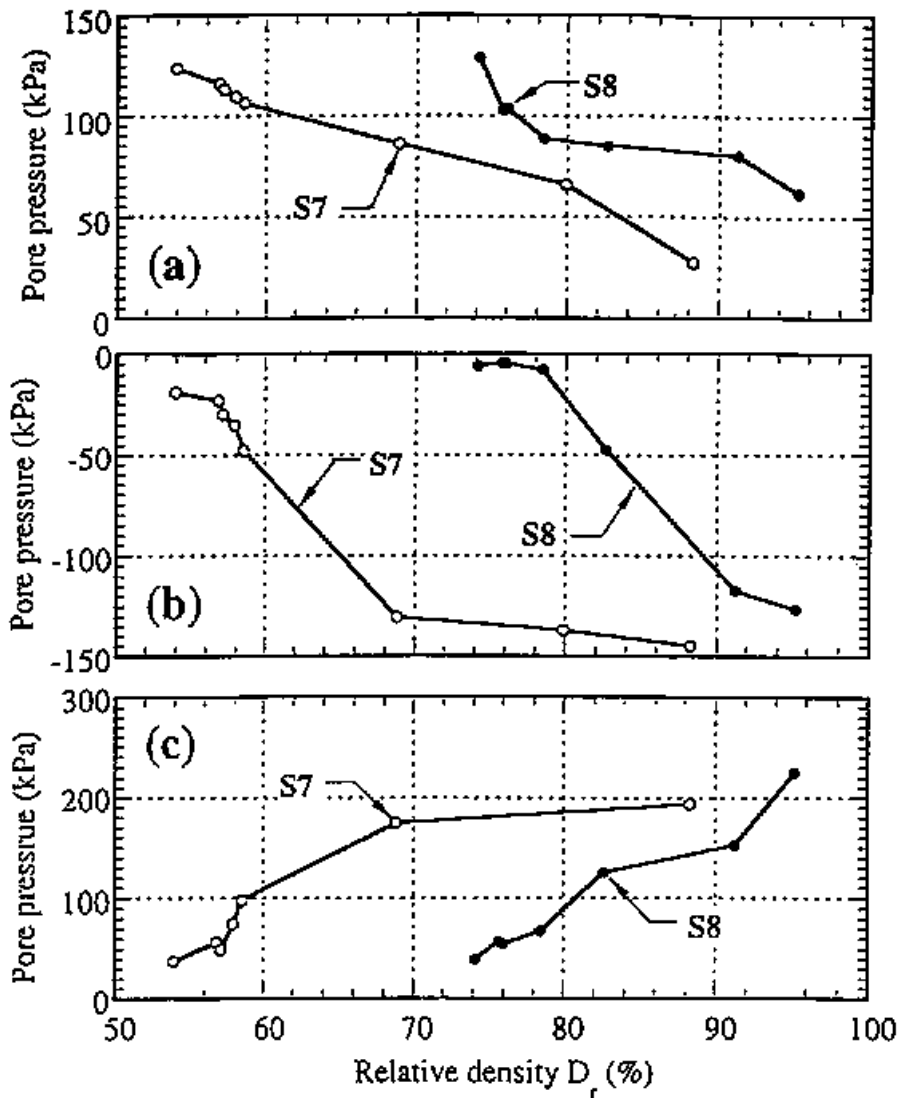


Figure 4.19 Variation of generated pore pressure in relation to relative density during different undrained shear periods for S7 and S8.

- (a): Generated pore pressure during Stage 1 due to the failure of metal stable soil structure and orientation of grains;
- (b): Generated pore pressure during Stage 2 due to the dilatancy of dense sand accompanying the further shearing;
- (c): Generated pore pressure during Stage 3 due to grain crushing accompanying the shear displacement.

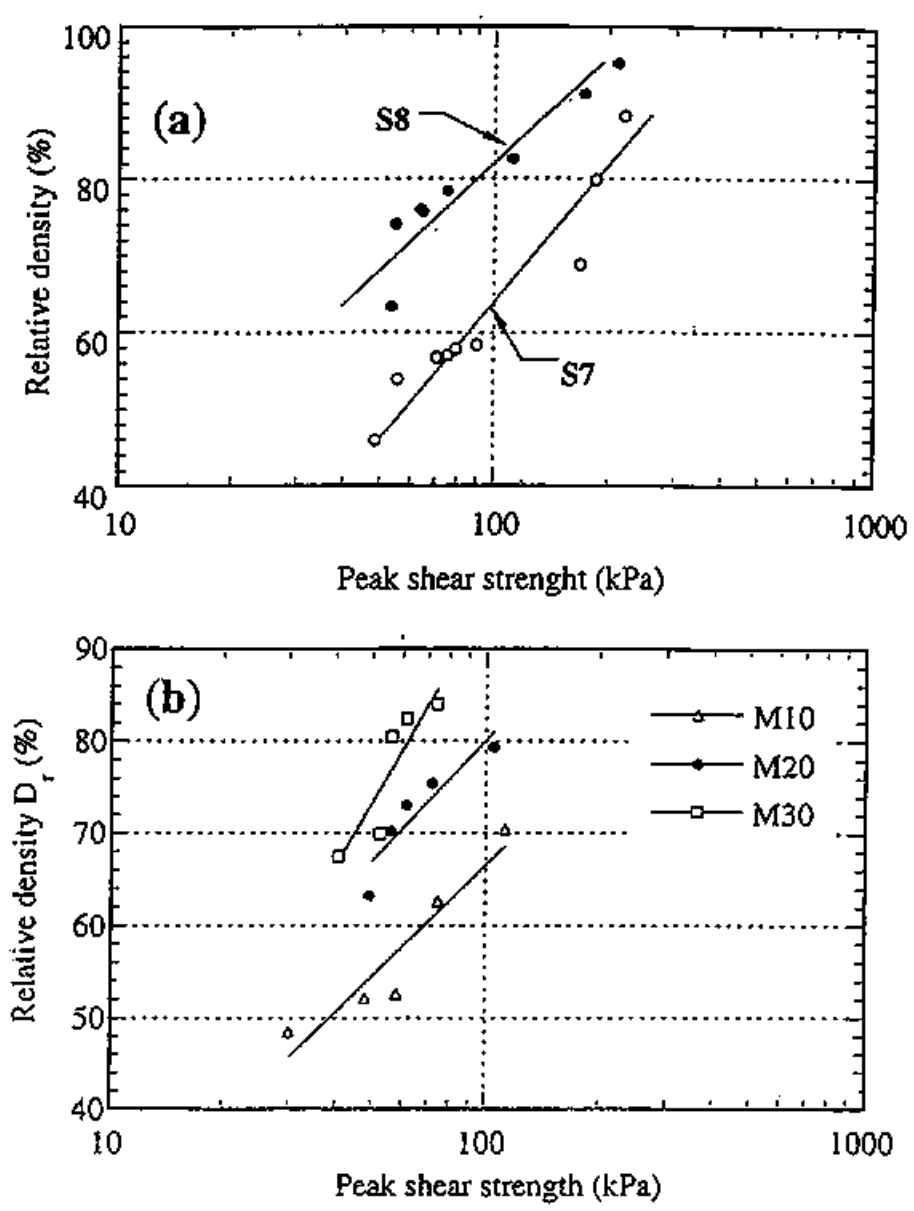


Figure 4.20 D_r versus peak shear strength.
 (a) For the tests on S7 and S8;
 (b) For the tests on M10, M20, and M30.

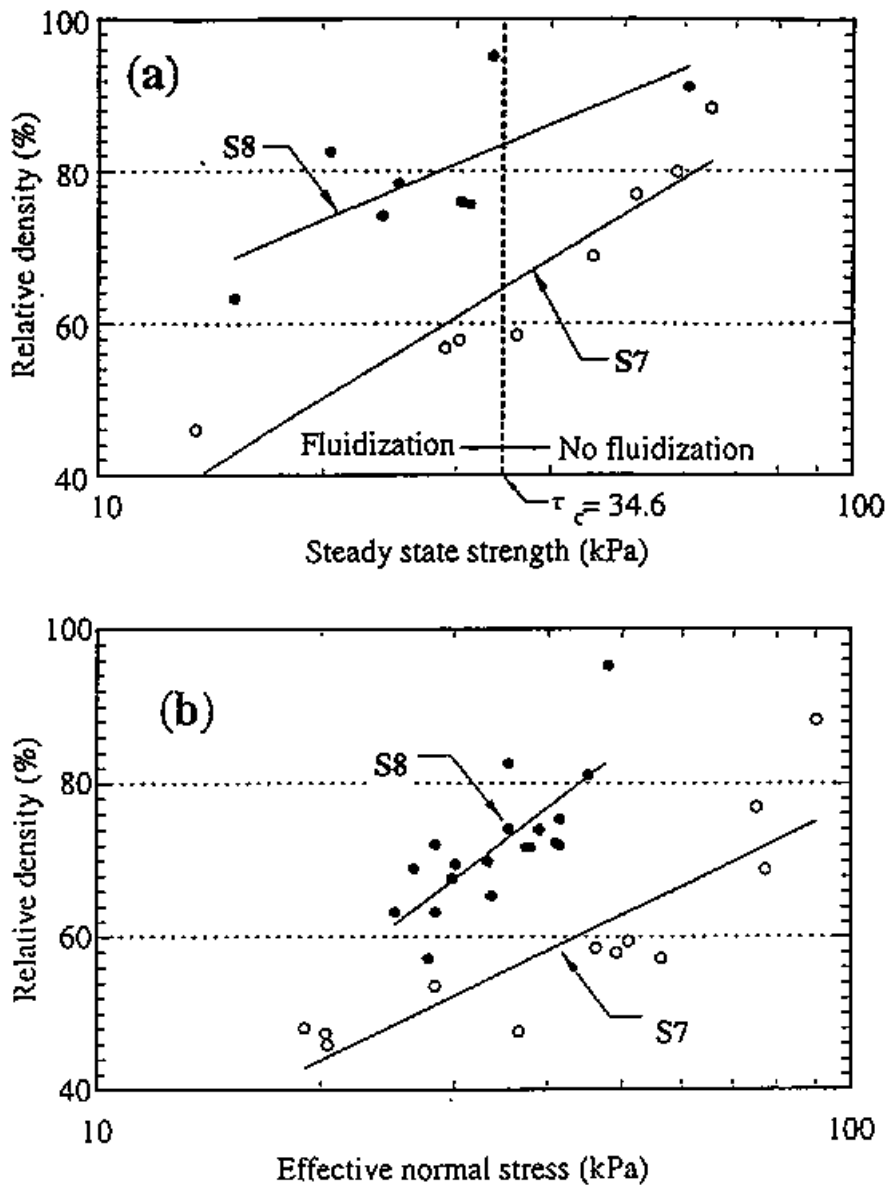


Figure 4.21 Ring shear test data for S7 and S8 at steady state.
 (a): D_r versus $\log(\tau_s)$; (b): D_r versus $\log(\sigma_s')$.

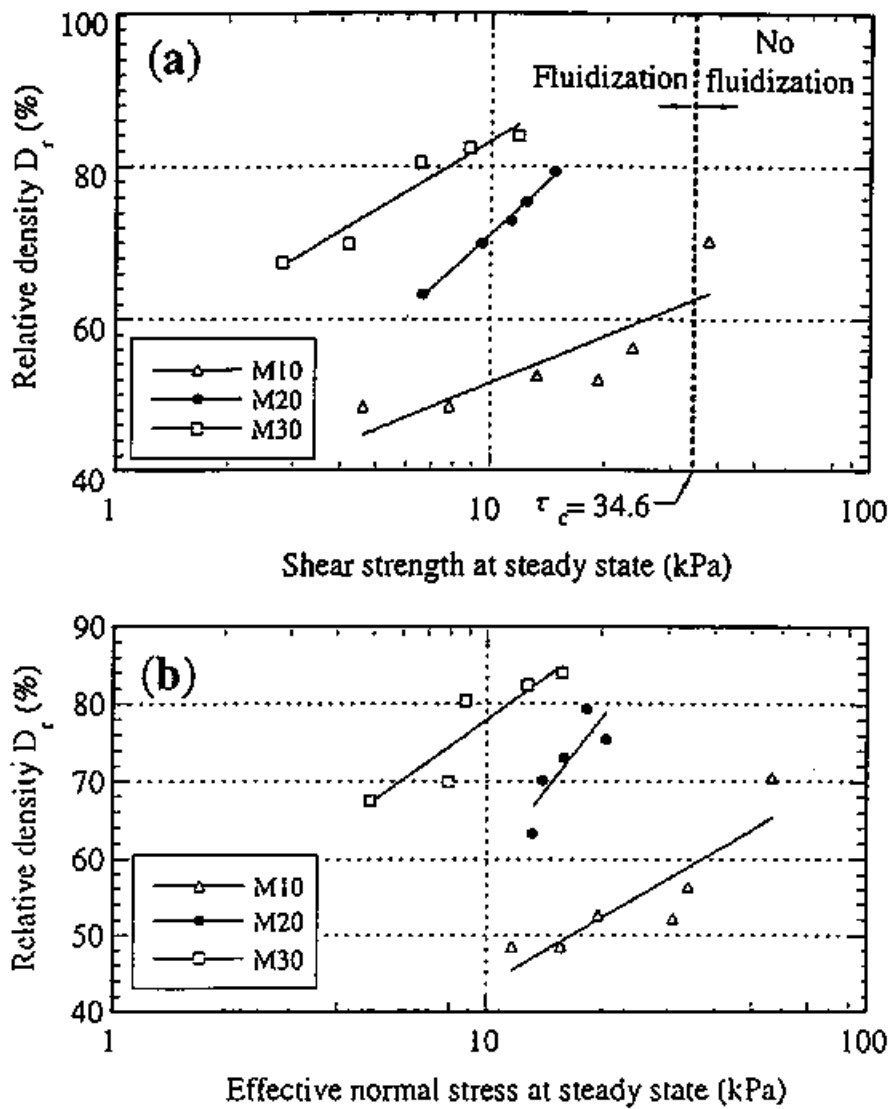


Figure 4.22 Ring shear test data for M10, M20, and M30 at steady state.

(a): D_r versus $\log(\tau_s)$; (b): D_r versus $\log(\sigma'_s)$.

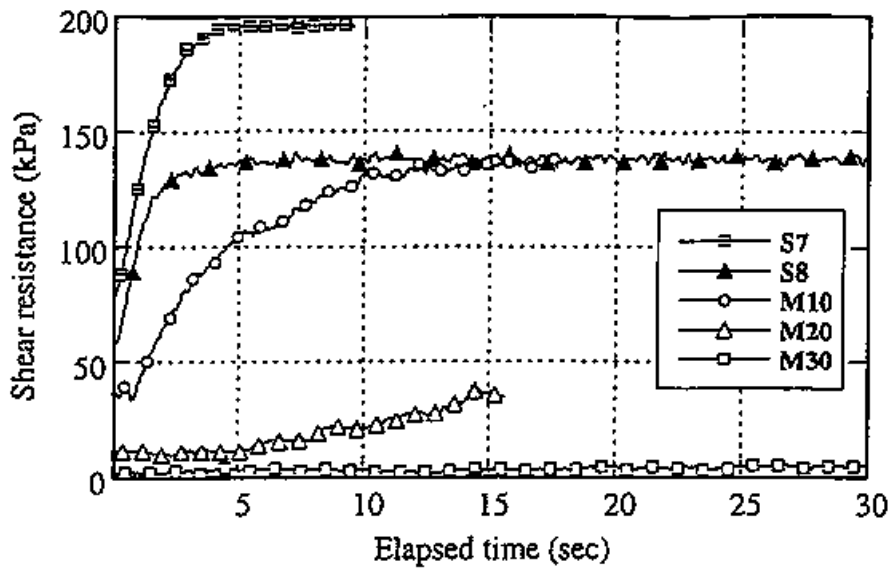


Figure 4.23 Recovering of shear resistance due to excess pore pressure dissipation from the shear zone.

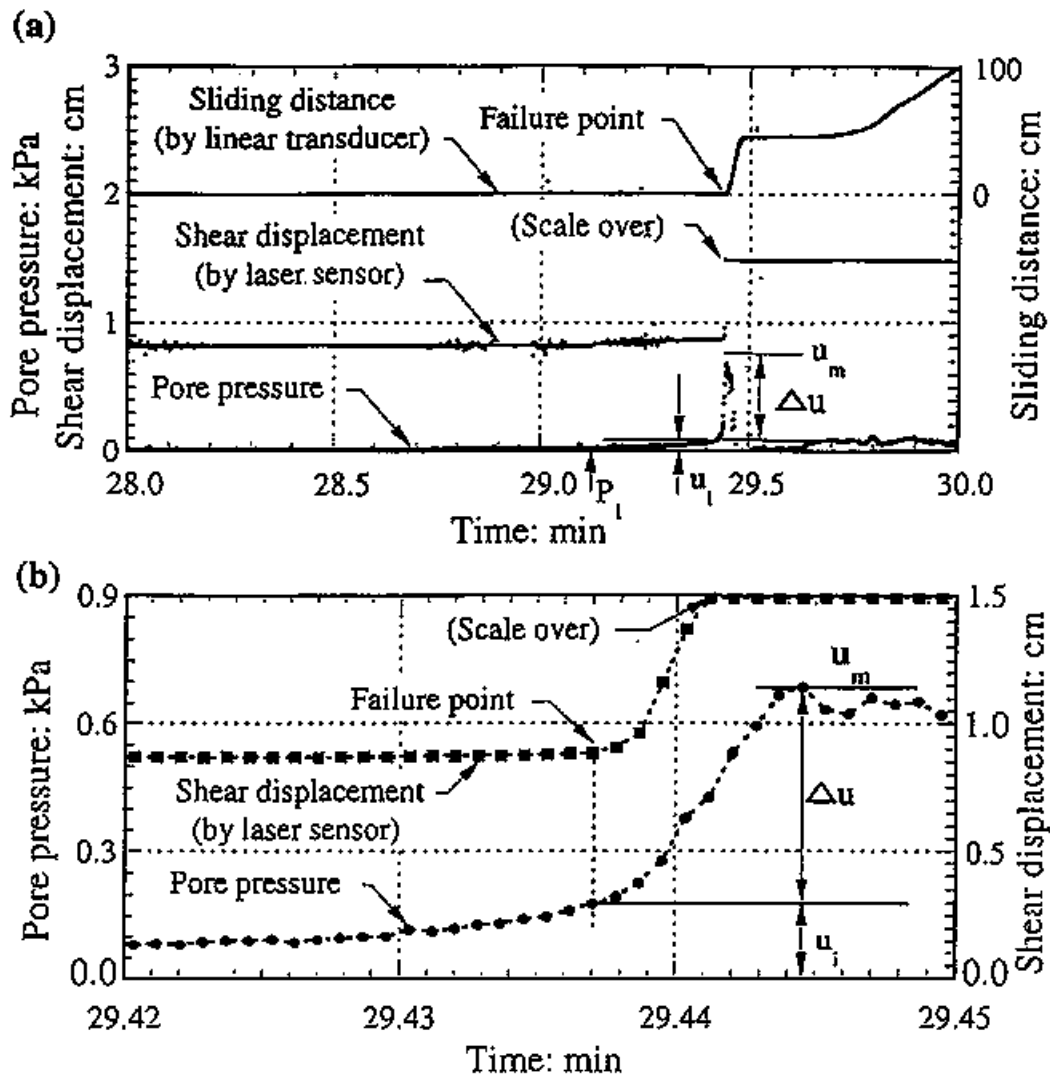


Figure 5.1 Time series of pore pressure and sliding distance for test S8_{g.8}.

(Sample: silica sand no. 8; Capacities of linear-displacement transducer and laser-displacement sensor are 100 cm and 15 mm, respectively; the displacements greater than the capacities were not determined.)

(a): Time series of pore pressure and sliding distance immediately before and after the failure.

(b): An enlargement of Figure 5.1a during the very short period of failure.

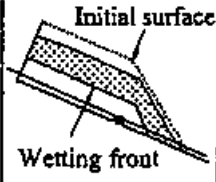
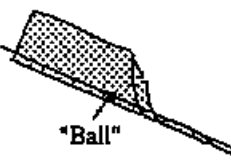

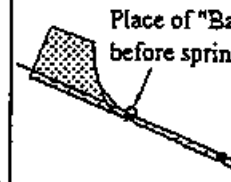

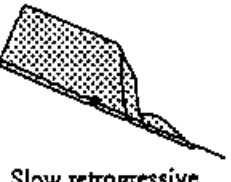
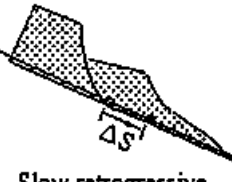

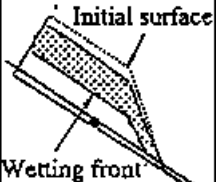
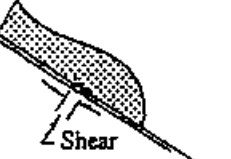


Type	Wetting	Precursory slides	Major failure	Successive motion
A S7 $l_d \leq 0.01$ Retrogressive sliding	 <p>Initial surface</p> <p>Wetting front</p> <p>Visible normal displacement</p>	 <p>"Ball"</p> <p>Slow retrogressive toe sliding</p>	 <p>Δs</p> <p>Sudden multiple sliding</p>	 <p>Place of "Ball" before sprinkling</p> <p>Very shallow flowslide</p>
B S7 $0.01 < l_d \leq 0.5$ Retrogressive sliding	 <p>Wetting front</p> <p>No visible normal displacement</p>	 <p>Slow retrogressive toe sliding</p>	 <p>Δs</p> <p>Slow retrogressive sliding</p>	 <p>Very shallow flowslide</p>
C S8, M10, M20, M30 $-0.14 \leq l_d \leq 0.46$ Flowslides	 <p>Initial surface</p> <p>Wetting front</p> <p>With/without visible normal displacement</p>	 <p>Shear displacement</p> <p>Shear deformation as a whole</p>	 <p>Δs</p> <p>Rapid flowslide failure</p>	 <p>l_m</p> <p>Slow sliding</p>

Figure 5.2 Summarized failure modes.

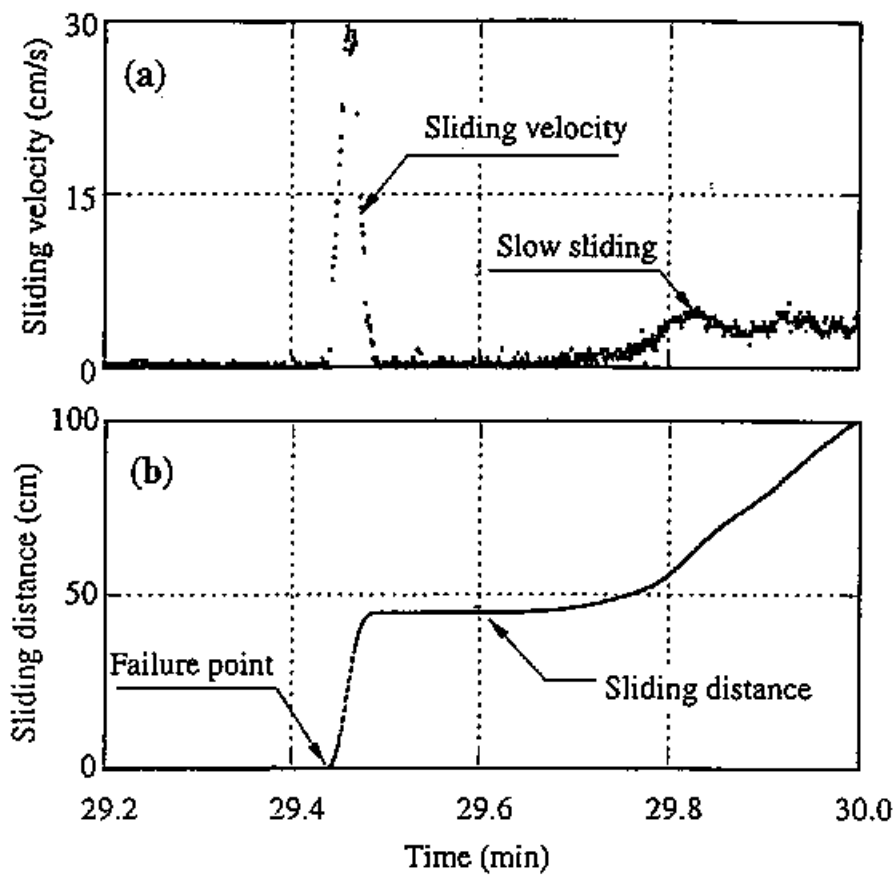


Figure 5.3 Variation of sliding distance and sliding velocity for test S8_{fl.s}.

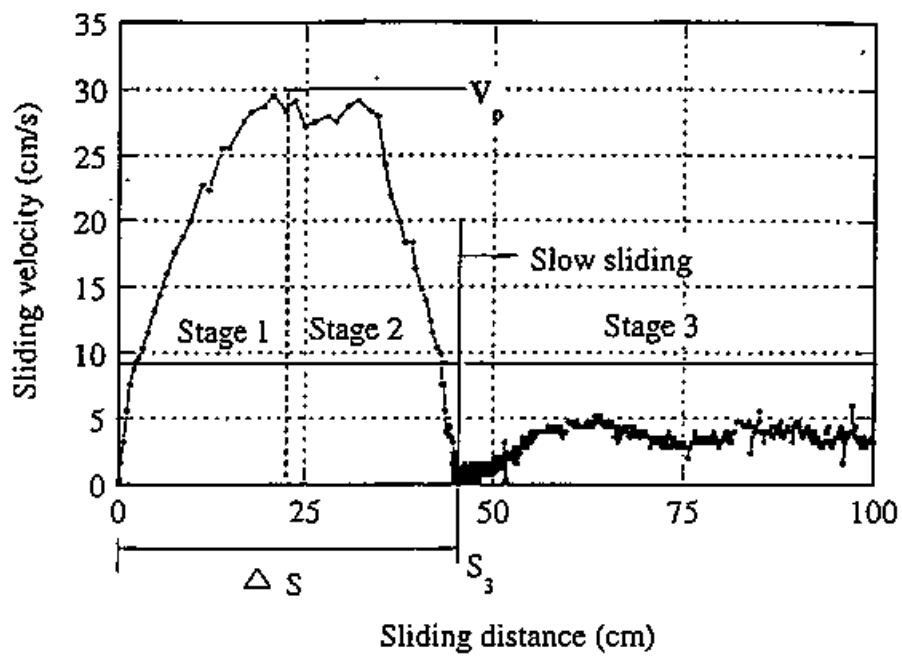


Figure 5.4 Variation of sliding velocity in relation to sliding distance ($SS_{U.S}$).

S_3 : Beginning of Stage 3; ΔS : Rapid run-out distance.

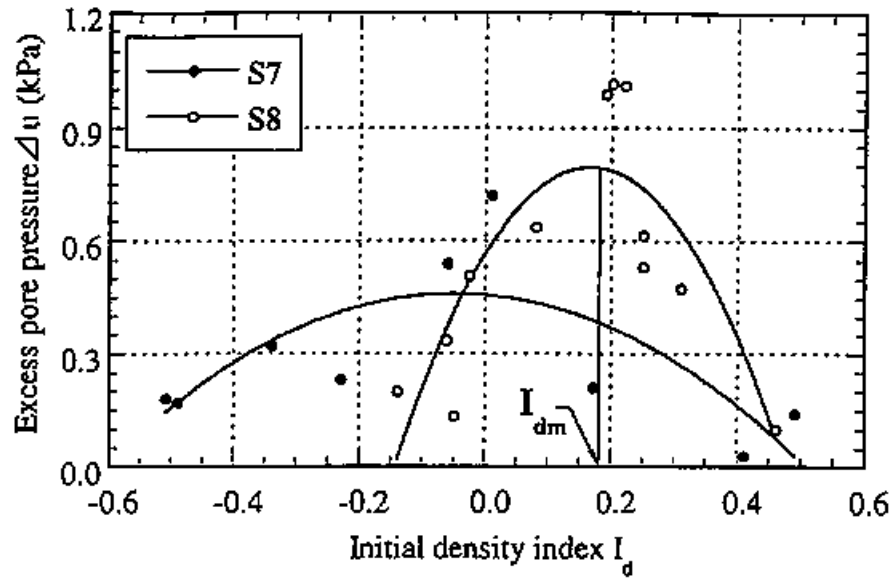


Figure 5.5 Relationship between excess pore pressure and initial density index.

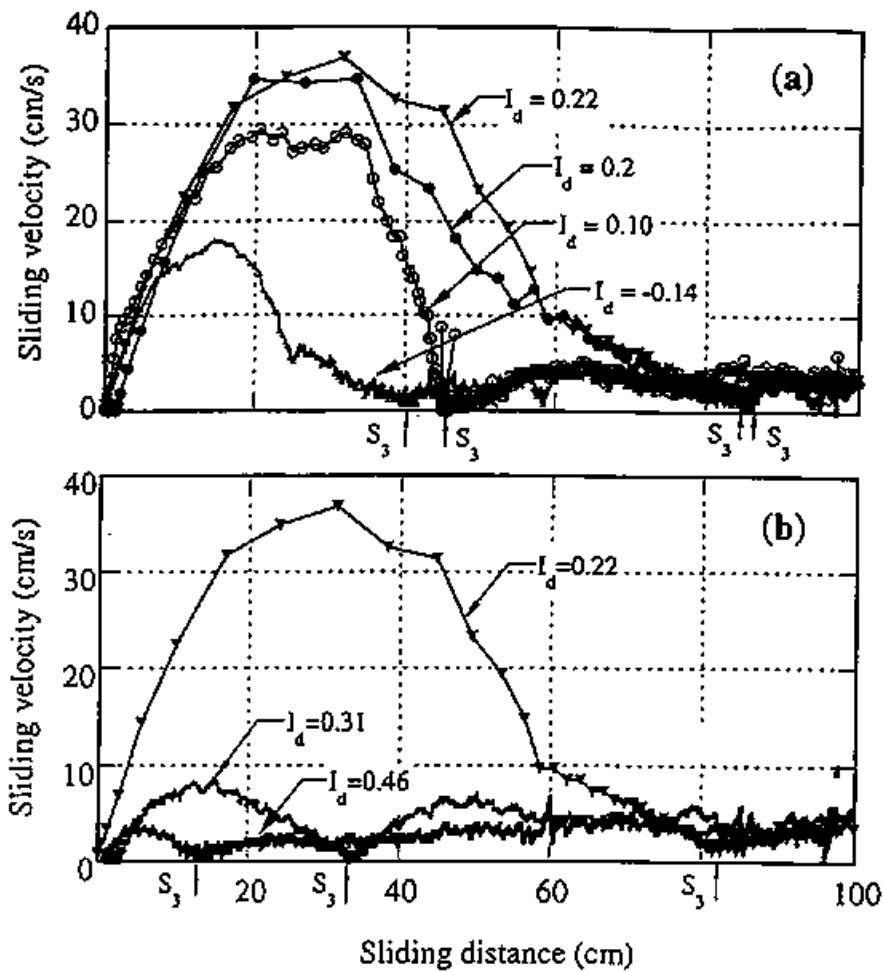


Figure 5.6 Variation of sliding velocity for samples with different initial density indexes.

- (a): for tests with initial density index $I_d \leq 0.22$ ($S8_{0.5}$, $S8_{0.6}$, $S8_{0.8}$, $S8_{0.12}$);
 (b): for tests with initial density index $I_d \geq 0.22$ ($S8_{0.1}$, $S8_{0.2}$, $S8_{0.5}$).

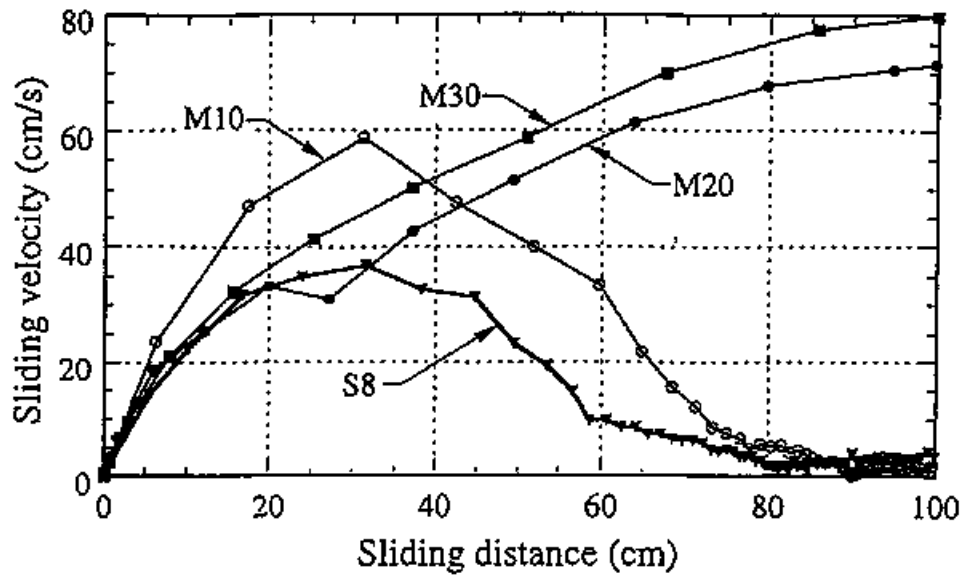


Figure 5.7 Variation of sliding velocity in relation to sliding distance for samples with different loess contents.

S8: Silica sand no. 8; M10: Mixture of silica sand no. 8 with 10 percent loess by weight; M20: Mixture of silica sand no. 8 with 20 percent loess by weight; M30: Mixture of silica sand no. 8 with 30 percent loess by weight.

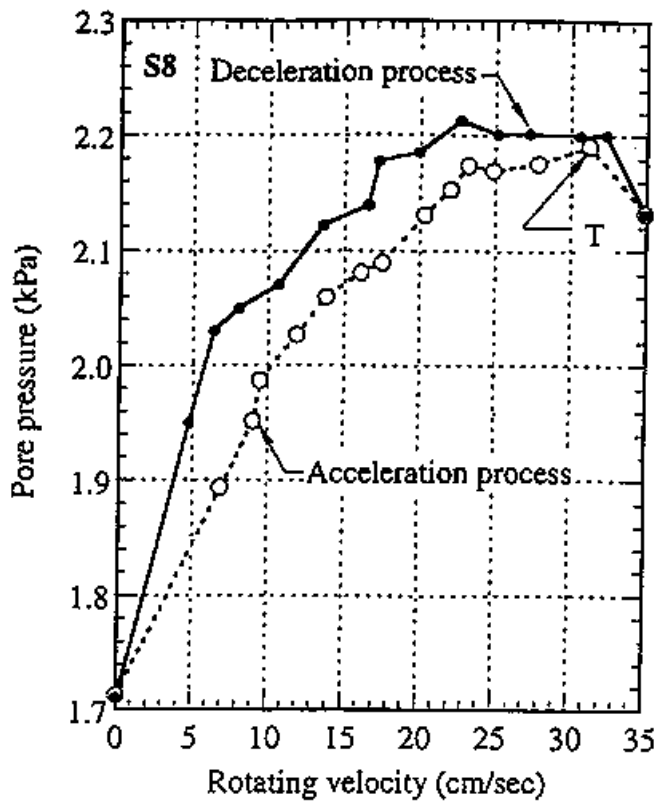


Figure 5.8 Variation of pore pressure in relation to rotating velocity for the test on saturated S8.

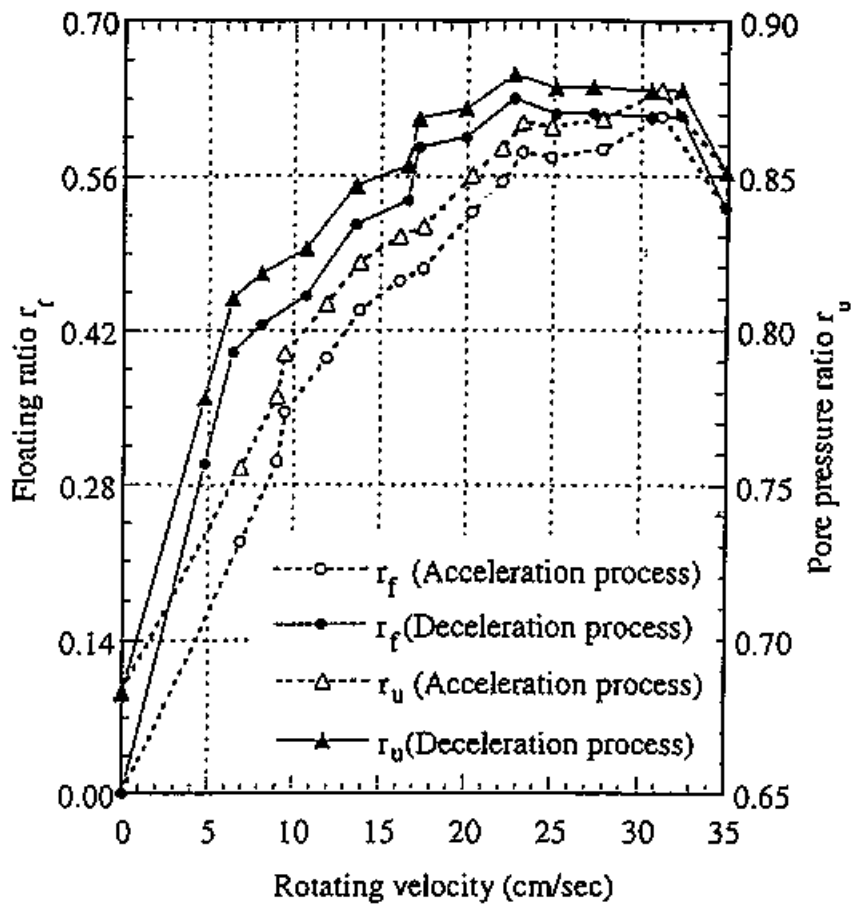


Figure 5.9 Pore pressure during motion for test on saturated S8 in the form of floating ratio and pore pressure ratio.

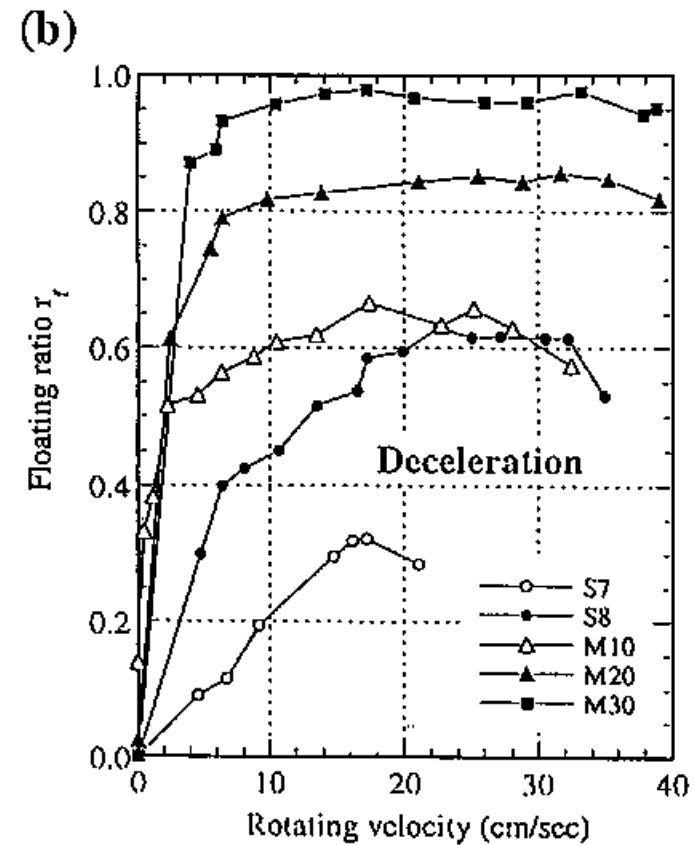
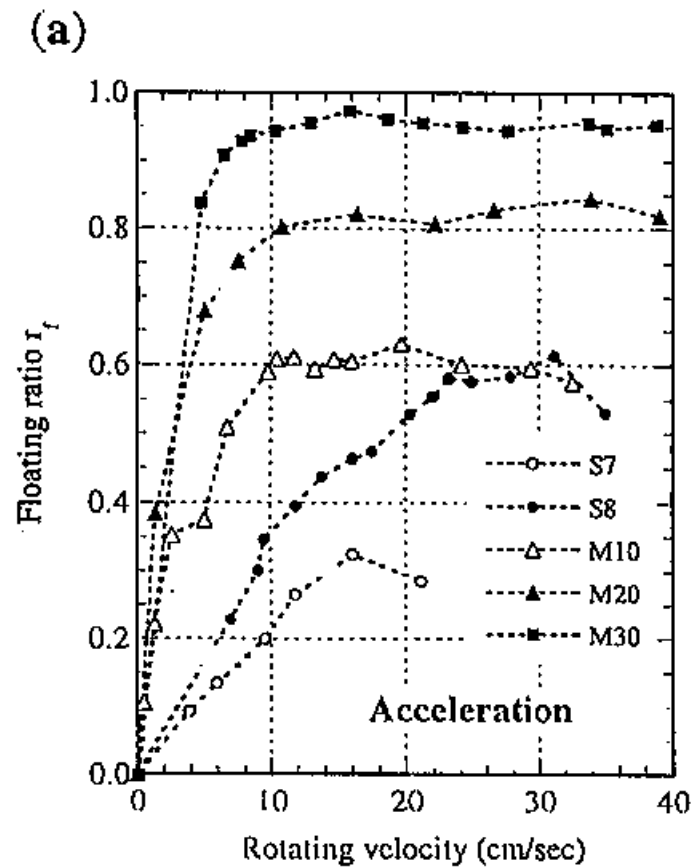


Figure 5.10 Results of double cylinder mixing tests on S7, S8, M10, M20, and M30.

(a): Variation of floating ratio against rotating velocity in the acceleration process;

(b): Variation of floating ratio against rotating velocity in the deceleration process;

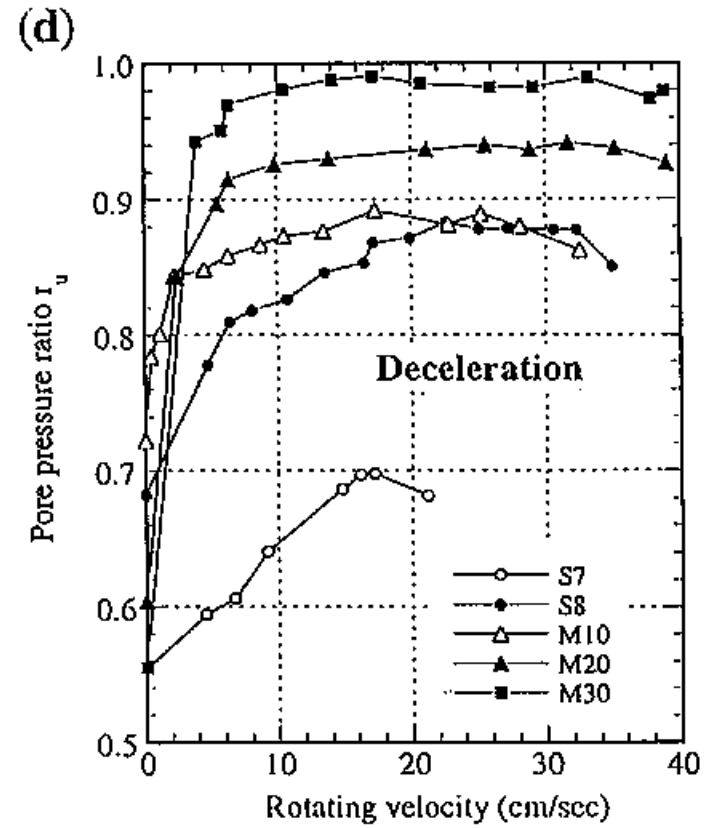
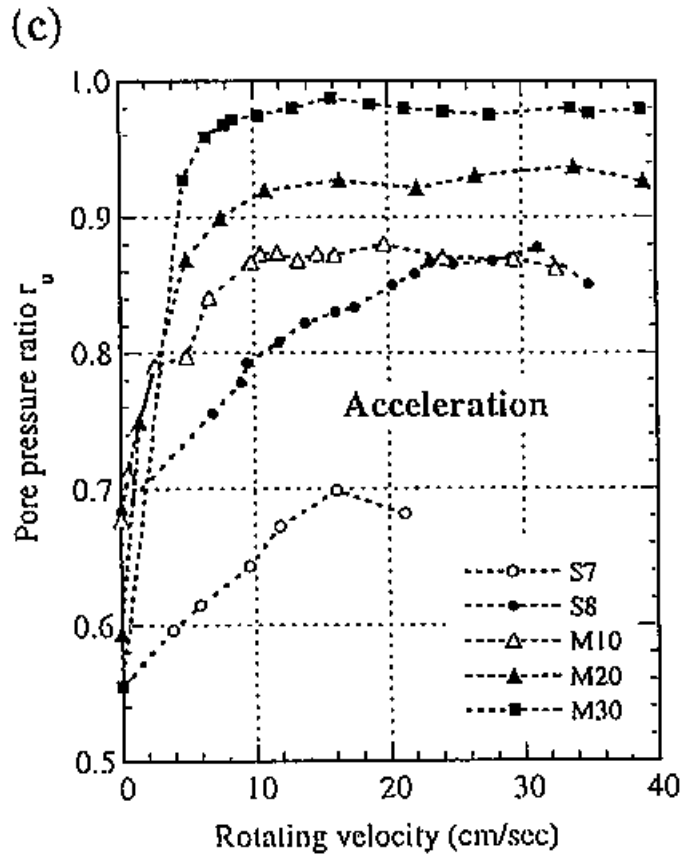


Figure 5.10 Results of double cylinder mixing tests on S7, S8, M10, M20, and M30.

(c): Variation of pore pressure ratio against rotating velocity in the acceleration process;

(d): Variation of pore pressure ratio against rotating velocity in the deceleration process.

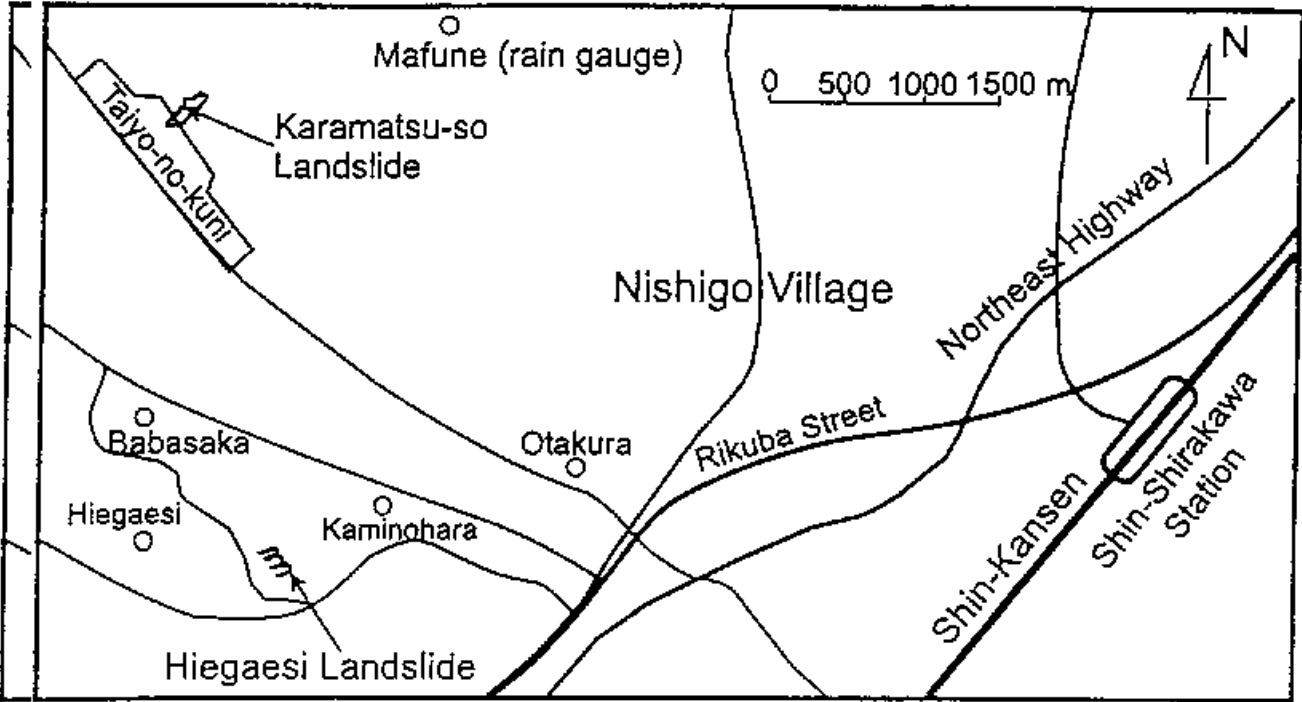


Figure 6.1 Location of the fluidized landslides.



Figure 6.2 The Hiegaesi landslide triggered by the August 1998 heavy rainfall depositing in a paddy field in Hiegaesi of Otakura, Nishigo Village (photograph courtesy of M. Chigira).

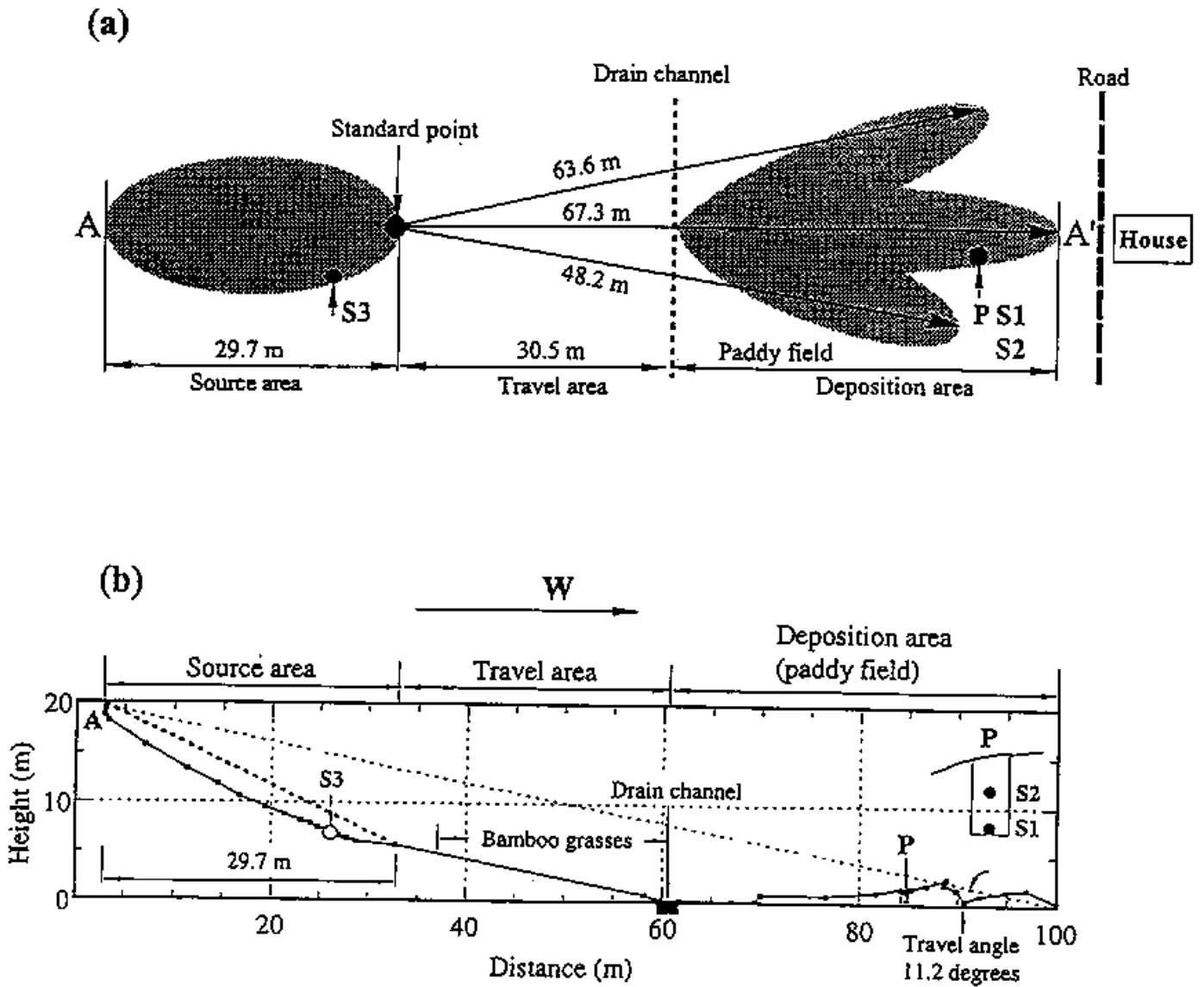


Figure 6.3 Plane sketch and longitudinal section of the landslide based on field survey

(S1, S2 and S3: sampling points; P: observation pit).

(a): Sketch of plane shape;

(b): Central longitudinal section.

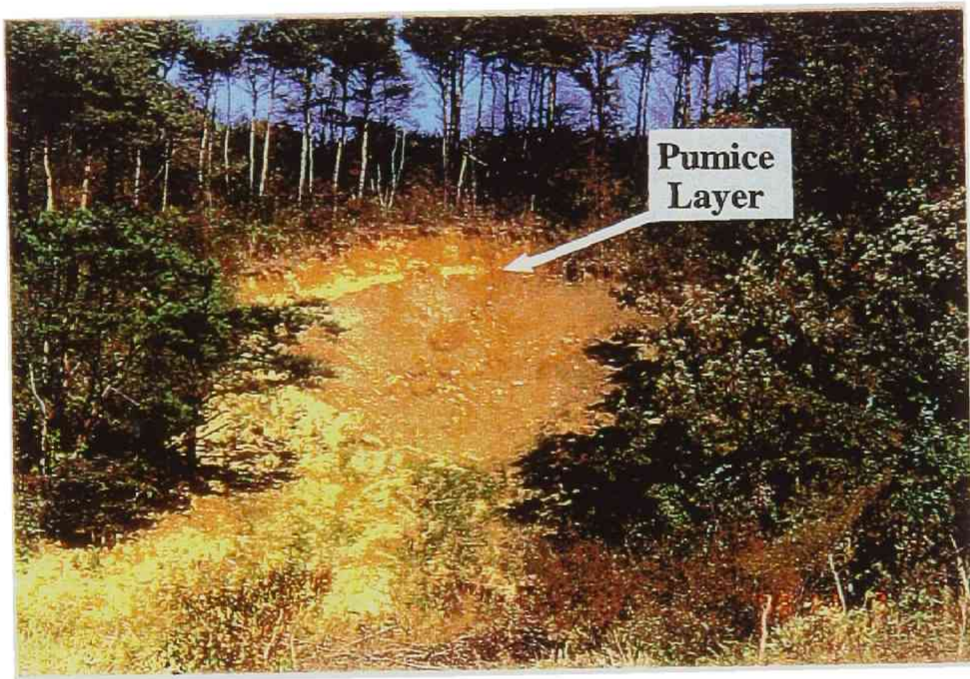


Figure 6.4 Source area of the Hiegaesi landslide (a yellow band over the dacite tuff is pumice layer).



Figure 6.5 Bamboo grasses in front of the source area brought down by landslide are keeping alive.

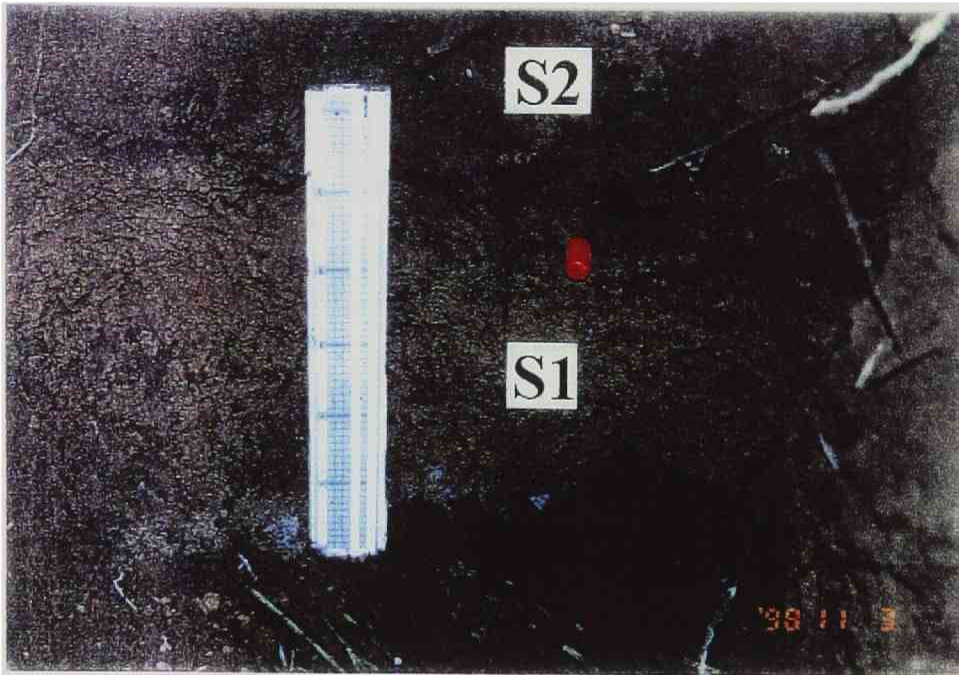


Figure 6.6 A close-up photograph in the observation pit (S1, S2: sampling points).

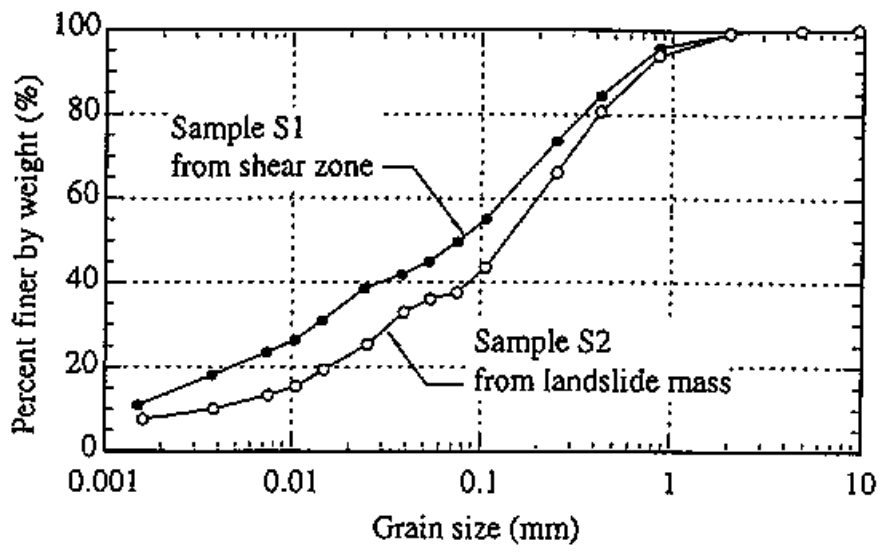


Figure 6.7 Grain-size distribution of sample S1 and S2.

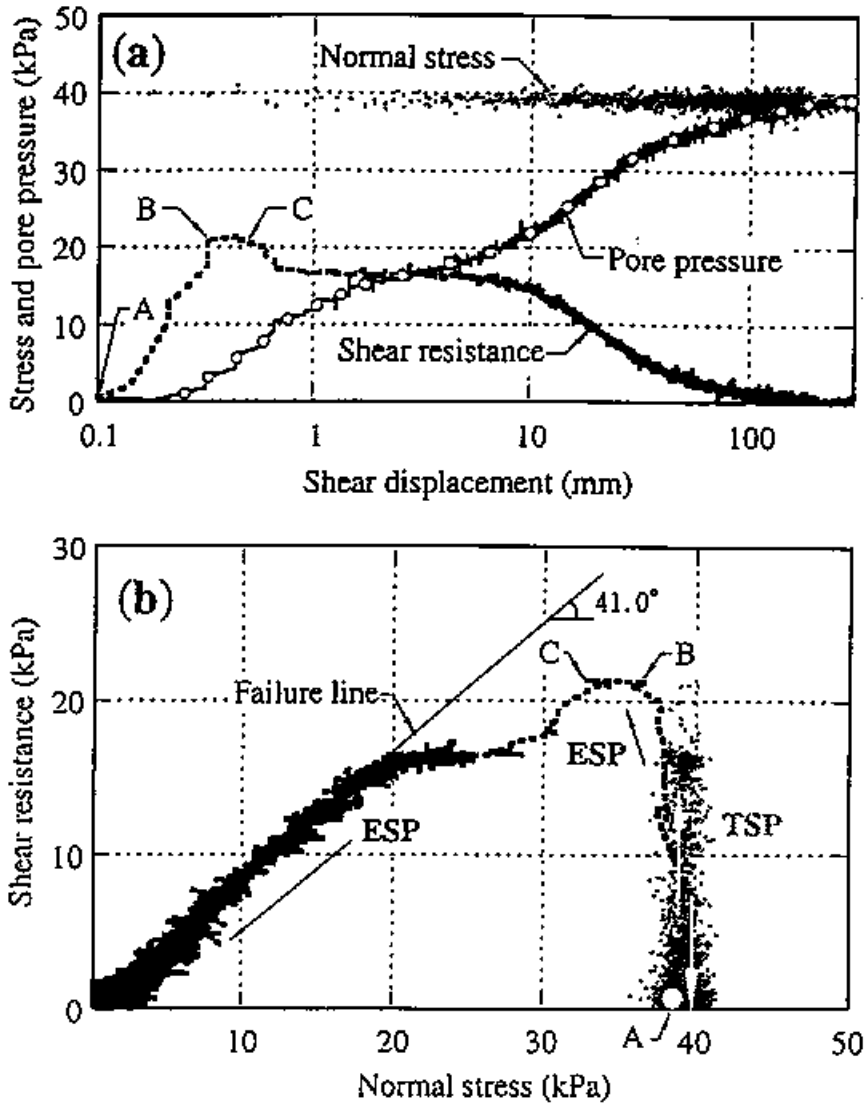


Figure 6.8 The undrained ring-shear test results on soils (sample S3) taken from the source area (Shear speed = 2 mm/sec, $B_D = 0.98$, $e = 1.93$).

- (a) Variation of normal stress, pore pressure and shear resistance with shear displacement;
- (b) Effective stress path (ESP) and Total stress path (TSP).

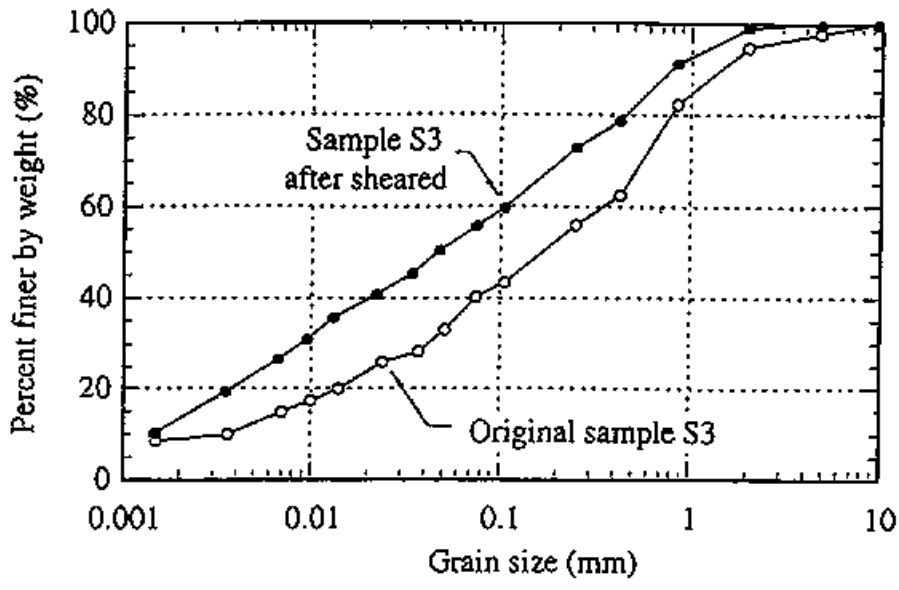


Figure 6.9 Grain-size distributions of sample S3 and that after sheared for 6.5 m in the drained condition.

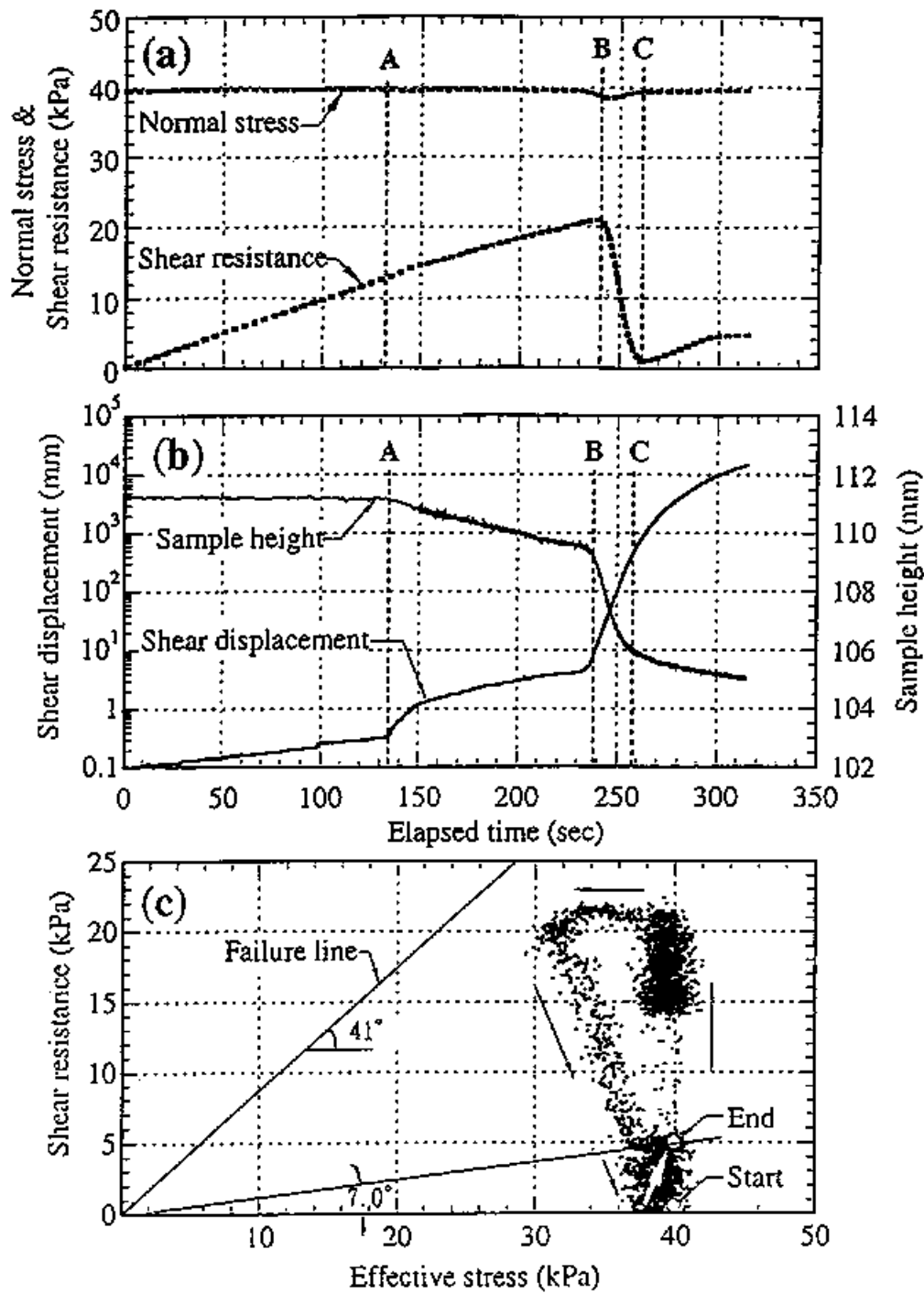


Figure 6.10 Results of drained ring-shear test on soil (sample S3) taken from the source area.

(Loading rate = 0.1 kPa/sec, $B_D = 0.98$, $e_0 = 1.82$)

(a) Variation of normal stress and shear resistance;

(b) Variation of shear displacement and sample height.

(c) Effective stress path.

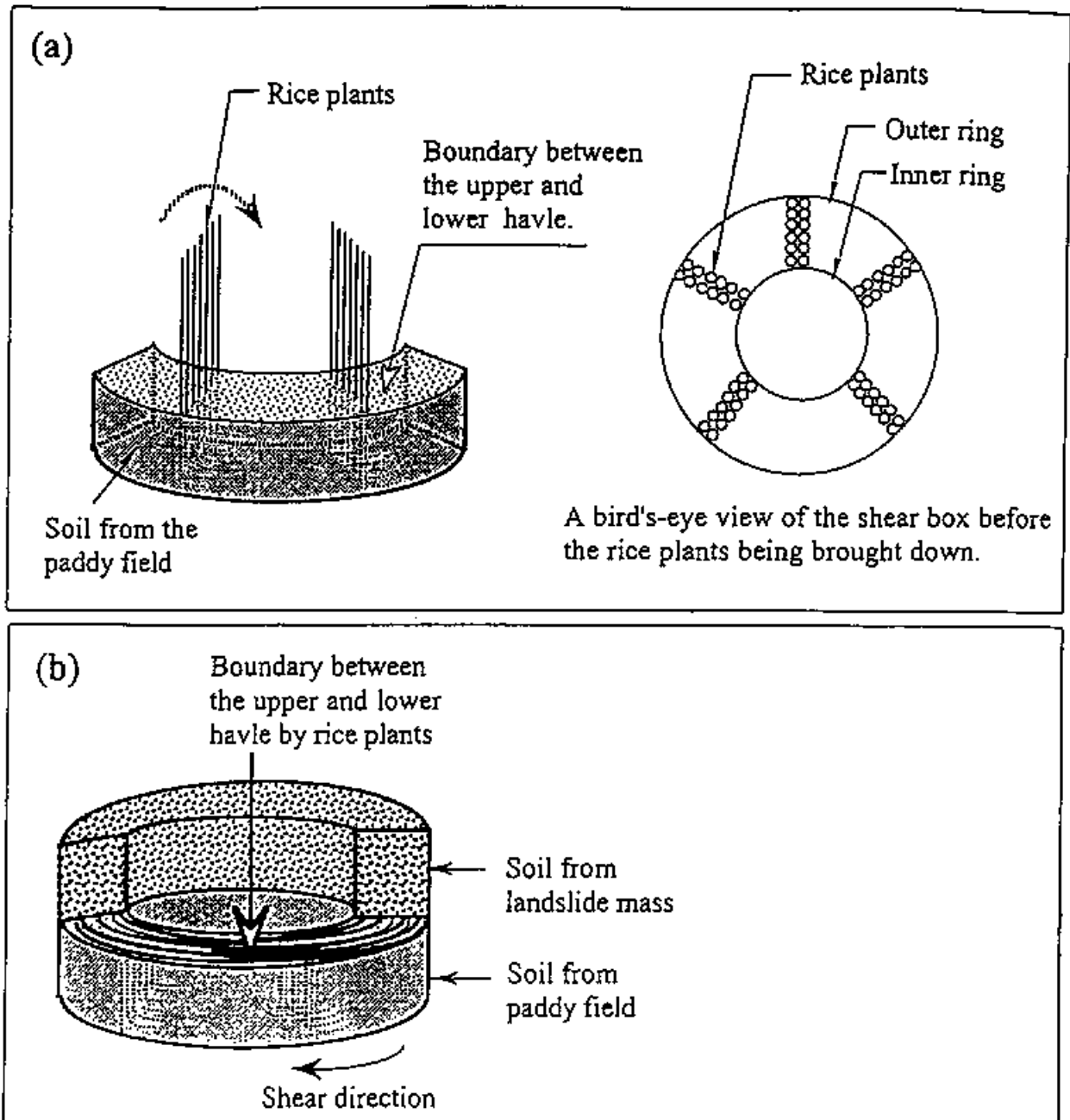


Figure 6.11 Schematic diagrams of sample preparation of rice plants and the soil from the landslide mass in ring-shear box.

(a): Schematic illustration of setting rice plants into the sample in ring-shear box;

(b): A schematic illustration of the motion of landslide mass on rice plants in ring-shear box.

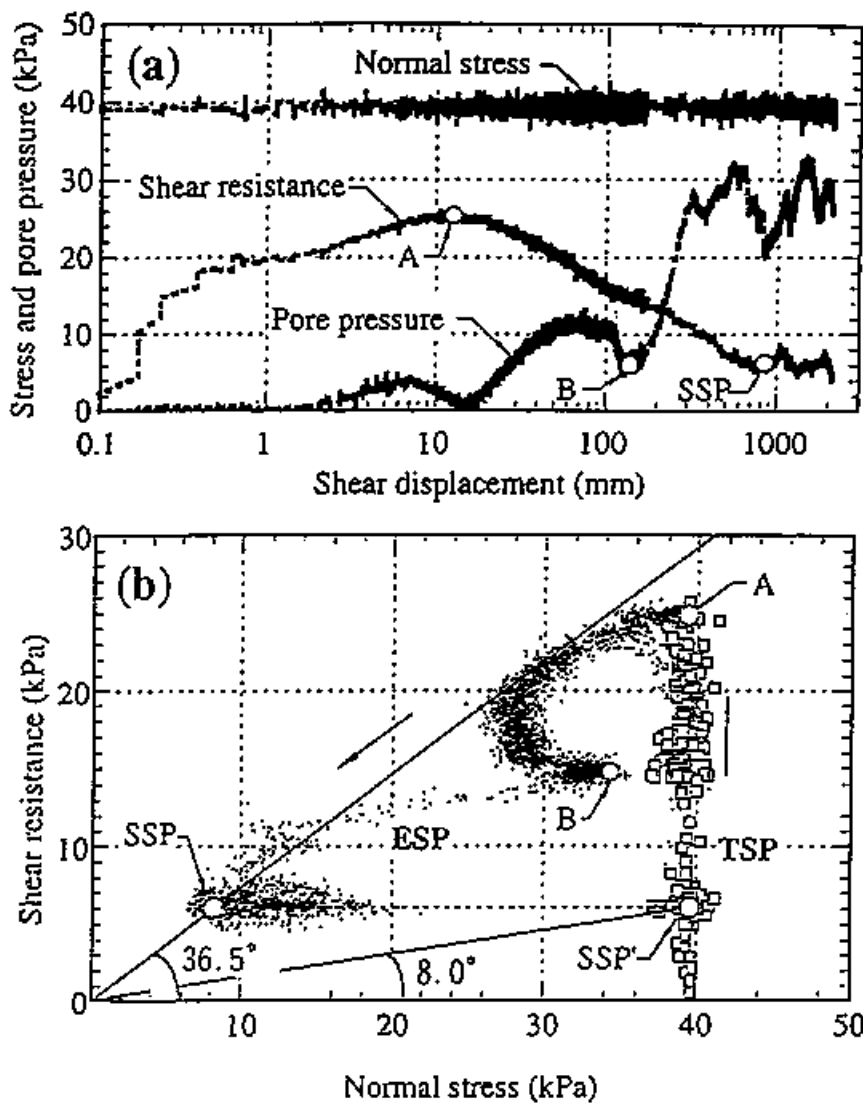


Figure 6.12 The ring-shear test results on rice plants and soil from landslide mass (shear speed = 2 mm/sec, $B_D = 0.55$).

- (a) Variation of normal stress, pore pressure and shear resistance with shear displacement;
- (b) Effective stress path (ESP) and Total stress path (TSP).

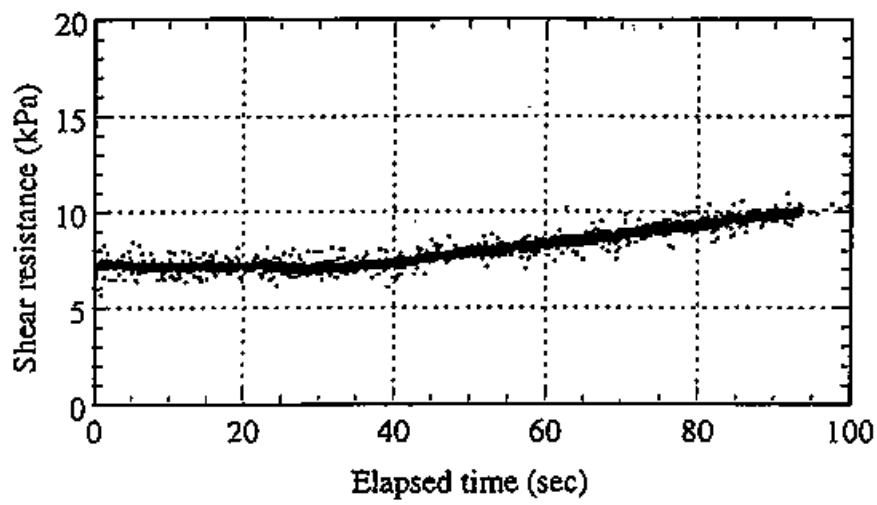


Figure 6.13 Recovering of shear resistance when shear box was turned into drained condition for the test on rice plants and soil.

(a)



(b)



Figure 6.14 Lower part of the shear box after the drained ring-shear test.

(a): Shear zone between rice plants and sliding soil mass. Pins show the border;

(b): Scratch on the bottom of the sliding soil mass caused by the relative motion with rice plants in the drained condition.